Master's thesis

2019

Steinar Åsmund Fagervoll

NTNU
Norwegian University of
Science and Technology
Faculty of Natural Sciences
Department of Materials Science and Engineering

Steinar Åsmund Fagervoll

Synthesis and Characterisation of NMC622 Cathodes for Lithium-Ion Batteries

- Using Chloride Solutions from Glencore Nikkelverk AS

July 2019

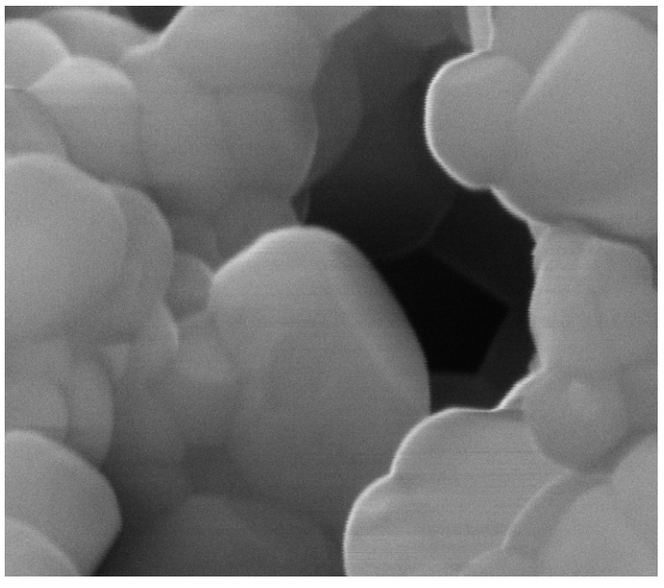

NTNU
Norwegian University of
Science and Technology

NTNU
Norwegian University of
Science and Technology

NTNU

Norwegian University of
Science and Technology

Synthesis and Characterisation of NMC622 Cathodes for Lithium-Ion Batteries

- Using Chloride Solutions from Glencore Nikkelverk AS

Steinar Åsmund Fagervoll

Nanotechnology for Materials, Energy and Environment
Submission date: July 2019
Supervisor: Sverre Magnus Selbach
Co-supervisor: Elise Ramleth Østli

Norwegian University of Science and Technology
Department of Materials Science and Engineering

Acknowledgement

This semester has been dedicated to working on and writing my master's thesis. As much as I'd like to take all the credit for myself, there are several people deserving of recognition, acknowledgment, and a heartfelt thank you for the roles they have played throughout this challenging semester.

First and foremost, I would like to extend my sincere gratitude to my supervisors, Fride Vullum-Bruer and Sverre M. Selbach, who have shared their knowledge and expertise on their respective academic fields with me, as well as reviewing my thesis and giving constructive feedback. I would also like to thank my co-supervisor, Elise R. Østli, who showed me the ropes in the laboratories, and who was always available whenever help was needed with experimental or theoretical problems.

I must also express my gratitude to Nils P. Wagner, who always had all the answers to why things went wrong, and how to fix them. To Silje N. Bryntesen, I would like to show my appreciation for all the laughs in the laboratory, and for the close cooperation during the work on our respective theses. I would also like to extend my thanks to the remaining members of the battery research group at NTNU.

Although academic support has been crucial to the success of the work in my thesis, there are people whose emotional support has been equally important to me. To my friends, who have helped take my mind off things when breaks were needed, and helped me focus when breaks were excessive, I will be forever grateful. I also humbly thank my family, who diligently does anything in their ability to provide for my well-being. Last, but not least, I must express my endless appreciation and love for my fiancée, Greta, who is always there for me whenever I need help with anything, or just need someone to rant to. Your devotion, patience and sincere support has inspired me throughout this semester, and will no doubt continue to in the future.

Summary

Efficient high-capacity batteries are becoming more and more important in our society, where the population is increasingly dependent on portable electronic devices and electric vehicles. In light of this, Glencore Nikkelverk AS has initiated a project where left-over chemicals are used for battery synthesis, which will also help reduce unwanted waste from the company. In this thesis, NMC622 powder for use as active cathode material in lithium-ion batteries was synthesised using a co-precipitation procedure. Nickel and cobalt precursors supplied by Glencore Nikkelverk AS was used to synthesise the powder (CPGC), and a reference batch was made using nickel and cobalt precursors from Sigma-Aldrich (CPSA). The structural, morphological and electrochemical properties of the powders and the resulting cathodes were investigated using a range of techniques, including SEM, XRD, BET, EIS and galvanostatic charge-discharge cycling. Both powders were phase pure with a low degree of cation mixing, and had somewhat spherical morphology. There was a large disparity in specific surface area due to larger particles for CPGC, possibly caused by the presence of chloride during synthesis. The electrochemical performance of CPGC was erratic, possibly due to side-reactions, which caused apparent capacity to drift beyond theoretical maximum. This can also be a result of potential presence of chloride, which could facilitate catalysis of unwanted side-reactions of the electrolyte. CPSA had better cycling results, with capacities around 200 mAh/g, and stable cycling over 100-200 cycles. CPSA was coated with aluminium phosphate (AL-CPSA), in order to reduce capacity degradation due to dissolution of manganese into the electrolyte. AL-CPSA showed slightly better capacity retention than CPSA, but had lower initial capacity, at around 140-155 mAh/g. Using chloride solutions from Glencore Nikkelverk AS has proved inconvenient, most likely due to the chloride content, and suggestions have been made so that the company may avoid similar problems in the future.

Sammendrag

Effektive batterier med høy kapasitet blir stadig viktigere i samfunnet, hvor folk blir mer og mer avhengig av bærbare elektroniske enheter og elektriske kjøretøy. På bakgrunn av dette har Glencore Nikkelverk AS startet et prosjekt hvor overflødige kjemikalier blir brukt til syntese av batterier, noe som også vil bidra til å redusere avfall fra bedriften. I denne masteroppgaven ble NMC622-pulver syntetisert ved hjelp av en ko-presipiteringsmetode, til bruk som aktivt katodemateriale i litium-ion batterier. Nikkel- og kobolt-forløpere fra Glencore Nikkelverk AS ble brukt til å syntetisere pulveret (CPGC), og et referansepulver ble også syntetisert med nikkel- og koboltforløpere fra Sigma-Aldrich (CPSA). De strukturelle, morfologiske og elektrokjemiske egenskapene til pulverene og de resulterende katodene ble undersøkt ved hjelp av karakteriseringsteknikker som SEM, XRD, BET, EIS og galvanostatisk sykling. Begge pulverene var faserene, med en lav grad av kationmiksing, og hadde til en viss grad sfærisk morfologi. Grunnet store CPGC partikler, var det stor forskjell i spesifikt overflateareal for pulverene. Dette kan ha vært et resultat av at kloridioner var tilstede i løsningen under syntesen. Den elektrokjemiske ytelsen til CPGC var svært ujevn, muligens grunnet sidereaksjoner som tidvis førte til at den tilsynelatende kapasiteten oversteg den teoretiske maksimale kapasiteten. Dette kan også skyldes tilstedeværelse av kloridioner som fasiliterer katalyse av uønskede sidereaksjoner i elektrolytten. CPSA viste bedre syklingsresultater, med kapasiteter rundt 200 mAh/g, og stabil sykling over 100-200 sykler. CPSA ble dekket med et aluminiumsfosfatbelegg (AL-CPSA) i et forsøk på å redusere degradering av kapasitet grunnet oppløsning av mangan i elektrolytten. AL-CPSA viste noe bedre kapasitetsretensjon enn CPSA, men hadde lavere initiell kapasitet, på rundt 140-155 mAh/g. Bruk av kloridløsninger som nikkel- og koboltforløpere fra Glencore Nikkelverk AS har vist seg å være upraktisk, sannsynligvis grunnet kloridinnholdet i disse, og forslag har blitt fremlagt slik at bedriften kan unngå lignende problemer i fremtiden.

Table of Contents

List of Tables

List of Figures

Abbreviations

Abbreviation	Explanation
AL-CPSA	Sample ID: Aluminium phosphate coated CPSA particles
BET	Brunauer-Emmet-Teller: Particle surface area analysis method
CPGC	Sample ID: Co-precipitation synthesis with Glencore chemicals
CPSA	Sample ID: Co-precipitation synthesis with Sigma-Aldrich chemicals
DEC	Diethyl Carbonate
DMC	Dimethyl Carbonate
DIW	Deionised Water
DRC	The Democratic Republic of Congo
EC	Ethylene Carbonate
EDS	Energy Dispersive X-ray Spectroscopy
EIS	Electrochemical Impedance Spectroscopy
EMC	Ethyl methyl Carbonate
FESEM	Field Emission Scanning Electron Microscopy
HOMO	Highest Occupied Molecular Orbital
LCO	$LiCoO_2$
LFP	$LiFePO_4$
LIB	Lithium-Ion Battery
LMNO	$LiMn_{1.5}Ni_{0.5}O_4$
LMO	$LiMn_2O_4$

Abbreviation	Explanation
LPF	$LiPF_6$
LUMO	Lowest Unoccupied Molecular Orbital
NCA	$LiNi_xCo_xAl_{1-x-y}O_2$
NEP	1-Ethyl-2-Pyrrolidone
NMC	$LiNi_xMn_yCo_{1-x-y}O_2$
NMC111	$LiNi_{0.33}Mn_{0.33}Co_{0.33}O_2$
NMC532	$LiNi_{0.5}Mn_{0.3}Co_{0.2}O_2$
NMC622	$LiNi_{0.6}Mn_{0.2}Co_{0.2}O_2$
NMC811	$LiNi_{0.8}Mn_{0.1}Co_{0.1}O_2$
PE	Polyethylene
PEIS	Potentio electrochemical impedance spectroscopy
PP	Polypropylene
PMGC	Sample ID: Pechini method synthesis with Glencore chemicals
PVDF	Polyvinylidene Difluoride
Redox	Reduction-oxidation
SEI	Solid-electrolyte interphase
SEM	Scanning Electron Microscopy
SHE	Standard Hydrogen Electrode
SSA	Specific Surface Area
XRD	X-Ray Diffraction
XRF	X-ray Fluorescence

Chapter 1

Introduction

1.1 Background

In a world faced with the prospect of major climatic changes, there is an imminent need for action to reduce carbon emission in production of goods and energy, as well as increasing the sustainability and efficiency of the energy infrastructure worldwide. One such action is the current large-scale energy transition, moving away from relying on fossil fuels to utilisation of renewable energy sources such as hydropower, solar cells or wind turbines. A major issue with these environmentally friendly energy sources is that the power production is intermittent, and often peak when energy consumption is relatively low. As such, there is a substantial and ever increasing demand for safe, reliable energy storage devices, with high energy efficiencies and capacities, with the ability to quickly store or supply energy when required.

Another consequence of increased environmental awareness is the rapid transition of fossil fuel vehicles to electrical vehicles. High quality batteries are essential in this field as well, with high capacities required for long range, and rapid charging processes to reduce downtime when traveling distances exceeding the maximum range of the electric vehicle [1, 2]. Safety is also a crucial aspect of the batteries used in vehicles, as life-threatening situations can arise if critical failure occurs at the wrong moment [3].

Quality of life improvement has always been an important motivator for research on many topics, and battery research is no exception. One example where this is prominent is in the field of portable electronic devices, of which the usage has skyrocketed in the last two decades. Cell-phones, laptops, smart watches and tablets are all used every day by a staggering amount of the worlds population. Batteries for such devices need to have high energy densities, as well as high capacities, rapid charging and high safety standards. Furthermore, the batteries must also be affordable in order to be viable for commercialisation in such products. Research on batteries that can fulfill these requirements has been conducted for several decades,

but still has potential for even better solutions. Eventually, the research led to the discovery of lithium-ion batteries (LIBs), which currently is the most commonly used battery in applications like electric vehicles and portable electronic devices [4].

The first commercially available LIB was developed by John B. Goodenough [5], and commercialised by Sony in 1991 [6, 7]. This battery had a graphite anode, and a layered transition metal oxide, initially $LiCoO_2$ (LCO), as a cathode. The layered nature of the cathode allowed reversible storage of lithium ions with capacities in the range of 140-150 mAh/g [7, 8, 9]. However, LCO cathodes were expensive due to the high price of cobalt, and also had safety issues related to low thermal stability. Exposure to elevated temperatures could cause exothermic release and thermal runaway reactions, in which the battery could spontaneously combust [10]. Due to these problems, research has been conducted to improve the performance, cost, stability and safety of these cathode materials.

One approach was to partially replace the cobalt in LCO cathodes with other transition metals or metals, such as nickel, manganese or aluminium [11]. Reduction of the cobalt content in cathodes was also motivated by the toxic nature of the element. This resulted in cathode materials with much higher capacities and energy densities than LCO, as well as higher thermal stabilities. One such cathode is $LiNi_xMn_yCo_{1-x-y}O_2$ (NMC), which is now commonly used in todays state-of-the-art batteries [9, 12, 13]. The NMC cathode has a theoretic capacity of 272 mAh/g, though the practical capacity is actually lower due to the aforementioned thermal runaway reactions that can occur when extracting excessive amounts of lithium ions from the cathode material [14]. Nevertheless, the batteries can still yield capacities in the range of 200-220 mAh/g, which is a considerable improvement from the early stages of LCO cathodes [8, 9, 13].

1.2 Aim of Work

This thesis is based on a collaboration between the Norwegian University of Science and Techonology and Glencore Nikkelverk AS, from here on referred to as Glencore. Glencore is a company that largely produces nickel, copper and cobalt metal, as well as sulphuric acid and smaller amounts of noble metals. The aim of the thesis is to study the potential for utilisation of nickel and cobalt precursors supplied by Glencore in production of state-of-the-art $LiNi_{0.6}Mn_{0.2}Co_{0.2}O_2$ (NMC622) cathode material for use in lithium ion batteries.

The thesis is a continuation of a project work performed by the author in august - december 2018, and will be heavily based on experience obtained in this time period. In the mentioned project work, hydrothermal synthesis was used in order to synthesise NMC622 cathodes. Two batches were made, one in which nickel and cobalt precursors from Glencore was used, and one “reference” batch in which only chemicals from standard chemical suppliers were used. The obtained batteries made with Glencore chemicals were non-functional due to a high degree of cation mixing and poor mechanical properties attributed to low binder content. Improvements were made to the synthesis procedure, resulting in functional batteries with

capacities in the range of 40-50 mAh/g for the reference batch cathodes. Due to the difference in synthesis parameters, no conclusion could be reached as to whether batteries could be synthesised with chemicals from Glencore.

To successfully achieve the main goal of this thesis, several aspects will be considered. Hydrothermal synthesis will be exchanged with two other synthesis methods in order to increase the amount of powder made with each batch; a Pechini method synthesis, and a co-precipitation synthesis. Furthermore, this project will apply improvements obtained in the aforementioned project work to the synthesis in order to make functional batteries with Glencore chemicals. This includes making a batch with "reference" cathodes, though refraining from having different synthesis parameters for the Glencore powder and the reference, so that a realistic comparison can be made between the two batches. An additional aim of this thesis is to attempt to reduce cyclic degradation of the capacity of the cathodes. To this end, the NMC622 particles will be coated with $AlPO_4$ in order to prevent dissolution of manganese in the electrolyte of the batteries, hopefully increasing the stability of the cathode material. The synthesised powders will be subjected to characterisation techniques to determine morphology, crystal structure and phase purity. In addition, the powders will be used to create coin cells, which will be characterised electrochemically in order to determine specific capacities, capacity retention, rate capability and internal resistance.

If chemicals from Glencore can be successfully used to create cathodes with high capacities and stability, it can open up a new source of revenue for the company, as well as potentially helping to reduce unnecessary waste by introducing a new resource pathway for chemicals which would otherwise be thrown away.

Chapter 2

Theory

2.1 Introduction to Batteries

2.1.1 Working Principle

The theory in this subsection is heavily based on Rahn and Wang [15], unless otherwise stated.

A battery is, by definiton, "A container consisting of one or more cells, in which chemical energy is converted into electricity and used as a source of power." [16]. The first batteries were *primary* batteries, i.e. non-rechargable. Traditionally, batteries consisted of two solid electrodes submerged in an electrolyte solution, with a separator in between. The materials used for the electrodes were chosen so that a spontaneous reduction-oxidation (redox) reaction would occur at the electrodes. A redox reaction involves two half-reactions, where one of the reactants is reduced in one of the half-reactions, while another reactant is oxidised in the other. In primary batteries, reduction and oxidation reactions occur at the positive and negative electrode, respectively. The electrolyte solution and the separator allows for conduction of positive and negative ions between the electrodes, while preventing conduction of electrons. Electrons are instead diverted through an external circuit which facilitates transport from the negative electrode to the positive electrode. When passing through this external circuit, the current resulting from the movement of electrons can be harnessed as electrical power.

Battery electrodes are often named according to the half reaction that occurs at them. The electrode at which an oxidation occurs is defined as the *cathode*, while the electrode at which a reduction occurs, is defined as the *anode*. Thus, in a primary battery, the positive electrode corresponds to the cathode, and the negative electrode corresponds to the anode. In *secondary*, i.e. rechargeable, batteries, however, this naming convention can be a source of confusion, because as a reverse voltage is applied across the two electrodes in order to recharge the battery, the redox reaction is reversed. This causes the half-reactions to be reversed as well,

pumping electrons and ions from the positive electrode to the negative electrode. In this case, the roles of the electrodes are reversed, so that the reduction occurs at the negative electrode, while oxidation occurs at the positive electrode. According to the definition of the electrodes, the negative electrode should now be referred to as the cathode, while the positive electrode should be referred to as the anode. In battery research, however, the convention is to always refer to the positive electrode as the cathode and the negative electrode as the anode, even though it is technically wrong during the recharge process. Thus, the names of the electrodes always correspond to the naming during the spontaneous discharge reaction, and thus also to the naming of electrodes in primary batteries. This naming convention will be used throughout this thesis.

A classic example of a secondary battery is the lead-acid battery, which has been extensively used in automobiles and other vehicles as a power source for starting, lighting and ignition of combustion engines. The cathodes and anodes in lead-acid batteries are PbO_2 and Pb, respectively, and the electrolyte is diluted sulphuric acid H_2SO_4. During discharge, Pb at the anode is reduced to $PbSO_4$ by $HSO_4{}^-$, and the excess H^+ ion travels through the electrolyte towards the cathode. The reduction releases two electrons, which are forced to travel through the external circuit, forming a current that can be harnessed as electrical energy. Meanwhile, PbO_2 at the cathode is oxidised to $PbSO_4$ by $HSO_4{}^-$ and H^+ ions, which consumes two electrons. During the charging process, these reactions are reversed. The half-reactions occurring at the cathode and anode are shown in Equations (2.1) and (2.2), respectively. The net reaction is shown in Equation (2.3).

$$PbO_2 + HSO_4^- + 3\,H^+ + 2\,e^- \underset{\text{charge}}{\overset{\text{discharge}}{\rightleftharpoons}} PbSO_4 + 2\,H_2O \tag{2.1}$$

$$Pb + HSO_4^- \underset{\text{charge}}{\overset{\text{discharge}}{\rightleftharpoons}} PbSO_4 + H^+ + 2\,e^- \tag{2.2}$$

$$Pb + PbO_2 + 2\,H_2SO_4 \underset{\text{charge}}{\overset{\text{discharge}}{\rightleftharpoons}} 2\,PbSO_4 + 2\,H_2O \tag{2.3}$$

2.1.2 Battery Research Terminology

In this subsection, important concepts in the battery research field will be defined and explained.

The open-circuit *cell potential*, V_{OC}, or the cell voltage, is one of these important concepts. The electrochemical reactions occurring in a battery is spontaneous when the cell potential is positive [17]. This can be seen from the Gibbs free energy, which can be described by the equation $\Delta G = -nFE_{cell}$, where ΔG is the Gibbs free energy, n is the number of moles of electrons transferred, F is the Faraday constant and E_{cell} is the cell potential. A spontaneous reaction occurs when the Gibbs free energy is negative, which is true when the cell potential is positive. The open-circuit cell potential is determined by the difference in potential between the two electrodes in the cell, as shown in Equation (2.4)

$$V_{OC} = (\mu_A - \mu_C)/e \tag{2.4}$$

where μ_A and μ_C is the electrochemical potential of the anode and cathode, respectively, and e is the elementary charge [18]. The potential at each electrode is in chemistry normally described relative to the standard hydrogen electrode (SHE), which is defined as having a potential of $E^0 = 0$ [17]. The electrochemical series is a series describing the reduction potential of half-reactions relative to the SHE. Notably, the half-reaction of Li/Li^+ has a reduction potential of -3.045 V, which is the lowest reduction potential of any metal, making it the strongest reducing agent. Due to this fact, most reasearchers working on lithium-ion batteries refer to electrode potentials relative to the Li/Li^+ reaction as opposed to potentials relative to the SHE.

The operating voltage of the cell is not always equal to the open-circuit voltage, however [18]. The chemical reactions will occur at a slightly different operating voltage due to the formation of an electrical double layer at the electrodes. This layer causes an internal resistance in the battery, increasing the energy required for transport of electrons from the bulk of the cathode's active material to the surrounding, conductive carbon black, as well as subsequent transport to the current collector. This increase in energy is called the *overpotential*, η, and is described as $\eta = I_{dis}R_b$ during discharge or $\eta = I_{ch}R_b$ during charge, where I_{dis} and I_{ch} are the currents during discharge or charge, respectively, and R_b is the internal battery resistance. The internal resistance is dependent on the current state of charge of the battery, q, which can be in the range $0 < q < 1$. This overpotential in turn decreases the operating voltage of the cell during discharge, V_{dis}, or increases the operating potential during charge, V_{ch}, as described by Equations (2.5a), (2.5b). Internal resistance in the battery also arises from intrinsic resistance of lithium transport in the electrode, and in the electrolyte [19].

$$V_{dis} = V_{OC} - \eta(I_{dis}, q) \tag{2.5a}$$

$$V_{ch} = V_{OC} + \eta(I_{ch}, q) \tag{2.5b}$$

The overpotential is thus proportional to the current, where an increase in current results in an increased overpotential. This effect is important when considering charging or discharging rates. High overpotentials lead to larger amounts of energy lost during charge or discharge, as excess energy is spent in order to charge the battery, and a reduced amount of energy is able to be extracted from the battery.

The amount of charge stored in a battery is known as the *capacity* Q of the battery [20]. The capacity is given in terms of a constant current I, and is described by Equation (2.6)

$$Q(I) = \int_0^{\Delta t} I dt \tag{2.6}$$

where Δt is the time that the battery can supply this current before it is completely discharged [18]. The capacity of a battery is often expressed in units of mAh. The capacity is dependent on the current, because the rate of transfer of ions across the interface between electrodes and the electrolyte becomes diffusion limited at high currents. The loss in capacity at higher currents is reversible, so the capacity should return to normal when lowering the current.

The rate at which the battery is charged or discharged is often referred to as the *C-rate*. This is a term that describes how quickly the entire capacity of the battery is charged or discharged [15], where 1C is defined as the rate at which the capacity is charged or discharged in exactly 1 hour. If a battery of 10 Ah is charged at 1C, a current of 10A is required for 1 hour. If the same battery is charged at 0.5C, it would be fully charged in 2 hours by applying a current of 5A. As discussed previously, though, increasing the C-rate at which a battery is charged or discharged causes a reduction in the capacity of the battery, due to a higher overpotential and diffusion limitations.

However, irreversible capacity loss can also occur in the battery [18]. This is often due to unwanted side reactions or damage to the electrodes which can occur during cycling. This irreversible capacity loss in each cycle is described by the coulombic efficiency, CE, which is a measure of the amount of charge inserted into the cathode during discharge, divided by the amount of charge extracted from the cathode during charge. This is described by Equation (2.7)

$$CE = \frac{Q_{dis}}{Q_{ch}} \times 100\% \tag{2.7}$$

where Q_{dis} and Q_{ch} are the capacities during discharge and charge in a single cycle, respectively. Coulombic efficiencies below 100% correspond to irreversible capacity loss, and if this is consistent in many cycles, the cumulative loss of capacity will cause capacity degradation over time. In many cases, a battery is considered to have reached its end of life when the capacity has decreased to 80% of the original capacity. This is due to the tendency of many batteries to have a sudden, rapid increase in capacity degradation, not long after 80-70% of the original capacity has been reached [21]. This phenomenon is often referred to as "sudden death" of a battery, and has been a major concern, especially for lead-acid batteries. Although not as prominent in LIBs, 80% capacity is still considered a rule of thumb for when to replace the battery, especially in electric vehicles or other applications where a sudden malfunction in the battery can be hazardous.

Capacity is an important parameter to consider when improving performance of batteries, but it is also important to be aware of energy requirements for batteries in specific applications. The energy contained in a battery is dependent on the current at which the battery is discharged, as was also discussed for the battery capacity. The energy E in a battery can then be found by measuring the time it takes to completely discharge the battery at a constant current I. This is shown in Equation (2.8).

$$E(I) = \int_0^{\Delta t} IV(t)dt \tag{2.8}$$

Considering the relationship between current and capacity from Equation (2.6), we can rewrite the equation for energy as seen in Equation (2.9)

$$E(V) = \int_0^{Q} V(q)dq \tag{2.9}$$

where Q is the total capacity of the battery, and V is the voltage of the cell. In plots of capacity vs. cell potential, the energy is thus visualised as the area underneath the curves. An example of such a plot for different cathode materials is shown in Figure 2.1. Energy is often expressed in terms of Wh or mWh.

In battery applications, weight or volume of the battery is often a limiting factor, such as in EVs, portable electronic devices or satellites. Therefore, the *specific capacity*, i.e. capacity relative to its weight or volume is considered an important factor. The *specific energy*, or energy density, is often represented as either gravimetric energy density, i.e. relative to weight, or volumetric density, i.e. relative to volume. Since the energy is a product of cell voltage and capacity, as shown in Equation (2.9), it is often desirable to have batteries with high specific capacities that operate at high operating potentials. For some applications, such as power tools, a high *power density* is more important than high energy density, because it is more important to extract the energy quickly from the battery, rather than having the battery last for a long time. Power is given by $P = VI$.

Electrodes used in LIBs are often characterised by inserting the electrode into a coin cell which has pure lithium metal as a counter electrode. This way, there is an "endless" supply of lithium available, and thus the performance of the electrodes can be studied independently. Such a cell is called a *half cell*, and is an important distinction from a normal cell, where supply of lithium is limited.

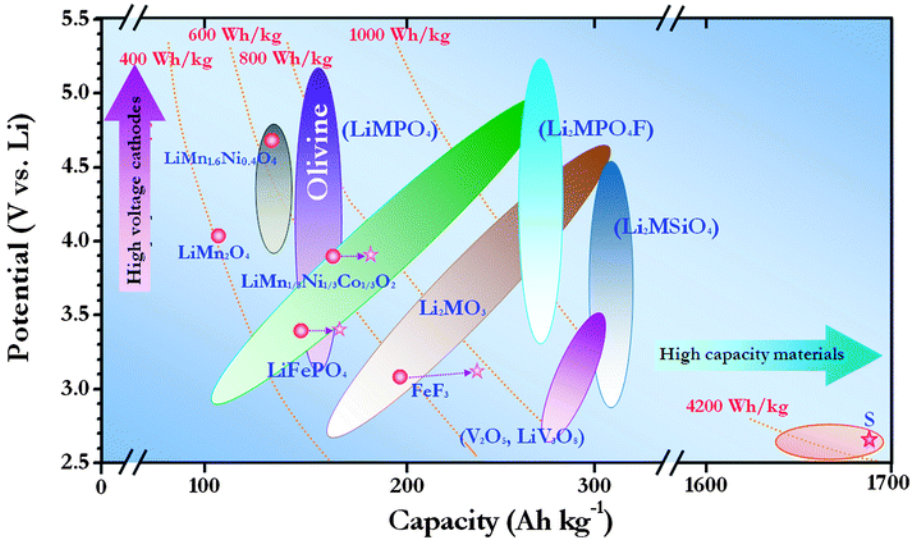

Figure 2.1: Cell voltage vs. Li/Li^+ vs. specific capacity for a range of cathode materials. The figure is retrieved from [22].

2.2 Lithium-ion Batteries

2.2.1 Background

Lithium ion batteries largely work in the same way as the lead-acid batteries described in the previous section. There are however some aspects with LIBs that set them apart from older technologies. This introduces additional possibilities, as well as challenges, which must be considered during development of new technologies for better and safer batteries.

Lithium-ion batteries generally use electrodes with a layered structure, allowing for the process of *intercalation* of lithium ions in the electrodes during charge transfer [15]. The intercalation process is a reversible insertion reaction, and allows lithium ions to be utilised without reducing them to their metallic form, instead subjecting the electrode materials to oxidation or reduction reactions. Multivalent ions are required in the electrode for successful intercalation to occur, in order to maintain charge neutrality [20]. Figure 2.2 shows a schematic of a typical LIB, with lithium cobalt oxide, LCO, as cathode, and graphite, C_6 as anode. During discharge, lithium ions are extracted from the anode, oxidising the carbon in the graphite, and move through the electrolyte towards the cathode. Electrons are thus ejected and travel through the external circuit. At the cathode, Li^+ intercalates into the cathode structure, reducing cobalt, and forming $LiCoO_2$. During charge, this process is reversed. Usually, unused batteries are initially in a discharged state, meaning lithium is already intercalated into the cathode. If excessive amounts of lithium are extracted from the cathode material, the structure of the cathode may collapse, irreversibly damaging the battery. LIB reactions are therefore often described in terms of removing only a portion of the available lithium, denominated x. The half reactions occurring at the cathode and anode are shown in Equations (2.10) and (2.11), respectively, and the net reaction is shown in Equation (2.12).

$$\mathrm{Li}_{1-x}\mathrm{MO}_2 + x\mathrm{Li}^+ + x\mathrm{e}^- \underset{\text{charge}}{\overset{\text{discharge}}{\rightleftharpoons}} \mathrm{LiMO}_2 \tag{2.10}$$

$$\mathrm{Li}_x\mathrm{C} \underset{\text{charge}}{\overset{\text{discharge}}{\rightleftharpoons}} \mathrm{C} + x\mathrm{Li}^+ + x\mathrm{e}^- \tag{2.11}$$

$$\mathrm{Li}_{1-x}\mathrm{MO}_2 + x\mathrm{C} \underset{\text{charge}}{\overset{\text{discharge}}{\rightleftharpoons}} \mathrm{LiMO}_2 + \mathrm{C} \tag{2.12}$$

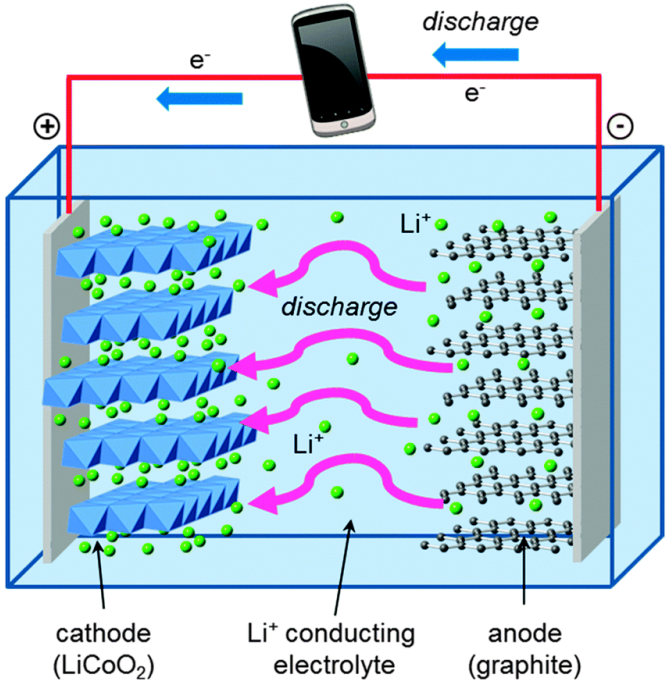

Figure 2.2: Schematic of Li-ion battery with $LiCoO_2$ as cathode and graphite as anode. When the battery is discharged, Li^+ flows from the anode to the cathode, while electrons travel through the external circuit where they can be harnessed in order to power a device. During charging, the process is reversed. The figure is retrieved from [2].

2.2.2 Anodes

Like the corresponding lead anodes in lead acid batteries, the anodes in lithium batteries could have been made out of pure lithium metal. Such an anode would have supplied such a large quantity of lithium that it would make any loss of lithium during cycling of the battery negligible. Lithium anodes have high specific capacities and low electrochemical potentials, as well as low densities, making them ideal anodes [23]. Using lithium therefore seems like a good choice for an anode. However, it has one severe problem which has limited the extent to which they have been used in batteries. When a lithium metal battery is charged, lithium ions deposit nonuniformly on the anode as lithium metal, resulting in formation of dendrites that extend into the electrolyte. This growth can extend so far into the electrolyte that the dendrites may penetrate the seperator, leading to short-circuiting and potentially spontaneous combustion of the battery. Due to these safety concerns, battery researchers have turned to other materials for use as anodes in LIBs, such as graphite or silicon [10].

In the last two decades, the most extensively used anode material in LIBs has

been graphite, which has a plethora of appealing properties [10]. The structure of a graphite anode is layered, allowing for intercalation of lithium ions at a ratio of 1:6 for Li:C. Graphite also has a low delithiation potential vs. Li/Li^+, which increases the cell potential of the battery compared to anodes of higher delithation potential. To achieve charge neutrality in the graphite anode, six carbon atoms change their oxidation states by -$\frac{1}{6}$ for each intercalated lithium ion. The electrical conductivity of the graphite anode is excellent, and the material is also affordable compared to many of its competitors due to the abundance of carbon. Furthermore, graphite has a high gravimetric capacity, although the volumetric capacity is quite poor. The specific capacity of graphite anodes are indeed high compared to any available cathode material, at around 372 mAh/g [24], which makes cathodes the limiting factor when it comes to the capacity of batteries. Nevertheless, other issues make graphite an important research topic, and resolving these issues will help improve their performance. One example is to better control the growth of the solid-electrolyte interphase (SEI) layer, an interphase which usually forms at the anode as a result of decomposition of electrolyte [25].

Silicon may well be the next generation anode, succeeding graphite anodes, but currently has severe problems with expansion and contraction during the lithiation/delithiation process, which irreversibly damages the anode [26]. Improvement of silicon anodes has therefore become an important focus area in anode material research.

2.2.3 Electrolytes

The electrolyte is a complex, but important part of battery systems due to its many different components, each with their distinctive roles. The electrolyte is usually made up of a mix of an inorganic lithium salt, as well as organic solvents [27, 28]. Commonly used organics include ethylene carbonate (EC), and dimethyl, diethyl, and ethyl methyl carbonate (DMC, DEC, EMC). Lithium hexafluorophosphate, $LiPF_6$ (LPF) is commonly used as the lithium salt. The requirements for a good electrolyte are many, and trade-offs are often necessary in order to obtain a functional electrolyte. It is important that the electrolyte is stable at the voltages that are used during battery operation. Furthermore, the electrolyte must be able to sustain ionic transport of the charge carriers, i.e. lithium ions in LIBs. It is preferrable that the components are safe and non-toxic, and can operate at a reasonable temperature range. The electrolyte should also passivate the anode, i.e. protect the anode from structural degradation and chemical side reactions. EC is a very important component in most electrolytes for use in LIBs due to its contribution to anode passivation. It is however often mixed with some of the other alkyl carbonates to improve e.g. viscosity of the solution to improve ion transport. LPF is not an ideal lithium salt, as it can decompose into LiF and PF_5, which can further hydrolyse to HF and PF_3O, both of which are able to facilitate unwanted reactions at the electrodes. However, LPF is considered the lesser evil compared to other lithium salts, which are either toxic, prone to combustion and explosion, or that can cause more severe side reactions than LPF.

The SEI is an interphase layer that can form on the anode through decompo-

sition of electrolytic salts and organic solvents [25]. A schematic of some of the possible constituents of an SEI layer is shown in Figure 2.3 [25]. Initial formation of this interphase layer is desirable as it protects against further decomposition of electrolyte components. The growth of SEI must however be controlled, to ensure that a stable SEI is formed. Certain additives are therefore included in the electrolyte to aid stabilisation of the SEI layer. The SEI must allow for transport of lithium ions between the electrolyte and anode, while also providing electric insulation. If SEI grows uncontrollably, ion conductivity may be drastically reduced, leading to poor performance of the battery. The SEI should also be somewhat flexible to allow slight volume expansion or contraction without crack formation during the lithiation/de-lithiation process of the anode. An excessively thick SEI layer may also block some parts of the anode entirely from being accesible to lithium ions, effectively reducing the anodes' ability to host lithium ions, and thereby also the capacity of the anode. A capacity drop is often seen after the first few cycles, due to the initial formation of an SEI layer.

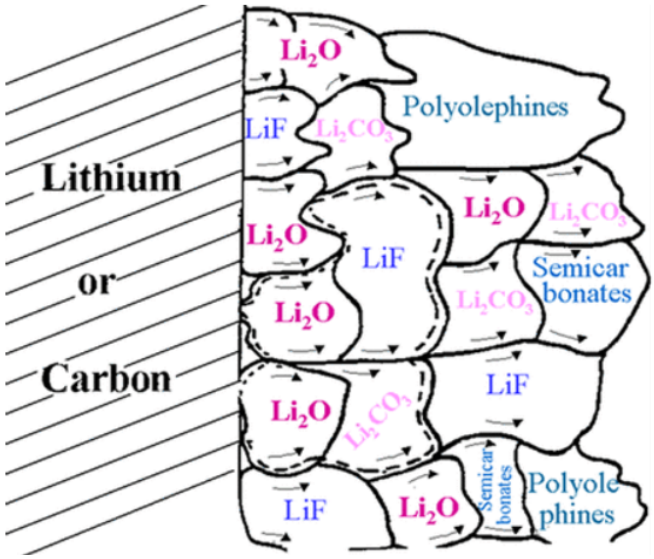

Figure 2.3: A schematic of how the SEI can be made up of several constituents resulting from decomposition of the electrolyte at the anode. The figure is retrieved from [25].

The decomposition of electrolyte to form an SEI is closely linked to the *electrolyte stability window*. The stability window of the electrolyte is defined as the energy separation E_g of the highest occupied molecular orbital (HOMO), and the lowest unoccupied molecular orbital (LUMO) [11, 29]. The HOMO and LUMO of an aqueous electrolyte is shown in Figure 2.4. Decomposition occurs at the cathode or anode if the electrochemical potential of the corresponding electrode is outside the electrolytic stability window, i.e. μ_C lower than the HOMO for the cathode or

μ_A higher than the LUMO for the anode. Thus, the cell potential of the battery should not exceed E_g of the electrolyte. However, graphite anodes do in fact have an electrochemical potential μ_A above the LUMO of a typical LPF electrolyte with alkyl carbonate solvents, thus making formation of a stable SEI passivation layer on the anode a necessity in order to protect the electrolyte and anode from further decomposition and side reactions.

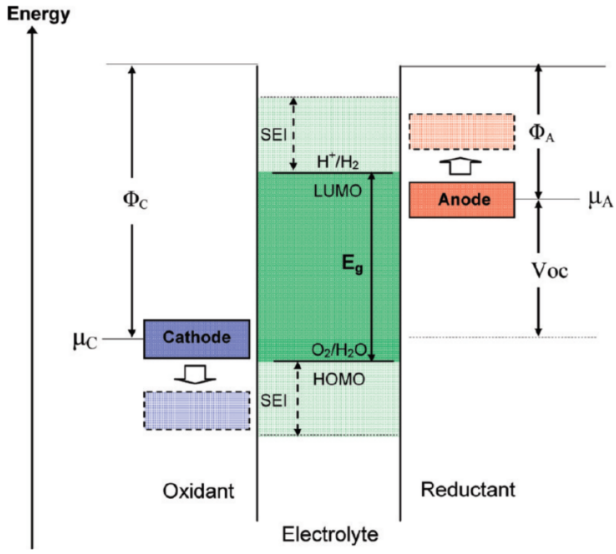

Figure 2.4: Schematic energy diagram of the energy gap E_g between the highest occupied molecular orbital and the lowest unoccupied molecular orbital of an aqueous electrolyte. The required chemical potentials for the cathode and anode to avoid formation of SEI layer formation is shown as μ_C and μ_A, and the open circuit voltage V_{OC} is the difference between these chemical potentials. The Figure is retrieved from [29].

2.2.4 Separators

The separator is vital for any battery cell to function properly [30]. It is crucial to both prevent direct contact between the two electrodes, and it must also prevent electronic conductivity, both of which would lead to short circuiting of the cell. The separator must also facilitate ionic conductivity to allow lithium ions to travel between the electrodes. Seperators are usually microporous polymeric membranes or fabrics. Furthermore, the separator must be chemically inert with regards to the electrodes and electrolyte, and have mechanical properties sufficient to withstand cell assembly. A typical separator in LIBs is one made out of a combination of polyethylene (PE) and polypropylene (PP).

2.2.5 Cathodes

As was discussed in the subsection regarding anodes, cathodes have become the limiting factor when it comes to specific capacity of a LIB. Naturally, many researchers are therefore attempting to discover novel cathode materials with potential for high capacity and capacity retention, as well as high specific energy and power. Cathodes used in LIBs are often seperated into different categories based on their mechanism of lithium transport [9, 10, 31, 32]. One type contain cathodes with spinel structures, such as $LiMn_2O_4$ (LMO) and $LiMn_{1.5}Ni_{0.5}O_4$ (LMNO), which allow three-dimensional transport of lithium ions in the cathode. Another type is the layered transition metal oxide cathodes, such as LCO, $LiNi_xCo_yAl1\text{-}x\text{-}yO_2$ (NCA) and the NMC cathodes. These cathodes facilitate two-dimensional transport of lithium ions. Finally, there are olivines, most notably $LiFePO_4$ (LFP), which allow for one-dimensional transport of lithium ions. The different cathodes each have different advantages and drawbacks compared to each other.

The spinels have low to medium capacities at 120 mAh/g and 150 mAh/g for LMO and LMNO, respectively, but have high operating potentials vs Li/Li^+ of 4.1 and 4.7 V [9, 33]. Both spinels have good capacity retention, the latter outperforming the former slightly, especially due to its higher operating potential which results in a higher specific energy [34]. LMO also suffers from rapid degradation and irreversible loss of capacity at higher temperatures [35].

LFP has a practical specific capacity around 170 mAh/g with an operating potential of around 3.45 V vs. Li/Li^+ [9]. Due to the abundance of iron, LFP is considered an affordable alternative to the other cathodes which contain more expensive elements like cobalt and, to a certain extent, nickel. In addition, the materials are also non-toxic which is an additional advantage to other cathode materials. It does however suffer from a low electrical conductivity as well as limitations to diffusion of ions.

The layered transition metal oxides have a much higher theoretical capacity than the other cathode materials. However, only part of this capacity is achievable due to structural degradation occuring in the case of delithiation of more than 50% of the lithium in the cathode material [9, 13]. LCO, which was the first commercially available cathode for LIBs, has a theoretic specific capacity of 272 mAh/g, but practically only around 160 mAh/g, at an operating potential of 4.2 V vs. Li/Li^+. NCA has higher theoretic capacity at around 200 mAh/g at an operating potential of 3.7 V vs. Li/Li^+ [10]. Capacities and operating potentials of NMC cathodes will be discussed in the upcoming section.

2.3 $LiNi_xMn_yCo_{1-x-y}O_2$ Cathodes

As described in the previous section, only 0.5 units of lithium ions can be extracted per unit formula of layered cobalt oxide [36]. This is due to chemical instability that arises from the overlap of the t_{2g} energy band of $Co^{3+/4+}$ and the O^{2-} $2p$ energy band. In order to solve this, cobalt is partially replaced by nickel and manganese, culminating in the cathode family known as NMC [10]. The overlap of the $Ni^{3+/4+}$

e_g energy band with the O^{2-} $2p$ energy band is much smaller compared to cobalt, which allows extraction of more lithium for use as charge carriers in the LIBs. This results in an increased practical capacity of the NMC cathodes compared to LCO, up to 220 mAh/g [13].

Due to the similarity in size between cobalt, nickel and manganese atoms, NMC retains the crystal structure of LCO, which is rhombohedral and belongs to the $R\bar{3}m$ space group. This crystal structure allows good transport of lithium ions in two dimensions, as discussed previously. The crystal structure is shown in Figure 2.5, where the alternating layers of lithium and transition metals can be easily identified.

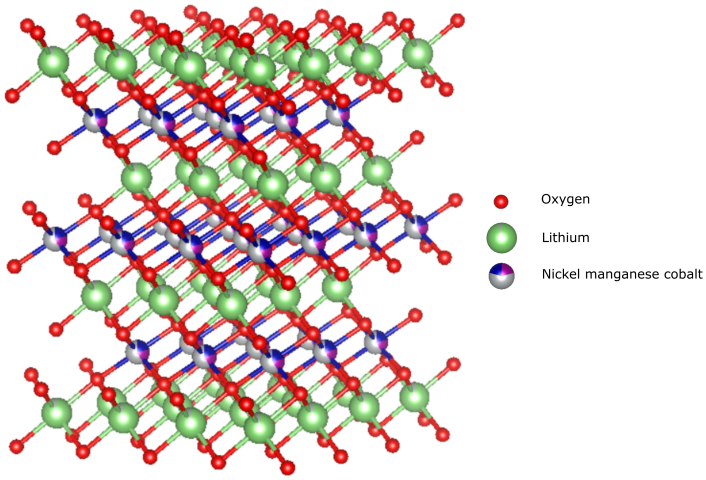

Figure 2.5: Crystal structure of $LiNi_{0.6}Mn_{0.2}Co_{0.2}O_2$, with space group $R\bar{3}m$. The figure has been adapted in VESTA [37] from the crystal structure of $LiNi_{0.33}Mn_{0.33}Co_{0.33}O_2$, found on Crystallography Open Database [38, 39, 40, 41, 42].

Introducing nickel and manganese into the LCO structure allows for different stoichiometries of transition metals in the cathode material [10]. The ratios between each transition metal have a large effect on the electrochemical properties of the cathode [43], which allows tailoring the properties of the cathode by using different stoichiometries. A visualisation of how each transition metal contributes to the cathode's properties is shown in Figure 2.6. Although both cobalt and nickel contribute to the electrochemical activity of the cathode, the content of nickel is more impactful, due to the band structures described in the first paragraph in this section [43]. Increasing the nickel content is thus a way to increase the specific capacity of the cathode. Cobalt and manganese both contribute to the structural stability of the cathode, which helps to prevent rapid capacity degradation as well as oxygen release and thermal runaway reactions that are a safety hazard for LIBs.

An increase in nickel content will entail a decrease in cobalt or manganese content, which will increase the capacity but simultaneously decrease cycling stability and safety of the cathode. Several NMC materials have therefore been studied in order to find materials with optimal performance. Examples of common NMC materials are $LiNi_{0.33}Mn_{0.33}Co_{0.33}O_2$ (NMC111), $LiNi_{0.5}Mn_{0.3}Co_{0.2}O_2$ (NMC532), NMC622 and $LiNi_{0.8}Mn_{0.1}Co_{0.1}O_2$ (NMC811).

Figure 2.6: A visual representation of how an increase in each transition metal affects different properties. Green colour indicates improved properties, while red colour indicates no effect or worsened properties. Orange colour indicates that cobalt contributes to capacity, but that it is not the main contributor.

Other factors also advocate the reduction of cobalt in production of cathodes for batteries. Cobalt is very expensive compared to other transition metals, which reduces the cost-efficiency of cobalt-rich cathodes [44]. Cobalt is also quite toxic, and is associated with several ethical issues. Over half of the world's supply of cobalt comes from The Democratic Republic of Congo (DRC), whose immoral mining industry has recently been shed light upon in a 2016 report from Amnesty International [45]. The report adresses abuse of human rights in DRC's cobalt mining industry, a problem that was also adressed by 2018 Nobel Peace Prize winner Denis Mukwege.

Specific capacities and capacity retentions in this paragraph have been retrieved from Noh et. al [46] for the purpose of comparison of the performance and properties of different NMC cathodes. The most extensively used NMC cathode on the market today is the NMC111 cathode, which utilises an even ratio of 1/3 of each of the transition metals [12]. Due to the relatively low nickel content, NMC111 has a specific capacity of around 160 mAh/g. The low capacity is remedied by its high capacity retention, at around 92% after 100 cycles at a C-rate of 0.5C. The other cathodes with higher nickel content, such as NMC532, NMC622 and NMC811 have higher capacities, at 175, 187 and 203 mAh/g, respectively. However, as expected, their capacity retentions are lower at around 90%, 85% and 70% after 100 cycles, respectively. The reduction in capacity retention with increasing nickel content stems from reduced thermal and structural stability of the materials [12]. Nickel-rich cathodes can experience release of oxygen at elevated temperatures, due to phase transformations from their layered structure via a spinel to a rock salt structure. Oxygen can then react with the electrolyte to form gases such as CO and CO_2, which causes capacity degradation during cycling. This release of oxygen occurs at a potential of around 4.7 V vs Li/Li^+ for NMC111 and NMC622, while

for NMC811 it can occur at potentials as low as 4.3 V. These potentials therefore limit the operating potentials of the cathode materials. Thus, NMC811 has a lower operating potential than the other NMC cathodes, and from Equation (2.9) they also have a lower specific energy than the other cathodes [12]. NMC622 has a moderately high operating potential, as well as a moderately high specific capacity, making it a well balanced cathode with potentially higher specific energies than other NMCs.

Although the NMC cathodes are usually shown as an ordered layered structure like the one shown in Figure 2.5, this is not always the case [13]. According to crystal-field theory, the unpaired electron spin in the e orbitals of Ni^{3+} causes instability of the ion, which can result in the ion forming as Ni^{2+} instead. Ni^{2+} has an ionic radius of 0.69 Å, while Li^{+} has an ionic radius of 0.76 Å. This similarity in size causes some nickel ions to occupy sites in the lithium layer, while the corresponding lithium ions occupy nickel sites in the transition metal layer. This effectively creates neutral antilattice defect pairs as shown with Kröger-Vink notation in Equation (2.13), a phenomenon known as cation mixing. Cation mixing can dramatically alter the performance of the cathode material, due to slower diffusion of lithium ions in the lithium layer. This occurs due to two seperate mechanisms. The disordered phase has a smaller interplanar distance in the crystal structure, raising the activation energy barrier for lithium diffusion through the lattice. In addition, the Ni^{2+} ions in the lithium layer act as physical barriers for lithium ions. This can be detrimental to the capacity of the cathode material, and especially affects the rate capability, due to the effects largely being related to reduced diffusion. Formation of Ni^{2+} instead of Ni^{3+} ions can occur both during synthesis, as well as during cycling of the battery. The occurence of cation mixing is related to deficiency of lihtium, which can occur due to evaporation of some lithium during heat treatment of the cathode material. Cation mixing significantly drops, however, when excess lithium is used during synthesis, making this an effective way to combat the problem [47]. Excess of lithium should nevertheless be limited to a certain extent, as an excess of over 10% has other implications which will reduce the specific capacity of the cathode [7]. For the purpose of this thesis, the *degree of cation mixing* will be used as a term to describe the percentage of lithium ions on nickel sites, and the adjoined percentage of nickel ions on lithium sites.

$$Ni_{Ni}^{\times} + Li_{Li}^{\times} \rightarrow Ni_{Li}^{\bullet} + Li_{Ni}^{`} \tag{2.13}$$

The changes in ordering of the crystal structure as a result of cation mixing is detectable in diffraction patterns obtained using X-Ray Diffraction (XRD) [13]. This technique is therefore very useful to detect whether cation mixing has occured in the cathode material. The disordering from cation mixing leads to partial destructive interference of the Bragg peak corresponding to the (003) crystal plane. Conversely, the Bragg peak corresponding to the (104) crystal plane experiences an increased intensity due to the Ni^{2+} ions in the lithium layer also lining up with the (104) plane. The relative ratio between the (003) and (104) crystal plane Bragg peaks can therefore be used as a qualitative assessment of the degree of cation mixing that occurs in the cathode material. In litterature, a ratio of larger than

1.2 is considered to be indicative of a satisfactorily low degree of cation mixing. Furthermore, the ratio between the intensities of the Bragg peaks corresponding to the (101) and (006)/(102) crystal planes are also indicative of the degree of cation mixing, as the intensity of the (102) Bragg peak diminishes when Ni^{2+} is present on lithium sites in the structure [48]. The degree of disordering of the structure can be assessed by either studying the peak splitting of the Bragg peaks corresponding to the (006) and (102) crystal planes, or the splitting of the peaks corresponding to the (108) and (110) crystal planes [49]. Rietveld refinement of the XRD data can be performed to obtain more accurate, quantitative data on the degree of cation mixing in the cathode material.

2.4 Powder Characterisation

2.4.1 X-ray Diffraction

XRD is a technique which relies on the detection of diffracted X-rays at different angles in order to determine crystal structure, phase purity and particle size of a sample [50]. Constructive interference of the reflected X-rays leads to high intensity of diffraction at certain angles, which are related to the interplanar distance between particular crystal planes, as described by Bragg's law. Differences in crystallographic structure lead to distinct X-ray diffractograms, and databases of such diffractograms can be used for comparison with the sample. Software can be utilised to further refine the results of XRD analysis. Rietveld refinement is a method that utilises the least-squares method to minimise differences between the observed and calculated X-ray patterns.

2.4.2 Scanning Electron Microscopy

A scanning electron microscope (SEM) is an instrument that utilises an electron beam to image a sample through detection of ejected secondary electrons or backscattered electrons [51]. The small wavelength of electrons allow imaging of features with dimensions smaller than the wavelength of light, contrary to traditional light microscopes. By scanning the electron beam across the sample surface, an image can be constructed from the detected electrons. Thus, the morphology and microstructure of a sample can be examined using an SEM.

2.4.3 Brunauer-Emmet-Teller Surface Area Analysis

The Brunauer-Emmet-Teller (BET) surface and porosity analysis technique is a method that utilises adsorption of gas, primarily nitrogen gas, onto a sample surface in order to estimate the surface area and porosity of porous samples [52]. The Langmuir isotherm can be employed to simplify the estimation of the surface area, but due to an assumption of ideal monolayer coverage of the sample surface by nitrogen atoms, this technique often underestimates the surface area. BET analysis incorporates multilayer coverage in its estimation, which makes the technique more accurate and precise. By assuming the sample particles to be spherical, a rough

estimate of the average particle diameter can be found by applying Equation (2.14), where $\bar{D}$ is the average particle size, ρ is the crystallographic density, and SSA is the BET specific surface area.

$$\bar{D} = \frac{6}{\rho \times SSA} \tag{2.14}$$

2.5 Electrochemical Characterisation

The theory in this section is based on Scholz, 2010 [53], except where otherwise stated.

2.5.1 Galvanostatic Charge-Discharge Cycling

One of the most common methods to test the performance of electrodes is to perform galvanostatic charge-discharge cycling of a half cell. Special battery testers are used for this, which apply a constant current to the coin cell, and detect the resulting voltage across the cell. Lower and upper limits are set for the voltage, so that when these voltages are reached, the current reverses. LIBs with NMC cathodes have lithium ions in the cathode when synthesised, so the first cycle is always a charge cycle. The currents used when testing the battery is determined by setting a theoretical maximum specific capacity, inputting mass of the active material, and choosing an appropriate C-rate. The actual capacity of the battery is then calculated by the software according to Equation (2.6). The Coulombic efficiency can also be calculated according to Equation (2.7).

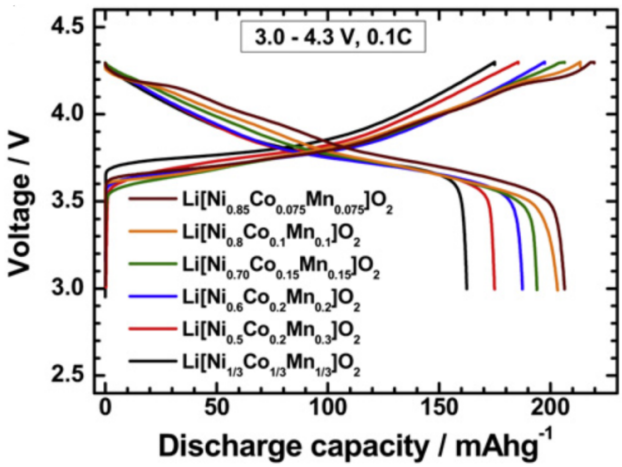

Figure 2.7: Cell voltage vs. Li/Li^+ vs. specific capacity for NMC cathodes. NMC622 is shown in blue. The current used corresponded to C-rate 0.1C. The figure is retrieved from [46].

The obtained information from galvanostatic charge-discharge cycling can be visually represented in many useful ways. Commonly, the voltage of the cell vs. Li/Li^+ is plotted as a function of the specific capacity, as shown in Figure 2.7. The Figure shows such plots for different NMC compositions, including NMC622

in blue. The plateaus indicate chemical reactions taking place, which is related to lithium ions inserted or extracted from the electrode [7]. The small incline towards the higher capacity of the charge curves (i.e. the curves starting at 3.0 V and ending at 4.3 V in the Figure) is typical for nickel rich cathodes. Plateaus that are entirely horisontal correspond to two-phase insertion reactions, while sloped regions indicate a single-phase solid-solution insertion reaction [54]. In vertical regions, where the voltage increases with no increase in capacity, no reactions occur.

The capacity retention of the electrode can be visualised by plotting the specific capacity of the electrode as a function of cycle number. An example of such a plot is shown for different compositions of NMC cathodes in Figure 2.8, with NMC622 shown in blue. A negative slope indicates capacity deterioration with each cycle. From the Figure, it is apparent that NMC compositions with higher nickel content has higher initial capacity, but also has a higher degree of capacity deterioration. It is also common to include plots of Coulombic efficiency in the same plot.

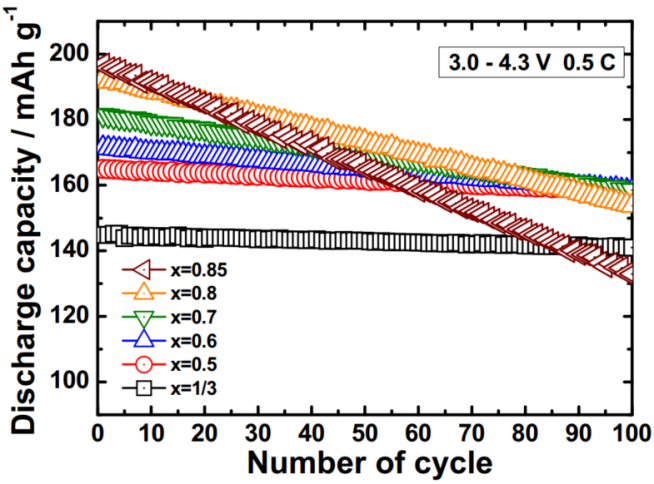

Figure 2.8: Specific capacity during discharge vs. cycle number for NMC cathodes of different compositions. The molar ratio of nickel to lithium is expressed as x. The current used corresponded to C-rate 0.5C. The figure is retrieved from [46].

By differentiating the capacity with respect to voltage, and plotting it against the cell voltage, a so called differential capacity plot is produced. Such a plot gives information about at what voltages the majority of the charge carriers are being inserted or extracted from the electrode, and an example for NMC622 is shown in Figure 2.9. The area underneath the curves correspond to the capacity of the battery, and as seen in the figure, the area will decrease as the battery is cycled and the capacity drops. The plateaus mentioned in Figure 2.7 are seen as peaks in a differential capacity plot. Separate peaks are related to different reactions, such as intercalation reactions or phase transitions, which are linked to the reduction or oxidation of transition metals in the electrode.

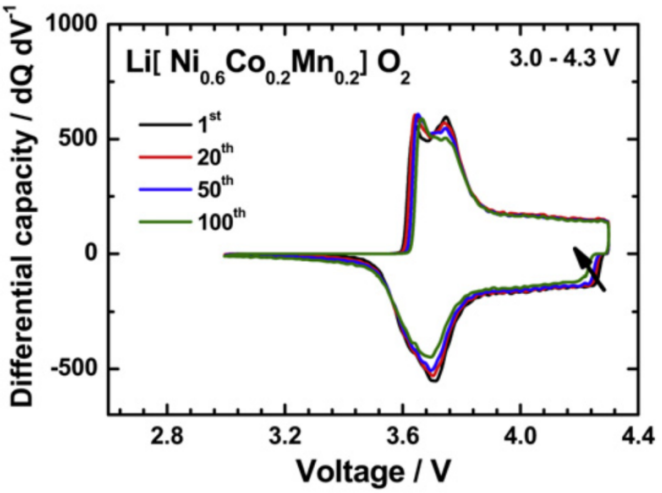

Figure 2.9: Differential capacity vs. cell voltage vs. Li/Li^+ for NMC622. The figure is retrieved from [46].

As discussed previously, the electrochemical performance of a cell is dependent of the C-rate at which the battery is charged or discharged. Galvanostatic charge-discharge cycling can therefore either be performed at a constant C-rate, as discussed in the previous paragraph, or can be cycled across different C-rates to see how the battery reacts to the different C-rates. Such a cycling procedure is referred to as a *rate-capability* test. This is commonly achieved by starting at a low C-rate of e.g. 0.1 or 0.2 C, and increasing the C-rate every 5 or 10 cycles. After reaching the highest desired C-rate, the current is usually returned to the initial C-rate, for comparison on whether the capacity at the lowest C-rate has been retained after cycling at higher C-rates.

2.5.2 Electrochemical Impedance Spectroscopy

The kinetics of an electrochemical system can be investigated by using electrochemical impedance spectroscopy (EIS). This technique applies small perturbations to the system, which results in a shift of the steady state. Characteristic parameters such as diffusion coefficient, reaction rate constants or charge transfer resistance of the system may then be determined according to the rate at which the system reaches a new steady-state.

Applying a monochromatic alternating voltage $U(t) = U_A sin(\omega t)$ to an electrode will result in a current of $I(t) = I_A sin(\omega t - \vartheta)$, where U_A and I_A are the amplitudes of the sinusoidal voltage and current, respectively, and ϑ is the phase difference between the voltage and the current. The impedance Z is then

$$Z = \frac{U(t)}{I(t)} = |Z|e^{i\vartheta} = Z_{Re} + iZ_{Im} \tag{2.15}$$

where i is the imaginary unit $\sqrt{-1}$, and Z_{Re} and Z_{Im} are the real and imaginary components of Z, respectively. A common way to represent EIS measurements is to plot the imaginary part of the impedance as a function of the real part of the impedance, while varying the frequency, resulting in what is referred to as a Nyquist plot. A Nyquist plot is shown in Figure 2.10,

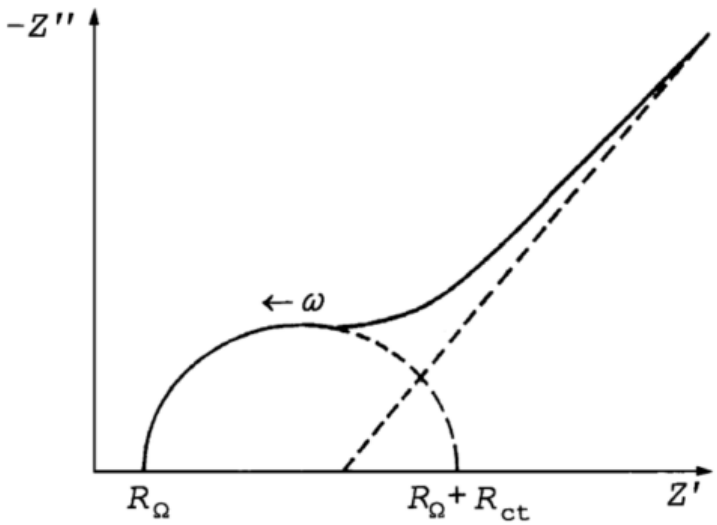

Figure 2.10: A schematic of a Nyquist plot. R_Ω is the high frequency series resistance, $\$R_{ct}$ is the charge transfer resistance, Z' is the real component of the impedance, and Z'' is the imaginary component of the impedance. ω indicates the direction of increasing frequency. The figure is retrieved from [53].

where R_Ω is the high frequency series resistance, R_{ct} is the charge transfer resistance, Z' is the real component of Z, and Z'' is the imaginary component of Z, and ω indicates the direction of increasing frequency.

Chapter 3

Experimental

3.1 Chemicals

Table 3.1 shows the chemicals used in the synthesis processes.

Table 3.1: Overview of the chemicals used in the synthesis processes.

Chemical	**Chemical formula**	**Producer**	**Purity**
Lithium nitrate	$LiNO_3$	Sigma-Aldrich	99 %
Nickel(II)acetate tetrahydrate	$Ni(CH_3CO_2)_2 \cdot 4\,H_2O$	Sigma-Aldrich	99.998 %
Manganese(II)nitrate tetrahydrate	$Mn(NO_3)_2 \cdot 4\,H_2O$	Sigma-Aldrich	97.5 %
Cobalt(II)acetate tetrahydrate	$Co(CH_3CO_2)_2 \cdot 4\,H_2O$	Sigma-Aldrich	98 %
Nickel(II)chloride	$NiCl_2$	Glencore Nikkelverk AS	*
Cobalt(II)chloride	$CoCl_2$	Glencore Nikkelverk AS	*
Ammonium hydroxide	NH_4OH	VWR International	29.1 %
Aluminium nitrate nonahydrate	$Al(NO_3) \cdot {}_9H_2O$	Sigma-Aldrich	99 %
Ammonium phosphate dibasic	$(NH_4)_2HPO_4$	Sigma-Aldrich	98 %
1-Ethyl-2-pyrrolidone	$C_6H_{11}NO$	Sigma-Aldrich	98 %
Polyvinylidene difluoride	$-(C_2H_2F_2)_n-$	Solvay	*
Carbon black	C	Imerys	*

* No specific purity was given for the chemical.

3.2 Pechini Method

The first batch was synthesised using the Pechini method. The precursor chemicals used for the synthesis was $LiNO_3$, $NiCl_2$, $Mn(NO_3)_2 \cdot 4\,H_2O$, and $CoCl_2$. $LiNO_3$ and $Mn(NO_3)_2 \cdot 4\,H_2O$ was supplied by Sigma-Aldrich, while $NiCl_2$ and $CoCl_2$ was supplied by Glencore, and the batch is therefore referred to as Pechini Method Glencore (PMGC). In order to obtain a stochiometrically correct product, the desired relationship between the precursor chemicals was 5:3:1:1, for lithium, nickel, manganese and cobalt precursors, respectively. However, to avoid cation mixing, a 5% excess of $LiNO_3$ was added. The target and measured amount of each chemical are shown in Table 3.2. $LiNO_3$ and $Mn(NO_3)_2 \cdot 4\,H_2O$ was weighed in powder state, and was dissolved in deionised water (DIW). $NiCl_2$ and $CoCl_2$ was measured in liquid state. Citric acid was added to each individual precursor solution in a ratio of 2 moles citric acid to 1 mole of the respective transition metal precursor. All precursor solutions initially had low pH, and NH_4OH was used to increase the pH of all individual solutions to 7. HNO_3 was used in order to decrease the pH to 7 after adding slight excess of NH_4OH.

Table 3.2: Overview of the target and measured amounts of the chemicals used in synthesis of PMGC.

Chemical	**Target amount [mol]**	**Target weight or volume**	**Measured weight or volume**	**Citric acid [g]**
$LiNO_3$	0.0542	3.73 g	3.74 g	20.82
$NiCl_2$	0.0310	22.54 mL	22.54 mL	11.89
$Mn(NO_3)_2 \cdot 4\,H_2O$	0.0103	2.59 g	2.59 g	3.96
$CoCl_2$	0.0103	6.73 mL	6.73 mL	3.97

The precursor solutions were mixed in a glass beaker, and stirred using a magnetic stirrer at 80 °C for 44 hours. At this point, the solution had formed a rigid gel network. The gel was dried in an oven at 220 °C in air for 24 hours. This heat treatment resulted in a dramatic expansion of the gel structure, increasing the volume of the gel by a factor of 4. The gel was crushed and mortared using a mortar and pestle, and subsequently precalcined in a calcination oven at 480 °C in air for 5 hours. The powder was once again mortared, and calcined in a vertical tube furnace at 800 °C in synthetic air for 15 hours. Finally, the powder was mortared one final time before characterisation. Due to unsatisfactory results from characterisation, the Pechini method synthesis was not repeated with nickel and cobalt precursors from Sigma-Aldrich.

3.3 Co-precipitation Synthesis

Two different batches were made using co-precipitation synthesis. Both batches used $LiNO_3$ and $Mn(NO_3)_2 \cdot 4\,H_2O$ as lithium and manganese precursors, but the

precursors used for nickel and cobalt differ between the two. The first batch used $NiCl_2$ and $CoCl_2$ precursors from Glencore, and is referred to as Co-Precipitation Glencore (CPGC). The second batch $Ni(CH_3CO_2)_2 \cdot 4\,H_2O$ and $Co(CH_3CO_2)_2 \cdot 4\,H_2O$ precursors from Sigma-Aldrich, and is referred to as Co-Precipitation Sigma-Aldrich (CPSA). The target and measured amounts used of each chemical during synthesis of CPGC and CPSA are shown in Tables 3.3 and 3.4, respectively.

Table 3.3: Overview of the target and measured amount used of each transition metal precursor in the synthesis of CPGC.

Chemical	**Target amount [mol]**	**Target weight or volume**	**Measured weight or volume**
$NiCl_2$	0.003	21.84 mL	21.84 mL
$Mn(NO_3)_2 \cdot 4\,H_2O$	0.001	2.51 g	2.51 g
$CoCl_2$	0.001	6.52 mL	6.52 mL

Table 3.4: Overview of the target and measured amount used of each transition metal precursor in the synthesis of CPSA.

Chemical	**Target amount [mol]**	**Target weight [g]**	**Measured weight [g]**
$Ni(CH_3CO_2)_2 \cdot 4\,H_2O$	0.03	7.47	7.47
$Mn(NO_3)_2 \cdot 4\,H_2O$	0.01	2.51	2.
$Co(CH_3CO_2)_2 \cdot 4\,H_2O$	0.01	2.49	2.49

The synthesis for both co-precipitation batches were performed by dissolving $Mn(NO_3)_2 \cdot 4\,H_2O$ in DIW and mixing it with nickel and cobalt precursors in a glass beaker and stirred with a magnetic stirrer. The colour of the precursor solution mix was green. 29.85 mL of 29.1% NH_4OH was diluted to 200 mL with DIW, and put in a tree-neck round bottom glass flask, which was partially submerged in a glass beaker filled with water. The amount of ammonia used was based on Hu et. al [55], which indicates an optimal molar relationship of ammonia to transition metal precursors of 2.7. The glass beaker was put on a magnetic stirrer, and a magnet was placed in the NH_4OH solution. The magnetic stirrer was set to keep the water at 50 °C, and the magnet rotating at an rpm of 750. Nitrogen gas was bubbled into the ammonia solution through a small tube to reduce the oxygen content in the atmosphere of the glass flask. A pH-meter was kept in the glass bottle in order to continually measure the pH and the temperature of the solution. The solution of the mixed transition metals was put in a dropping funnel above the glass flask of ammonia solution. This solution was slowly dripped into the ammonia solution, while continuously measuring the pH, and manually adding 4M NaOH with a plastic pipette in order to keep the pH above 11. Initially, the clear ammonia solution turned a matt turquoise colour after dripping some of the precursor solution into

it, but after adding more of the precursor solution, the solution in the glass flask turned brown with visible brown precipitate particles. These particles were presumably the desired hydroxide material $Ni_{0.6}Mn_{0.2}Co_{0.2}(OH)_2$. The solution was stirred overnight, while keeping temperature at 50 °C and continuously bubbling nitrogen gas.

The solution was then filtrated using a Büchner funnel and corresponding Whatman Blue ribbon ashless filter paper circles with pore size smaller than 2 μm. The particles remaining on the filter paper was washed five times with 200 mL DIW in order to wash away any ammonia residue. Due to potential problems caused by chloride in a battery environment, the CPGC particles were additionally washed several times in order to completely remove chloride ions from the particles. Remaining chloride was detected by adding $AgNO_3$ to the filtrate, and then observing whether precipitation of AgCl occurred. The filtrate was continually removed and retested with $AgNO_3$ in each wash cycle, and after 15 times, no further precipitation of AgCl was observed. Both powders were then dried in a vacuum oven overnight at 90 °C. Next, the particles were removed from the filter paper, and ground by a mortar and pestle.

A portion of the powders were weighed, and an appropriate amount of $LiNO_3$, corresponding to a molar relationship of $LiNO_3$ to transition metals of 1.05:1 was weighed and mixed with the $Ni_{0.6}Mn_{0.2}Co_{0.2}(OH)_2$ powder using a mortar and pestle. The powders were precalcined at a temperature of 480 °C for 5 hours in a calcination furnace, and ground again with a mortar and pestle. Finally, the powders were calcined in a vertical tube furnace at 800 °C for 15 hours, and then ground with a mortar and pestle. Only a portion of the $Ni_{0.6}Mn_{0.2}Co_{0.2}(OH)_2$ powders were processed into NMC622 due to the desire of characterising the initial hydroxide powders along with the precalcined and calcined NMC622 powders. This was done in order to study the morphological and structural properties of each step in the synthesis.

3.4 $AlPO_4$ Coating of Particles

1 g of the calcined CPSA powder was then coated with $AlPO_4$. CPSA was chosen for the coating procedure, in stead of CPGC, due to promising results from galvanostatic charge-discharge cycling of the CPSA coin cells. The procedure was performed using a precipitation coating method, where the NMC particles act as heterogeneous nucleation sites during precipitation of $AlPO_4$. 0.040 g of $Al(NO_3)\cdot_9H_2O$ and the 1 g of CPSA powder was mixed with 10 mL of DIW in a glass beaker and stirred for 30 minutes. 0.014 g of $(NH_4)_2HPO_4$ was mixed with 10 mL of DIW in another glass beaker and stirred for 30 minutes. The $(NH_4)_2HPO_4$ solution was then put in a dropping funnel and slowly dripped into the NMC and $Al(NO_3)\cdot_9H_2O$ solution while stirring 600 rpm. The solution was allowed to stir for 3h at 60 °C, before inserting the solution into a vacuum oven in order to evaporate the remaining water and drying the powder overnight. Next, the dry powder was crushed with a mortar and pestle, and inserted into a calcination oven at 500 °C for 1 hour, to allow any nitrates and ammonia to be burned off from the sample. The

powder was then once again ground with a mortar and pestle, and taken for characterisation and further processing. The resulting $AlPO_4$ coated NMC powder will from now be referred to as Aluminium phosphate Co-Precipitation Sigma-Aldrich (AL-CPSA).

3.5 Powder Characterisation

XRD measurements were performed on the CPSA and CPGC powders at different stages in the synthesis process. The first measurement was performed prior to mixing with $LiNO_3$. The second measurement was performed after mixing the oxide powders with $LiNO_3$ and their respective precalcination treatment, but prior to calcination. The third measurement was performed after the final calcination step. The final measurement was performed on AL-CPSA, after its respective final heat treatment. All measurements were performed with the same instrument and parameters; a D8 A25 DaVinci X-ray Diffractometer with Cu-Kα radiation, scanning across 2Θ angles 10-75 ˚ for 30 minutes with a slit size of 0.2 nm. The powders were prepared in a sample holder and covered by Kapton tape, due to the toxic nature of the materials. The resulting X-ray diffractograms from these scans were mainly used qualitatively in order to determine if the synthesised powders were suitable for further processing into cathodes.

Additional scans were performed on the finished CPGC, CPSA and AL-CPSA powders for improved XRD data. The scans were performed across 2Θ angles of 10-110 ˚ over 6 hours, with a 0.2 nm slit size. For these scans, CPGC and CPSA were covered with Kapton tape, but due to shortage of remaining AL-CPSA powder, the remaining powder was suspended in ethanol, and dripped onto a monocrystalline silicon sample holder. The ethanol was dried prior to XRD measurements, and the resulting sample was not covered with Kapton tape due to the nature of the sample preparation. The resulting X-ray data and diffractograms were further processed and refined using the software TOPAS v5 in order to gain quantitative data on e.g. cation mixing and crystallite size.

The Rietveld refinements were performed by refining an increasing amount of parameters in TOPAS. In addition, three peak phases were used in refinement of the samples that had Kapton film, to improve background estimation at lower angles. First, lattice parameters a and c were refined, as well as scale factor. Next, partial occupation of nickel ions on lithium sites, and conversely, lithium ions on nickel sites were refined. Crystallite size and strain were then refined. The refinement was at this point still unsatisfactory, so several corrections were included in the refinements. These include sample displacement, surface roughness, absorption and sample tilt. Finally, two preferred orientations were included, for the (003) and (104) crystal planes, due to their significance for cation mixing.

A Zeiss Ultra, 55 Limited Edition field emission scanning electron microscope (FESEM) was employed to obtain images of the morphology of the powders. Images were obtained at the different synthesis stages for CPGC and CPSA, as described in the previous paragraph. AL-CPSA was also characterised using FESEM. The electron beam was set to 15 kV, and secondary electrons were used for signal

detection. The working distance was kept constant at 10.0 mm for all images, allowing for comparison between images at identical magnifications. FIJI [56], a distribution of ImageJ [57], was employed to refine the SEM images.

For the purpose of performing a BET surface area analysis, 1.1288 g, 1.1054 g, and 0.9878 g of CPGC, CPSA and AL-CPSA powders respectively, were degassed in vacuum for 18 hours at 250 °C in glass tubes. All powders were then analysed using a TRISTAR 3000 surface area and porosity analyser instrument. Results of the specific surface area of the powders were employed to estimate average particle sizes according to Equation (2.14), using crystallographic density of NMC of 4.8 g/cm^2 [12].

3.6 Cathode Casting and Battery Assembly

Prior to the process of making cathode casts for CPGC, CPSA and AL-CPSA, three slurries were made by mixing 80 wt% of the respective NMC622 active cathode material powders with 10 wt% carbon black and 10 wt% polyvinylidene difluoride (PVDF) which were dispersed in a 1-ethyl-2-pyrrolidone (NEP) solvent. The added carbon black powder contributes to the conductivity of the cathode, while the PVDF particles act as binder material. The PVDF-NEP solution was made by mixing 1 g of PVDF particles with 19.01 g of NEP solvent, which was performed by Hans-Olav Meløy, a master student in the battery research group. Some extra NEP was added to each slurry in order to gain optimal viscosity. This is achieved at a relationship of NEP to solid material of 2:1. The measured amounts of NMC622 powders, carbon black, and PVDF/NEP used in each slurry are shown in Tables 3.5, 3.6, and 3.7 for CPGC, CPSA and AL-CPSA, respectively.

Table 3.5: Slurry content for CPGC.

Material	**Weight [g]**	**Target wt%**	**Actual wt%**	**Deviation wt%**
$LiNiMnCoO_2$	0.499	80	79.95	0.05
Carbon black	0.062	10	10.00	0.00
PVDF	0.063	10	10.05	0.05
NEP	1.254	-	-	-

Table 3.6: Slurry content for CPSA.

Material	**Weight [g]**	**Target wt%**	**Actual wt%**	**Deviation wt%**
$LiNiMnCoO_2$	0.500	80	79.85	0.15
Carbon black	0.063	10	9.98	0.02
PVDF	0.064	10	10.17	0.17
NEP	1.250	-	-	-

Table 3.7: Slurry content for AL-CPSA.

Material	**Weight [g]**	**Target wt%**	**Actual wt%**	**Deviation wt%**
$LiNiMnCoO_2$	0.507	80	80.10	0.10
Carbon black	0.063	10	9.92	0.08
PVDF	0.063	10	9.98	0.02
NEP	1.267	-	-	-

The slurry was mixed in a 10 mL shaker mill jar on a shaker mill at a frequency of 25 Hz for 30 minutes. The slurry was then deposited in a line onto a sheet of 25 μm aluminium foil, with a trace metals basis of 99.45%. A slip caster with a height of 100 μm was then manually dragged across the aluminium foil at a constant speed, smearing the line of slurry into an even film across the foil surface. The cathode cast was dried in a heating cabinet at 90 °C overnight in order to evaporate most of the NEP solvent. The casts were then dried in a vacuum oven at 120 °C for 3 hours to make certain no humidity was left on the cathode cast surface.

An electrode cutter was employed to cut circular cathodes out of the cathode casts. Some samples of the aluminium foil, without cathode material, was also cut using the same electrode cutter in order to determine the average weight of aluminium in each cathode. The average weight of the aluminium samples was 13.80 g, with a standard deviation of 0.097 g. The cathodes were all assigned an ID by appending a number to the abbreviation of the active cathode material. The weight of the active cathode material in each cathode was determined by subtracting the average weight of the aluminium samples from the weight of each individual cathode and multiplying by the weight percentage of the active material. The measured and calculated weights of the cathodes and cathode active materials are shown in Table 3.8.

The cathodes were inserted in a glove box with argon atmosphere, where the atmospheric contents of O_2 and H_2O were constantly measured to be below 0.1 ppm. Coin cells were assembled by performing the following procedure. A cathode was inserted into the bottom of a CR2016 coin cell, inside a plastic ring which acts as a separator between the bottom and the lid of the coin cell. Next, 20 μL of 1M LPF in 1:1 solution of EC:DEC electrolyte was applied on top of the cathode using an autopipette. A Celgard 2320 20 μm microporous trilayer membrane separator was then carefully placed on top of the cathode and electrolyte. Another 20 μL of electrolyte was then added on top of the separator. A strip of lithium metal was brushed to remove any impurities on the surface, and a circular anode was made by using a punching tool to cut out a disk of metal. This disk was then attached to a spacer disk, and added on top of the coin cell, with the lithium metal facing down towards the electrolyte. Finally, the lid was placed on top of the spacer disk, and the coin cell was inserted into a crimping machine for sealing of the cell. The coin cell assembly was performed for five cathodes from each batch, while the two remaining cathodes were put aside for subsequent characterisation by SEM and XRD.

Table 3.8: The measured weight of the cathodes for CPGC, CPSA and AL-CPSA, and the calculated weight of active material in each cathode.

Cathode ID	Cathode weight [mg]	Active material weight [mg]
CPGC1	16.42	2.10
CPGC2	16.41	2.09
CPGC3	16.72	2.34
CPGC4	16.88	2.46
CPGC5	17.51	2.97
CPGC6	16.98	2.54
CPGC7	17.33	2.82
CPSA1	17.66	3.09
CPSA2	17.83	3.22
CPSA3	17.80	3.20
CPSA4	16.99	2.55
CPSA5	18.18	3.50
CPSA6	18.81	4.01
CPSA7	17.68	3.10
AL-CPSA1	19.28	4.38
AL-CPSA2	18.82	4.02
AL-CPSA3	19.27	4.38
AL-CPSA4	19.53	4.58
AL-CPSA5	19.34	4.43

3.7 Electrochemical Characterisation

Directly after assembling the coin cells and removing them from the glove box, the coin cells were characterised by electrochemical impedance spectroscopy on a potensiostat, using EC-Lab software. A potentio electrochemical impedance spectroscopy (PEIS) technique was used, with a voltage perturbation amplitude of 10 mV, scanning across a frequency range of 200 kHz 100 mHz.

Next, galvanostatic charge-discharge cycling was performed on the cells. All coin cells were allowed to rest for at least 10 hours before cycling. Three coin cells from each batch followed the same program by cycling one time at a charge/discharge rate of 0.1C, before they were set to cycle 200 times at 0.2 C. Two coin cells from each batch were used for a rate-capability test by cycling five times each on different C-rates, namely 0.1 C, 0.2 C, 0.5 C, 1 C, 2 C, and finally back to the starting rate of 0.1 C. Table 3.9 shows an overview over what cycling program was used for which cell. During cycling, cut-off voltages were set to 2.5 V and 4.3 V as lower and upper limits, respectively. The lower limit should have been set to a higher potential, such as e.g. 3 V, but due to the first cells being cycled with a lower limit of 2.5 V, the same lower limit was used for all cells for consistency. Most cells did not complete 200 cycles for varying reasons, such as insufficient time or cell

breakdown.

Table 3.9: Overview of galvanostatic charge-discharge cycling tests performed on each coin cell. For rate-capability tests, the C-rate of the initial and final cycles are included in parenthesis.

Coin cell ID	**Test performed**
CPSA1	0.2C, 93 cycles
CPSA2	0.2C, 200 cycles
CPSA4	0.2C, 106 cycles
CPSA5	Rate-capability (0.1C)
CPSA6	Rate-capability (0.1C)
CPSA6 #2	Rate-capability (0.2C)
CPGC1	Rate-capability (0.1C)
CPGC2	0.2C, 80 cycles
CPGC3	0.2C, 89 cycles
CPGC4	0.2C, 92 cycles
CPGC5	Rate-capability (0.1C)
AL-CPSA1	0.2C, 30 cycles
AL-CPSA2	0.2C, 46 cycles
AL-CPSA3	0.2C, 51 cycles
AL-CPSA4	Rate-capability (0.1C)
AL-CPSA5	Rate-capability (0.1C)

3.8 Post-mortem Characterisation

After cycling, two coin cells, CPGC3 and CPSA2, were disassembled in order to perform post-mortem SEM characterisation of the cathodes. For comparison, two corresponding, unused cathodes were also subjected to the same characterisation technique. Images of the cathode surfaces, and of the aluminium current collector were captured. A pure sample of unused aluminium was also imaged for comparison with the current collector of the cycled cathodes.

Chapter 4

Results

This chapter presents results obtained from the range of characterisation techniques used throughout the experimental work in this thesis. In order to keep the results section concise, a selection of representative results are presented, while additional results and information is included in the appendices A-E. To accomplish this, the results focus on presenting differences between CPGC, CPSA and AL-CPSA, as well as between certain parameters, such as comparisons of cells prior to and after cycling.

4.1 Powder Characterisation

This section presents results obtained from SEM, XRD and BET characterisation of the synthesised powders prior to their processing to cathodes.

4.1.1 Scanning Electron Microscopy

FESEM images of calcined CPGC, CPSA and AL-CPSA powders are shown in Figure A.1. Images (a), (c) and (e) are overview images at intermediate magnifications, and show how the crystallites have partially agglomerated, especially for CPGC and AL-CPSA. Images (b), (d) and (f) are detail images whit high magnifications, and show the crystallites of the powders. The crystallites have a slight spherical shape. Additional images of the powders at different magnifications are included in Appendix A.

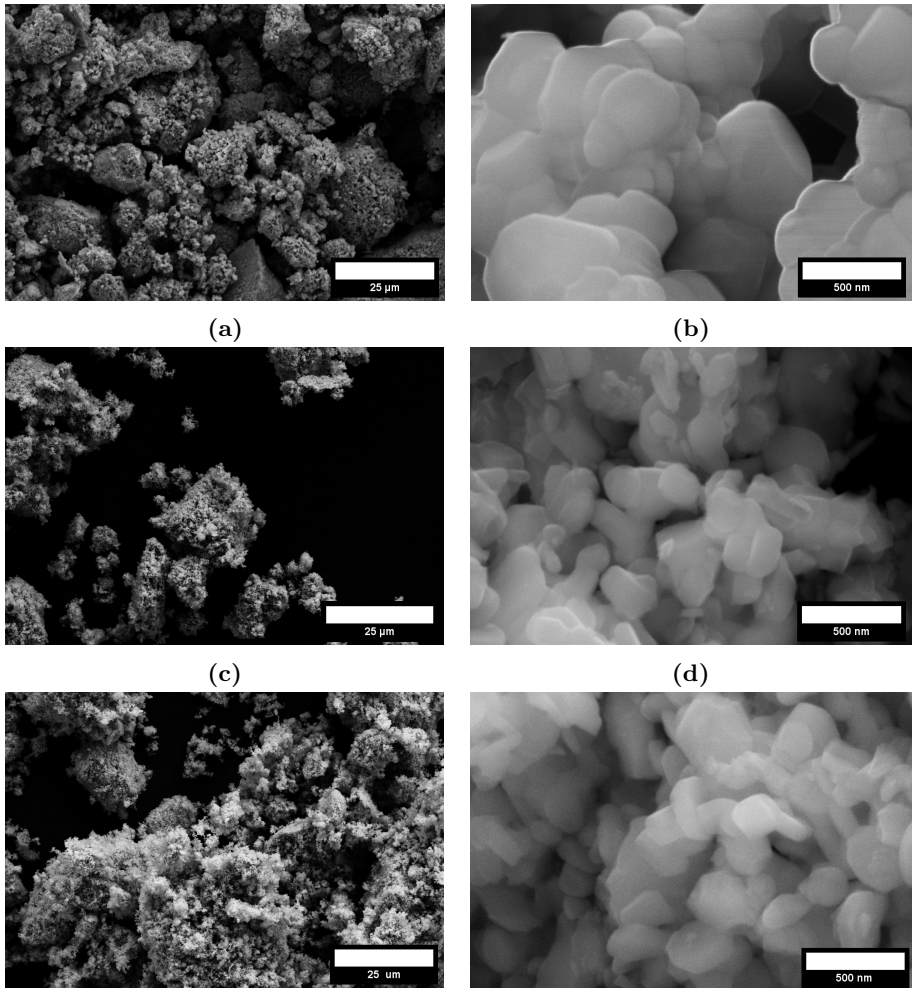

Figure 4.1: SEM images of calcined CPGC (a) & (b), calcined CPSA (c) & (d), and AL-CPSA (e) & (f) powders.

4.1.2 X-Ray Diffraction

The X-ray diffractogram for PMGC is shown in Figure 4.2. The hkl reference lines for theoretical Bragg peaks of the NMC structure are shown in black in the figure, and a large disparity between the reference lines and the XRD peaks for PMGC is observed. A comparison of the X-ray diffractograms of the 6 hour scans of CPGC, CPSA and ALCPSA powders is shown in Figure 4.3 in green, blue and red, respectively. The relevant Bragg peaks, as described in section 2.3, have been indicated by including the hkl values of the crystal planes they correspond to. The different materials have very similar diffractograms, and they all match up well with the hkl reference lines of the desired main phase, which indicates that the materials are phase pure. A Rietveld-refined X-ray diffractogram of CPGC is shown in Figure 4.4, where the measured values are shown in blue, the calculated values are shown in red, and the difference between these are shown in grey. The figure also includes reference hkl peak positions for NMC622, shown as black vertical lines. Figure B.1 shows a comparison between 30 minute XRD scans for CPGC at different synthesis stages, where uncalcined powder is showed in green, precalcined in red, and calcined in blue. The NMC622 reference lines are shown in black. The four asterisks indicate unexpected peaks in the diffractogram of precalcined CPGC powder. The XRD database confirmed that the peaks corresponded to lithium nitrate.

Rietveld refined XRD plots of CPSA and AL-CPSA are included in Appendix B. The appendix further includes plots of XRD scans of CPSA at different synthesis stages.

Rietveld refinement revealed particle size, lattice parameters and degree of cation mixing for the powders. The results are shown in Table 4.1. They indicate that the crystallite size is smallest for CPGC, slightly larger for CPSA, and even larger for AL-CPSA. 1.15 % cation mixing was detected for CPGC, while CPSA and AL-CPSA showed no sign of cation mixing.

Table 4.1: Results from X-ray diffraction measurements of CPGC, CPSA and AL-CPSA powders. Degree of cation mixing is the percentage of lithium ions on nickel sites and nickel ions on lithium sites. The R-factor R_{wp} is a weighted-profile factor indicating how well the Rietveld refinement fits the experimental data.

Powder ID	CPGC	CPSA	AL-CPSA
Crystallite Size [nm]	126	170	420
Lattice Parameter a [Å]	2.865(7)	2.865(4)	2.867(3)
Lattice Parameter c [Å]	14.194(4)	14.203(2)	14.205(2)
Degree of Cation Mixing [%]	1.15	0	0
R-Factor R_{wp}	4.83	5.87	5.46

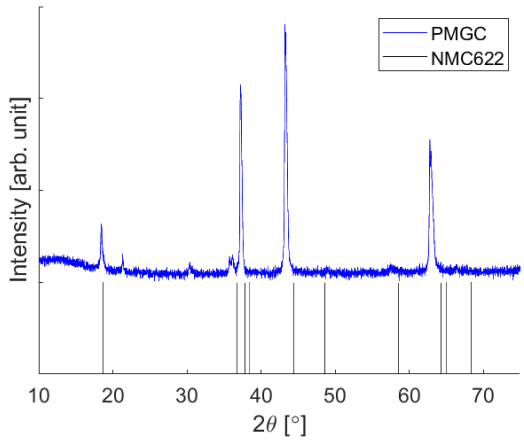

Figure 4.2: X-Ray Diffractogram of a 30 minute scan of PMGC powder. The black lines indicate reference peaks for NMC622.

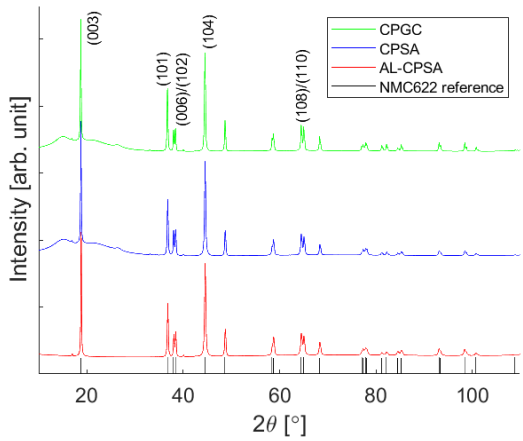

Figure 4.3: X-Ray Diffractograms of 6 hour scans of CPGC, CPSA, and AL-CPSA powders, plotted in green, blue and red, respectively. The black lines indicate reference peaks for NMC622. The relevant Bragg peaks have been indicated by including the hkl values of the crystal planes they correspond to, and are valid for all three powders.

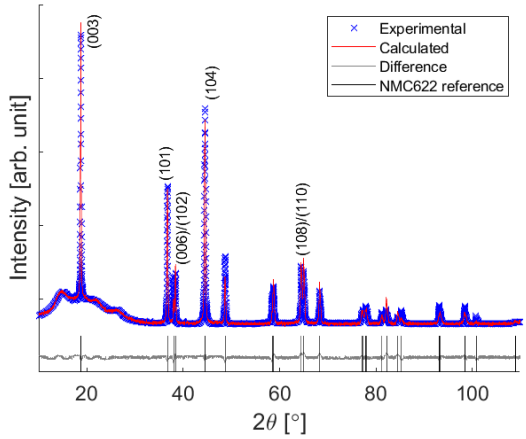

Figure 4.4: Rietveld refined X-ray diffractogram of CPGC powder. The measured values are shown in blue, calculated values are shown in red, and the difference between measured and calculated values is shown in grey. The black lines indicate reference peaks for NMC622. The relevant Bragg peaks have been indicated by including the hkl values of the crystal planes they correspond to.

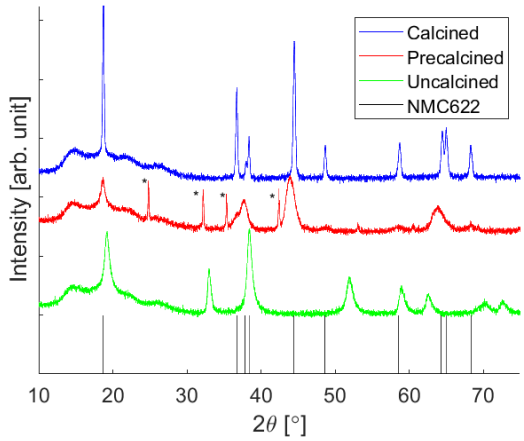

Figure 4.5: X-Ray Diffractograms of 30 minute scans of CPGC at different stages. Uncalcined powder is shown in green, precalcined powder is showed in red, and calcined powder is shown in blue. The black lines indicate reference peaks for NMC622. The asterisks indicate peaks corresponding to lithium nitrate in the precalcined powder.

4.1.3 Brunauer-Emmet-Teller Surface Area Analysis

BET surface area analysis results are summarised in Table 4.2. Full reports on data obtained from BET analysis are included in Appendix E. The results show that the SSA is smaller for CPGC than for CPSA by an order of magnitude. AL-CPSA has a slightly larger SSA than CPSA. Accordingly, the average particle size is smallest for AL-CPSA, slightly larger for CPSA, and larger by an order of magnitude for CPGC.

Table 4.2: Results from BET measurements of CPGC, CPSA and ALCPSA powders. Mass is the mass of each powder used for the measurement, BET SSA is the BET specific surface area, and the average particle size is calculated by using Equation (2.14).

Powder ID	**Mass [g]**	**BET SSA [m^2/g]**	**Average Particle Size [μm]**
CPGC	1.1288	0.35	3.54
CPSA	1.1054	3.41	0.37
ALCPSA	0.9878	5.66	0.22

4.2 Cathode Characterisation

This section presents SEM results from imaging cathodes prior to and after cycling. In Figure 4.6, overview and detail images are shown for a CPGC cathode prior to and after cycling. Little difference can be seen between these. Images (e) and (f) show unused aluminium foil, and aluminium foil which was part of the current collector in a CPGC coin cell. Image (f) shows more contamination on the foil than image (e), but does not show deterioration of the foil due to oxidation. Additional SEM images of the cathodes are included in Appendix A.

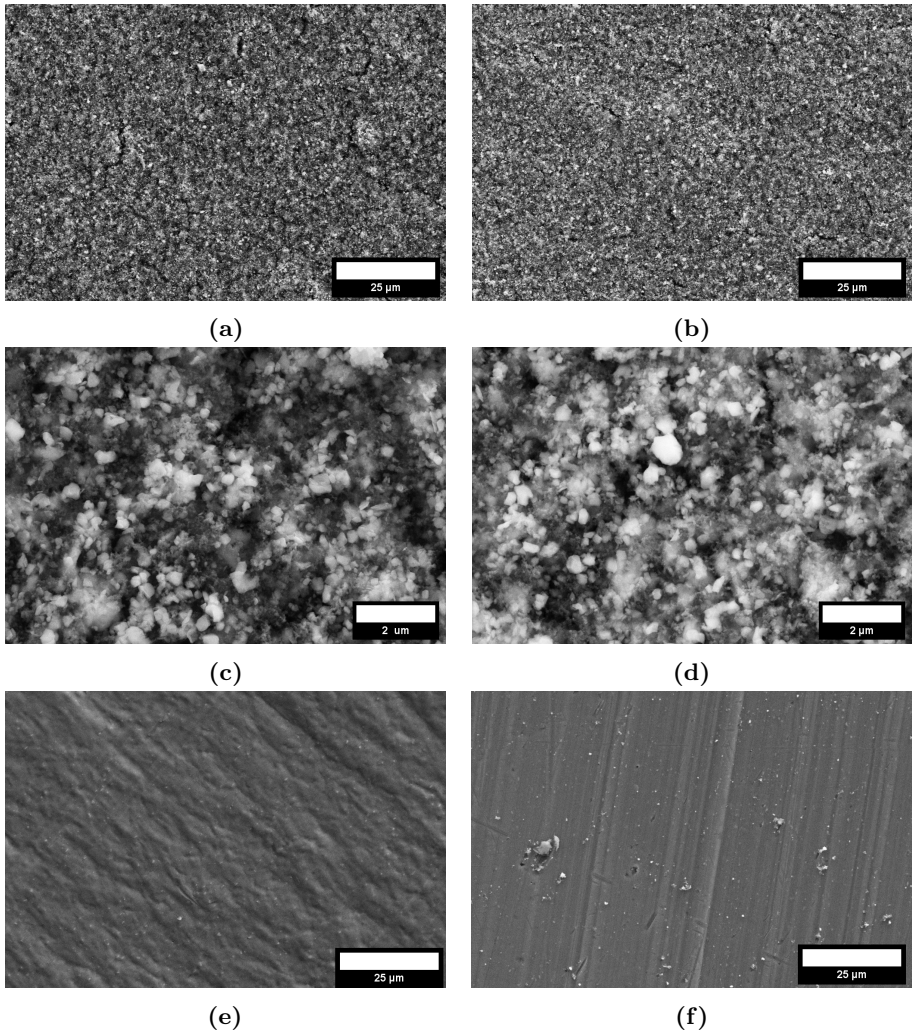

Figure 4.6: SEM images of a CPGC cathode pre cycling (a) & (c) and a CPGC cathode post cycling (b) & (d). Image (e) shows unused aluminium foil, and image (f) shows aluminium current collector of a CPGC cathode post cycling.

4.3 Electrochemical Characterisation

In this section, results from EIS prior to and after cycling will be presented as Nyquist plots, as well as calculated resistances from polynomial fitting of these plots. Results from galvanostatic charge-discharge cycling are also presented by several different plots, which highlight capacities, capacity retention and differential capacity of the coin cells.

4.3.1 Electrochemical Impedance Spectroscopy

Estimated series resistances and charge transfer resistances, including standard errors, from polynomial fitting of experimental data are shown in Table 4.3. All cells show similar high-frequency series resistance, which does not change much after cycling. There are differences in the charge transfer resistances of the coin cells, where CPGC shows low resistance, CPSA shows intermediate resistance, and AL-CPSA shows high resistance. There is also a difference in charge transfer resistance after cycling, where some cells display an increase in the resistance, while other cells display a decrease.

Nyquist plots of imaginary vs. real resistance as a function of frequency, as well as fourth degree polynomial fitting of experimental data for CPGC5, CPSA5, and AL-CPSA5 are shown in Figure 4.7. Corresponding Nyquist plots for the remaining coin cells are included in Appendix C. In Figure 4.7, the semi-circle shape at high frequencies is apparent for all coin cells. At low frequencies the measurements become erratic for CPGC and CPSA prior to cycling, but after cycling, this is seen for all coin cells.

Table 4.3: Estimated series and charge transfer resistance, including standard error, of coin cells prior to and after cycling. Dashes (-) indicate that no measurement was performed, and asterisks (*) indicate that measurements were performed, but data was insufficient to provide estimates of resistances.

Coin cell ID	**Series resistance before cycling** [Ω]	**Series resistance after cycling** [Ω]	**Charge transfer resistance before cycling** [Ω]	**Charge transfer resistance after cycling** [Ω]
CPGC1	*	-	*	-
CPGC2	3.2 ± 0.7	3.6 ± 0.8	48.8 ± 1.0	90.4 ± 2.6
CPGC3	2.4 ± 0.8	-	61.2 ± 1.3	-
CPGC4	2.8 ± 0.7	-	54.4 ± 1.0	-
CPGC5	2.8 ± 0.7	3.2 ± 0.1	52.0 ± 1.0	47.6 ± 0.4
CPSA1	2.4 ± 1.8	*	114.4 ± 3.1	*
CPSA2	2.4 ± 1.3	-	88.4 ± 2.1	-
CPSA4	-	3.2 ± 1.2	-	172.8 ± 32.2
CPSA5	2.8 ± 1.7	2.8 ± 1.9	93.2 ± 2.4	149.2 ± 12.5
CPSA6	2.4 ± 1.8	2.4 ± 1.7	129.2 ± 3.4	159.2 ± 16.6
AL-CPSA1	2.0 ± 1.9	2.0 ± 1.7	147.6 ± 4.0	151.6 ± 6.5
AL-CPSA2	0.0 ± 1.7	-	187.6 ± 4.3	-
AL-CPSA3	3.2 ±1.1	3.6 ± 0.45	114.0 ± 2.3	65.6 ± 1.9
AL-CPSA4	3.2 ± 1.5	2.8 ± 1.0	124.0 ± 2.4	113.2 ± 4.3
AL-CPSA5	1.6 ± 2.3	2.4 ± 0.54	193.2 ± 9.1	108.0 ± 3.0

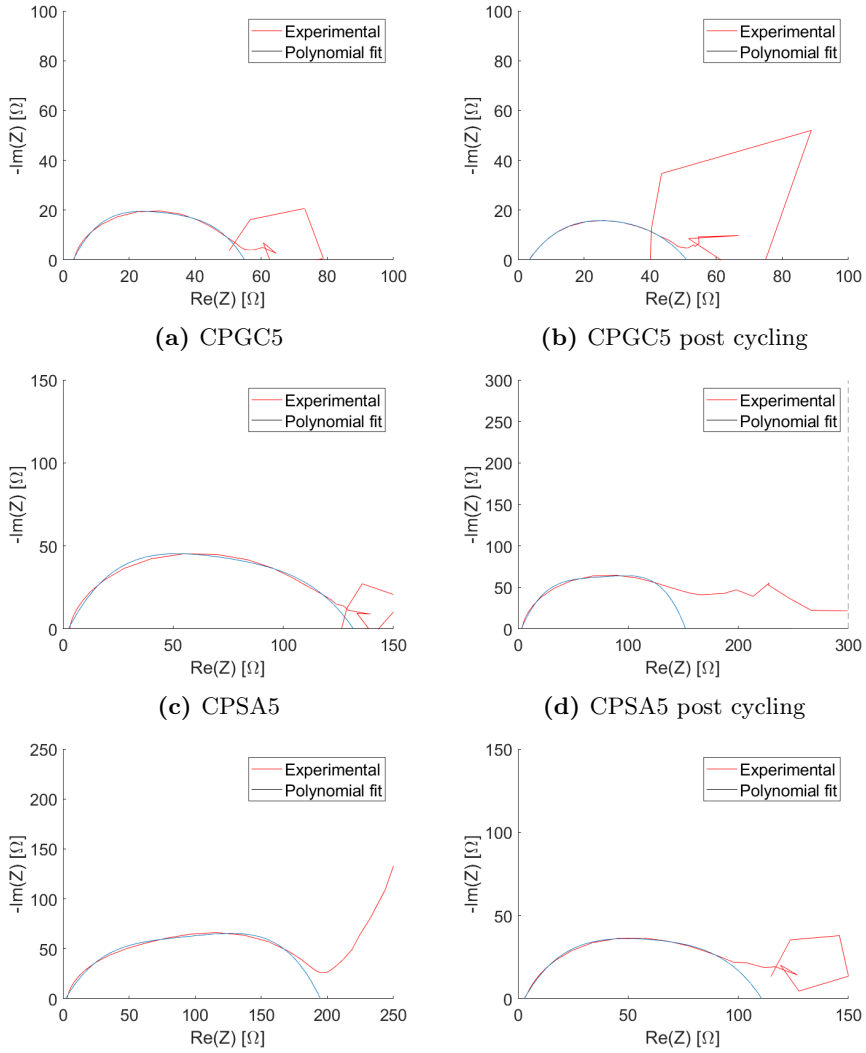

(a) CPGC5

(b) CPGC5 post cycling

(c) CPSA5

(d) CPSA5 post cycling

(e) AL-CPSA5

(f) AL-CPSA5 post cycling

Figure 4.7: Results from electrochemical impedance spectroscopy for CPGC1, CPGC3, CPGC2, CPGC2 post cycling, CPGC4 and AL-CPSA2.

4.3.2 Galvanostatic Charge-Discharge Cycling

Figure 4.9 shows results from galvanostatic cycling for CPGC2, CPSA2, and AL-CPSA2. The left-hand side images of the figure, (a), (c) and (e), show plots of cell voltage as a function of specific capacity for each coin cell at specific cycle numbers. The charge and discharge curves display the expected shapes, with a small incline/decline at approximately 3.8 V. For CPGC2, anomalies are seen for

cycles 25 and 50, while for CPSA2 and AL-CPSA2 this is not seen. The right-hand side images of the figure, (b), (d) and (e), show charge and discharge specific capacity as well as Coulombic efficiency as a function of cycle number for the coin cells. The anomalies seen at cycles 25 and 50 on the left hand side is accompanied by erratic capacities and Coulombic efficiencies for cycles beyond the 25th cycle for CPGC. It is mostly the charge capacities that deviates from the trend for CPGC2. For CPSA2 and AL-CPSA2, trends are much clearer than for CPGC2. Plots of cycling data for the remaining coin cells are included in Appendix D.

Figure 4.8 shows plots of differential capacity as a function of cell voltage vs. Li/Li^+ for CPSA3 and AL-CPSA3. Plots of differential capacity for CPSA1, CPSA2, AL-CPSA1 and AL-CPSA2 are included in Appendix D. No differential capacity plots were able to be generated for CPGC coin cells due to insufficient cycling data. In Figure 4.8, two distinct peaks protrude during charging cycles of the cell. A small contraction of the area underneath the curves can be observed with increasing cycle number. Furthermore, the peaks during charge cycles move slightly towards higher voltages with increasing cycle number, and peaks during discharge cycles move slighly towards lower voltage with increasing cycle number.

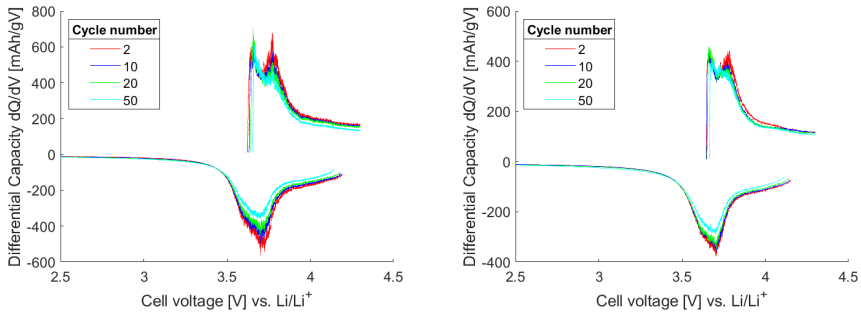

(a) CPSA3 **(b)** AL-CPSA3

Figure 4.8: Differential capacity plots as a function of cell voltage vs. Li/Li^+ for CPSA3 (a) and AL-CPSA3 (b).

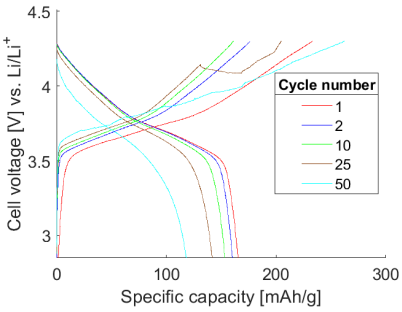

(a) CPGC2

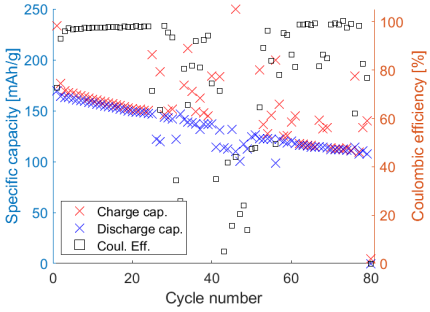

(b) CPGC2

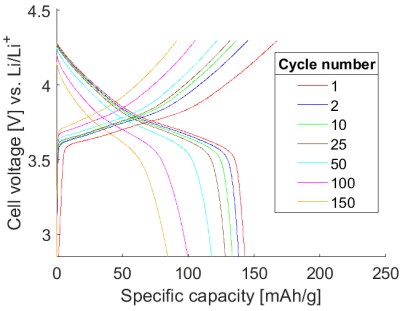

(c) CPSA2

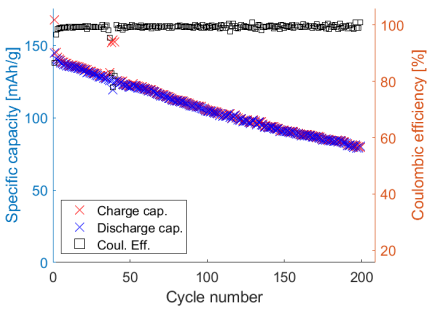

(d) CPSA2

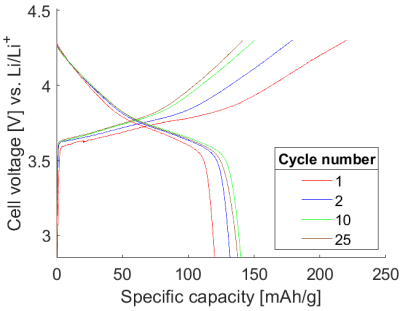

(e) AL-CPSA2

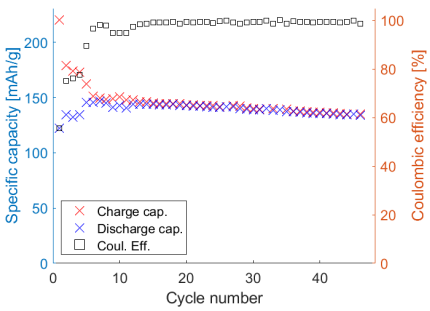

(f) AL-CPSA2

Figure 4.9: Figures on the left show cycling data as plots of voltage as a function of specific capacity for coin cells CPGC2 (a), CPSA2 (c) and AL-CPSA2 (e). Figures on the right show specific charge and discharge capacity as well as Coulombic efficiency as a function of cycle number for CPGC2 (b), CPSA2 (d) and AL-CPSA2 (f).

4.3.3 Rate Capability Cycling

Figure 4.10 shows cycling data for CPSA6 subjected to two different rate capability tests. Plot (a) and (c) show cell voltages as functions of specific capacities for rate capability cycling of CPSA6, starting and ending at 0.1C and 0.2C, respectively. Plots (b) and (d) show specific charge and discharge capacities as well as Coulombic efficiencies as a function of cycle numbers for different rate capability tests of CPSA6. For the rate capability test starting at 0.1C, cycles 3, 26 and 27, i.e. three of the cycles at 0.1C indicate some cell malfuntion, resulting in specific capacities way above theoretically possible. Plots for the other coin cells subjected to rate-capability cycling are included in Appendix D.

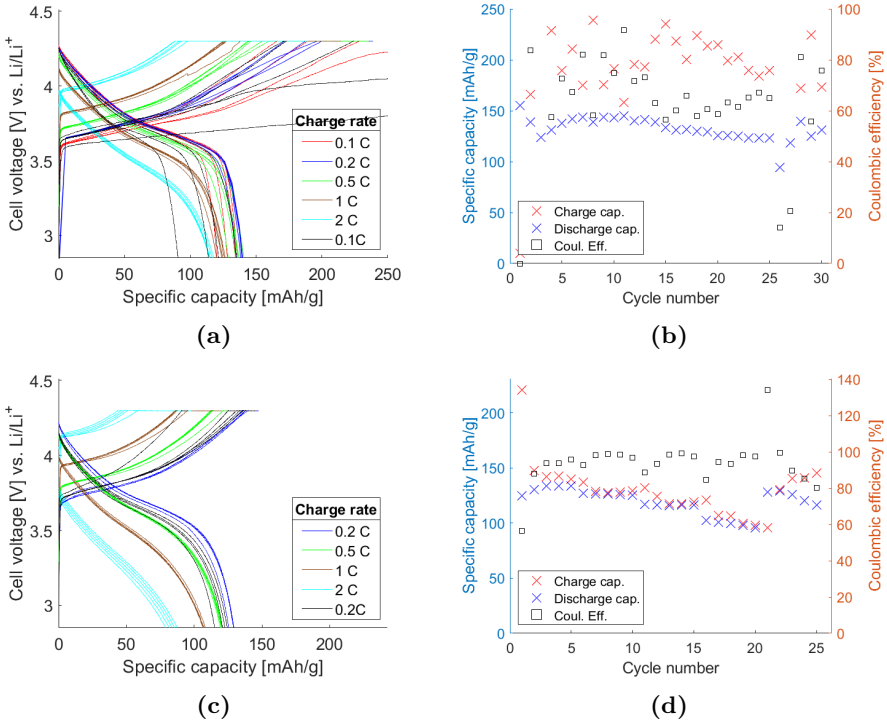

Figure 4.10: Figure (a) and (b) show rate-capability cycling of CPSA6 from 0.1C through 0.2C, 0.5C, 1C, 2C, back to 0.1C with different scales on the x-axis. Figure (c) and (d) show rate-capability cycling of CPSA6 from 0.2C through 0.5C, 1C, 2C, back to 0.2C.

Chapter 5

Discussion

5.1 Powder Synthesis and Characterisation

5.1.1 Pechini Method

Although the synthesis procedure of PMGC seemed to be succesful, the XRD results of the powder in Figure 4.2 showed that the powder did not have the desired layered $R\bar{3}m$ crystal structure. The disparity between the reference lines and the Bragg peaks indicates that one or several phases other than the desired structure had been formed. No exact match was found with the database, but some peaks seemed to match to a certain degree with different oxides such as e.g. NiO, Co_3O_4 and MnO_2. The Pechini method, used to synthesise cathodes from chloride solution precursors was expected to be difficult, as the synthesis method did not allow washing away chloride from the resulting powder. This was expected to cause problems if cathodes were made from the powder, and subsequently used in batteries due to potential side reactions between chloride ions and the electrolyte, electrodes or SEI. Therefore, when problems arose after initial characterisation of the powder, the synthesis method was immediately abandoned in favour of co-precipitation synthesis, which was expected to provide better results.

5.1.2 Co-Precipitation

The co-precipitation synthesis was deemed successful, as XRD results showed that phase pure NMC had been achieved for both CPGC and CPSA, with the desired $R\bar{3}m$ crystal structure. These powders were therefore further processed into batteries. Initial 30 minute XRD scans indicated a low degree of cation mixing, due to the high intensity ratio between the (003) and (104) Bragg peaks. As mentioned in Section 2.3, a ratio larger than 1.2 between the intensities of these planes indicate a low degree of cation mixing. More accurate analyses of the powders with six hour scans, followed by Rietveld refinement, revealed that cation mixing was not

present for CPSA, but occurred at a degree of 1.15% for CPGC. This may however be considered a low degree of cation mixing, and is therefore not expected to cause major consequences for lithium diffusion in the CPGC cathodes. Interestingly, the 30 minute XRD scan of precalcined CPGC unexpectedly revealed peaks which indicated that $LiNO_3$ was present in the sample. Figure B.1 in Appendix B shows a comparison of the CPGC powder at different synthesis stages. Due to the high precalcination temperature of 480 °C, all of the lithium nitrate in the sample was expected to have decomposed during the previous step. It is unknown whether the remaining lithium nitrate is a result of insufficient heating of the oven, an unexpected power cut, or too dense packing of the powder in the precalcination crucible. The remaining lithium nitrate was however not expected to have a large impact on the properies of the powder, as it was expected to be completely decomposed after the following calcination step at 800 °C. Indeed, after calcination, the lithium nitrate peaks had all disappeared.

During synthesis, the same parameters were used for both CPGC and CPSA during all stages. This included the molar relationship between precursors, mixing time, temperatures during heat treatment, slurry composition, etc. This way, the impact of known factors separating the two samples was limited to the chemical composition of the precursors used. Due to expected problems with chloride in the chemicals from Glencore, as was also evident in the PMGC sample, the CPGC sample was washed extensively and tested with silver nitrate in order to assure that as little chloride as possible remained. Thus, the amount of chloride remaining in the powder should be close to zero, assuming chloride had not formed stable bonds with the powder. The extensive washing may have caused additional problems, such as washing away the smaller particles, and possibly also washing away nickel or lithium. The increase in cation mixing seen for CPGC could result from the possibility that lithium or nickel had been washed off during the washing procedure. Chloride was washed away after the actual co-precipitation synthesis, so it may already have affected the powders in terms of e.g. growth rate, or morphology. This could likely have contributed to the disparities seen between CPGC and CPSA in crystallite and particle sizes.

SEM images of the powders revealed that the powder crystallites were close to spherical in morphology, and that the crystallites had partly agglomerated together, for both CPGC and CPSA. The agglomerates were not necessarily hard agglomerates, but since only simple sample preparation was performed prior to SEM imaging, this was neither confirmed nor disproven. SEM images seem to indicate that agglomeration especially occurs for CPGC, which was also evident from the particle size calculation from BET surface areas. The BET results showed that CPGC had particle sizes of an order of magnitude larger than CPSA. The difference in particle size for the powders were expected to have an impact on the capacity and stability of the cathodes made from powders with large particle sizes. For example, a high degree of agglomeration can lead to large and uneven particles, which would make cathode packing insufficient, leading to poor contact with the current collector. The amount of binder used in the cathode slurry could also have been excessive for such large particles. Furthermore, the high degree of agglomeration

could lead to poor electrolyte penetration of the cathode. From Rietveld refined X-ray diffractograms, crystallite sizes were identified for each of the powders. In fact, it is the CPGC powder that has the smallest crystallite size, despite having the largest particle size.

Coating CPSA with aluminium phopshate was attempted in order to increase the stability of the coin cells by limiting the dissolution of manganese from the cathode material into the electrolyte. The coated AL-CPSA powder showed largely similar characteristics as CPGC and CPSA in terms of Bragg peaks from XRD, and morphology from SEM. An increase in specific surface area was detected in BET, which may be from the porous nature of the aluminium phosphate crystal structure, which is similar to zeolites. Crystallite size from XRD was slighly larger than for CPSA, however, which was expected, due to the thickness added by the coating onto the CPSA crystallites.

5.2 Electrochemical Characterisation

5.2.1 Electrochemial Impedance

The cathodes made from different precursors showed vastly different electrochemical characteristics. Firstly, the general shape of EIS curves were, for CPGC and CPSA, quite different from what is normally seen in Nyquist plots such as Figure 2.10. They had the characteristic semi-circle shape at high frequencies, but at lower frequencies, where the curve usually has a steep incline, the coin cells instead exhibited erratic behaviour. At first, this was believed to be a result of directly subjecting the coin cells to EIS measurements without allowing them to rest following coin cell assembly, i.e. at 0% state of charge. A suggested solution was to allow the coin cells to charge for a small amount of time, then keep them at constant potential to regain chemical equilibrium, and finally perform the EIS measurements. Due to time-constraints however, the coin cells were immediately subjected to EIS measurements, and then set to galvanostatic charge-discharge cycling. If the aforementioned recommendations had been performed, the coin cells might have had time to let the electrolyte properly soak into the cathode material, which could have resulted in better results at high frequencies. Strangely, however, all the AL-CPSA coin cells indeed exhibited proper behaviour at low frequencies, despite also being immediately subjected to EIS measurements with no rest and/or charge time. Furthermore, it was expected that all coin cells would have the steep incline characteristic after cycling, due to electrolyte having had plenty of time for penetration of the cathode during the charge-discharge cycling. However, after cycling, no coin cells displayed this characteristic, including the AL-CPSA cells which had displayed this prior to cycling. Therefore, the suggested reasoning for why the coin cells initially did not show such behaviour is not necessarily correct.

From the EIS results displayed in Table 4.3, it is apparent that the series resistance of the coin cells are quite similar, independent of the precursors used for the cathode. There was however a large discrepancy in the charge transfer resistance of the coin cells. CPGC had the lowest charge transfer resistance of the three, in

the range of approximately 50-60 Ω. The charge transfer resistance in CPSA was approximately double of what is seen for CPGC, in the range of 90-130 Ω. Finally, AL-CPSA had the highest charge transfer resistance, in the range of 110-200 Ω. The difference in charge transfer resistance between CPGC and CPSA can possibly be explained from the differences in crystallite and particle sizes. CPGC has a smaller crystallite size than CPSA, which makes it more difficult for lithium ions to diffuse into the bulk of each crystallite in CPSA. Furthermore, due to equal amounts of binder used for CPGC and CPSA, the larger crystallite size of CPSA would cause the binder to be thicker for this material. Since the binder is insulating, this may also contribute to the increase of the resistance in the CPSA coin cells. The high charge transfer resistance for AL-CPSA is likely a combined result of the larger crystallite sizes of CPSA, as well as the electrically insulative properties of the aluminium phosphate coating. For the post-cycling EIS results, it is difficult to conclude much, due to the inconsistency of whether the coin cells experienced increased or decreased charge transfer resistance.

5.2.2 Galvanostatic Charge-Discharge Cycling

The first thing that stands out from the galvanostatic charge-discharge cycling results of CPGC and CPSA is how unstable the cycling of CPGC is compared to CPSA. After only few cycles, all CPGC coin cells had massive increases in charge capacities, resulting from apparent inability of the battery tester to increase the cell voltage to the upper limit cut-off voltage. Instead, there appeared to be some form of side reaction occurring in the battery, causing erratic drops in voltage of the cell, which was then continually attempted to be increased again by the tester. Interestingly, the apparent breakdowns did not occur during discharge of the cell, only during charge. This can be clearly seen for cycles 25 and 50 for CPGC2 in Figure 4.9 (a). The disorder in plot (b) of the same from cycle 20 and onward further substantiates this. For CPGC, the apparent breakdown seems to occur very quickly, normally within 10-20 cycles. CPSA cells behave much more normal, compared to CPGC, although the same kind of breakdown behaviour is observed for some cells after many cycles. CPSA1 displayed erratic behaviour after around 70 cycles, while CPSA2 and CPSA4 never reached complete breakdown during their respective 200 and 109 cycles. Both CPSA2 and CPSA4 showed some sort of reaction occurring over a few cycles (30-34 and 60-70, respectively), but both recovered and became stable after their respective anomaly, as is shown in Figure 4.9 (c) and (d) for CPSA2, and in Figure D.1 in Appendix D for CPSA4. CPSA1, however, never recovered from the apparent breakdown occurring at around its 70th cycle. The breakdown of CPSA1 appears similar to all the CPGC coin cells, where the cycling, as discussed, was stable for only a few cycles before breakdown occurred, and where the coin cells never recovered. Due to the stability of the CPSA coin cells, and instability of the CPGC coin cells, CPSA was chosen to be coated with aluminium phosphate, as it had the most promising results. The breakdown of the CPGC cells will be further discussed.

The AL-CPSA coin cells were also largely stable, although there were some anomalies for them, as well. AL-CPSA2, shown in Figure 4.9 (e) and (f) was

initially unstable, but after around 10 cycles, the coin cell stabilised and cycled smoothly, with very little capacity degradation. This can possibly indicate that coating the particles has indeed had an effect on the stability of the coin cell. AL-CPSA1, shown in Figure D.2 (c) and (d) in Appendix D, became unstable after 25 cycles, much like the CPGC cells. AL-CPSA3, shown in Figure D.2 (e) and (f) in Appendix D, also cycled smoothly for all cycles. Due to the desire of testing CPGC and CPSA coin cells prior to choosing which powder to coat with aluminium phosphate, the production of AL-CPSA was delayed until satisfactory results were available for CPGC and CPSA. Therefore, the coin cells were allowed less time to cycle than CPGC and CPSA. The full effect of the coating with aluminium phosphate is therefore difficult to assess completely, due to insufficient data on the capacity degradation of AL-CPSA at cycles beyond number 50.

From the available data, the capacity seemed to degrade slower for AL-CPSA coin cells than it did for CPGC and CPSA cells. The capacity retention from the 2nd to the 20th cycle for CPGC2, CPSA2, and AL-CPSA1, (which were all stable at low cycle numbers), was 86.6%, 92.1 %, and 92.5%, respectively. Such calculations often do not include the first few cycles, due to a commonly seen drop in capacity in these cycles resulting from initial formation of SEI layers, as described in section 2.2.3. Looking closer at CPSA2 and AL-CPSA3, which were stable over more cycles than CPGC2 and AL-CPSA1, the capacity retention from the 3rd to the 50th cycle was 88.3 % and 86.0%, respectively. Although the difference in capacity retention is slight, the impact of it increases with each cycle, which is important to increase the cycle life of the battery.

The actual specific capacity of the coin cells is also an important aspect of the cells' performance. Initial specific capacity for the CPSA coin cells had high disparities, as the capacity for CPSA1 and CPSA4 exceeded 200 mAh/g, while for CPSA2, the initial capacity was around 145 mAh/g. The loading, i.e. the amount of active material on the cathodes were quite similar, and in fact, CPSA1 and CPSA2 were closer to each other than to CPSA4. The difference in capacity is therefore not likely from a difference in the loading. Taking into account the mass of the cathode material should either way neutralise this possibility. Of course, the calculated loading on each cathode is dependent on the assumption that the aluminium foils weigh exactly 13.80g, which was clearly not the case when weighing the individual aluminium foils. The difference can therefore be a result of deviations of the weight of the aluminium foil or possible contaminants that were not taken into account during the calculation of the loading. For CPGC, the specfic capacities were more consistent, at around 170-180 mAh/g. The difference in capacities between CPGC and CPSA coin cells, however, are not likely results of the loading of the cathodes, but more probably results of the difference in specific surface area between the two powders. An increase in SSA, will increase the available space for lithium ions to enter and exit the cathode structure. A higher surface area may then facilitate better storage of the lithium ions, due to increased diffusivity into the bulk of the cathode material, and thereby result in a higher capacity of the cathode. For AL-CPSA, the capacities were found in the range of 140-155 mAh/g initially. This contradicts the theory that higher SSA introduces a higher

capacity, since AL-CPSA had a higher SSA than CPSA, but for AL-CPSA the likely reason is that the additional thickness introduced by the coating may have inhibited the diffusion of lithium ions into the bulk of the active material. The weight of the coating will also slightly reduce the capacity, because the coating is not electrochemically active. This effect in particular was not expected to have a large impact though, considering that only 1% coating was used relative to CPSA powder. As was seen from EIS results, the charge transfer resistance of AL-CPSA was also higher than for the other coin cells, which can contribute to the relatively low capacity.

In the differential capacity plots shown in Figure 4.8, as well as in Figure D.3 in Appendix D, two clearly defined peaks were seen during the charge process (i.e above the x-axis), corresponding to the potentials at which the reduction of nickel and cobalt occurs. The plots were very similar to the results presented by Noh et. al [46], which is shown in Figure 2.9. The decrease in intensity and the adjoined reduction in area underneath the curves with increasing cycle number indicates that the capacity degrades, as was discussed previously. Furthermore, the reduction peaks shift slightly towards the right on the positive side of the x-axis, and slightly to the left on the negative side of the x-axis. This indicates the occurrence of a small polarisation, increasing the resistance, and thus changing the operational voltages of the cell, as discussed in section 2.1.2.

5.2.3 Rate-Capability

During rate-capability measurements, several problems presented themselves. Initially, a mistake in the cycling program caused the cells to cycle 5 times at the lowest C-rate, and following up with only one cycle at each subsequent C-rate. As a result, the CPGC and CPSA coin cells that were subjected to rate-capability tests had already been cycled around 10 times before being subjected to the tests presented in Figure 4.10, as well as Figure D.4 in Appendix D. For AL-CPSA, shown in Figure D.5 in Appendix D, the correct program was used immediately. The cycling program was not the main issue with the rate-capability tests, however. As seen for CPSA6 in Figure 4.10 (a), 3 charge cycles drifted past the 250 mAh/g axis limit. These lines corresponded to the 3rd, 26th and 27th cycle, i.e. three of the cycles with a C-rate of 0.1C. The same was observed for AL-CPSA4 and AL-CPSA5. CPGC5 also behaved erratically, but this is likely related to the similar behaviour of the remaining CPGC cells. The fact that the problems for the rate-capability tests mainly occurred at 0.1 C, could indicate that the battery tester used was not able to supply a steady current at such a low current density. Since all cells experienced the same problems at 0.1 C, problems with the instrument seems even more likely. The upper limit of current for the ports used was 10 mA, but no information was given for the lower limit. The currents used at 0.1C was $\pm$ 0.067 mA. This is well below the upper current limit, but due to an unknown lower limit, it is possible that the instrument was responsible for the poor results at 0.1 C.

Due to the poor cycling at 0.1 C, CPSA6 was subjected to one more rate-capability test with a program starting and ending at 0.2 C. The measurements

for this test are shown in Figure 4.10 (c) and (d), and the results were much more normal than those seen for the 0.1 C tests. Although the first cycle at each new C-rate tends to have a large disparity between charge and discharge capacity, this seems to normalise in the 4 subsequent cycles at the same C-rate. The drop in capacity with increasing C-rate was very clear in Figure 4.10 (d), and the capacity increased once more when the C-rate returned to 0.2 C. By averaging the capacities of the last four cycles at each C-rate, an average capacity was found for each C-rate. This was then divided by the capacity of the initial 0.2 C cycles to find capacities relative to the initial capacity. During charge, these were found to be 89.9%, 83.7%, 75.9% and 97.3% for C-rates of 0.5 C, 1 C, 2 C and 0.2 C, respectively. Likewise, for the discharge capacity, the capacities relative to the initial 0.2 C cycles were found to be 95.0%, 87.6 %, 75.4% and 92.7% for 0.5 C, 1 C, 2 C and 0.2 C, respectively.

5.2.4 CPGC Cycling Performance

There are several possibilities as to why the performance of CPGC was so erratic during cycling. One is that the cathode had partially or temporarily lost contact with the current collector. For example, the cathode could be cracking during cycling, which could cut off contact between some of the active material particles on the cathode and the current collector. However, this would probably lead to poorer capacity during discharge as well, which was not observed to the same extent as it was during charge. Furthermore, it is difficult to find a reason for why such cracking would make the capacity increase past the theoretical limit. Another possibility could be that the current collector had been oxidised. In order to investigate this, CPGC3 and CPSA2 were disassembled after cycling. In the case of oxidation of aluminium to aluminium oxide, discolouration of the current collector would occur. However, no such discolouration could be observed. Furthermore, the cathodes, including the current collectors, were characterised post-mortem in SEM, shown in Figure 4.6, and in Figure A.5 in Appendix A. No distinct differences between cathodes or current collectors prior to and after cycling could be observed.

There is one possible reason for the breakdowns of CPGC coin cells that seem more likely than others. There are numerous side reactions that can occur in a battery, and it is very possible that one or more occurs in CPGC coin cells. Some examples are mentioned in Section 2.2.3, such as decomposition of the LPF in the electrolyte into LiF and PF_5, and further into HF and PF_3O. It is near impossible to tell exactly what reactions are taking place inside the batteries, especially when no clues can be found from the post-mortem characterisation performed. One important aspect of this breakdown phenomenon, however, is that not only does it happen to every single CPGC battery, but also to a CPSA battery. This implies that inherently both battery systems are able to have the same chemical reactions occur in the battery. Thus the difference in precursors should not be a deciding factor of whether these reactions can occur. It may however promote the rate at which these reactions occur, or how quickly they can initiate. This can be indirectly, by e.g. causing the difference seen in particle and crystallite size. However, the CPGC powder had lower SSA than CPSA, which should make the powder less susceptible to chemical reactions, rather than more susceptible. The involvement

could also be direct, i.e. that some species in the CPGC precursors/powder contributes to catalysation of the detrimental reactions that occur. The most likely candidate for this would be chloride ions, that may or may not be present in the CPGC cathodes. It is unknown how exactly chloride ions would affect this, but chloride can likely cause damage to the battery, due to its high reactivity. The electrolyte used in the assembly of all the batteries was one that had been used for a long time by members of the research group, so the properties of the electrolyte may have been compromised due to decomposition of electrolyte components. This may be the reason that the erratic behaviour can occur in all cells, but does not explain why it is more prevalent for CPGC than for the other coin cells.

Chapter 6

Conclusion

In this master's thesis, the goal was to synthesise NMC622 cathodes for lithium-ion batteries using nickel and cobalt chloride solutions from Glencore Nikkelverk AS. To accomplish this, two different synthesis methods were employed. A Pechini method was first attempted, but was not successful in synthesising phase pure NMC622 powder. A co-precipitation synthesis procedure was then succesfully employed to synthesise NMC622 powder, CPGC. The same synthesis procedure was also performed with identical synthesis parameters, to make a reference powder using nickel and cobalt precursors from Sigma-Aldrich, CPSA. Phase purity was established by the use of XRD analysis, and Rietveld refinement was employed to establish that the powders had a low to non-existent degree of cation mixing. SEM was employed to study morphology of the particles, and BET was used to determine the surface area of the particles. The CPGC cathodes were found to be unstable when cycling, which might be a result of side reactions occurring inside the battery. The cause of the side reactions are unknown, however, due to the occurrence of instability in CPGC coin cells, but not in CPSA cells, it was suggested that the chlorine content in the precursors of CPGC may be a contributor to this. The CPSA cathodes also had a higher specific capacity than CPGC, at around 200 mAh/g, compared to 170 mAh/g. CPSA was coated with aluminium phosphate, to limit capacity degradation through manganese dissolution in the electrolyte. The coated powder, AL-CPSA, showed slightly better capacity retention than CPSA, but a lower initial specific capacity, at around 150 mAh/g. In light of the results presented in this thesis, the chemicals provided by Glencore may not be suitable for synthesis of stable, high-capacity lithium-ion batteries unless changes are made to the chemical composition of their precursors.

Chapter 7

Future work

In order to move forward with the research from this thesis, it would be beneficial to determine whether chloride actually was present in the CPGC powders. For this, several methods could be used, e.g. energy dispersive X-ray spectroscopy (EDS) or X-ray fluorescence (XRF). This was not performed in this thesis due to time constraints, and is something that could be considered by Glencore in the future. Furthermore, Glencore could stand to gain a lot by exchanging their chloride solutions for other options, as this would both make the synthesis easier by reducing the amount of requried washing, as well as completely removing any doubt that chloride will have an impact on newly produced batteries. A suitable option could be to dissolve the nickel and cobalt metal in sulphuric acid rather than hydrochloric acid. Sulphuric acid is more commonly used in battery synthesis, and sulphide should be easier than chloride to decompose during heat treatments of the powders. If such changes are successfully applied, Glencore may be able to contribute to the green shift by supplying materials for battery production, whilst reducing waste and increasing their own revenue.

Bibliography

[1] K. Young, C. Wang, L. Y. Wang, and K. Strunz, "Electric vehicle battery technologies," in *Electric Vehicle Integration into Modern Power Networks*, R. Garcia-Valle and J. A. Peças Lopes, Eds., New York, NY: Springer New York, 2013, pp. 15–56, ISBN: 978-1-4614-0133-9 978-1-4614-0134-6. DOI: 10.1007/978-1-4614-0134-6_2. [Online]. Available: http://link.springer.com/10.1007/978-1-4614-0134-6_2 (visited on Oct. 26, 2018).

[2] M. Saiful Islam and C. A. J. Fisher, "Lithium and sodium battery cathode materials: Computational insights into voltage, diffusion and nanostructural properties," *Chemical Society Reviews*, vol. 43, no. 1, pp. 185–204, 2014. DOI: 10.1039/C3CS60199D. [Online]. Available: https://pubs.rsc.org/en/content/articlelanding/2014/cs/c3cs60199d (visited on Oct. 25, 2018).

[3] Recharge - The European Association for Advanced Rechargeable Batteries, "Safety of lithium ion batteries," 2013.

[4] B. Brents. (Feb. 28, 2014). Understanding lithium batteries in portable electronics, Electronic Design, [Online]. Available: https://www.electronicdesign.com/power/understanding-lithium-batteries-portable-electronics (visited on Oct. 26, 2018).

[5] J. B. Goodenough, K. Mizushima, P. C. Jones, and P. J. Wiseman, "LixCoO2 (0¡x¡-1): A new cathode material for batteries of high energy density," *Materials Research Bulletin*, vol. 15, no. 6, pp. 783–789, Jun. 1, 1980, ISSN: 0025-5408. DOI: 10.1016/0025-5408(80)90012-4. [Online]. Available: http://www.sciencedirect.com/science/article/pii/0025540880900124 (visited on May 19, 2019).

[6] M. Armand and J.-M. Tarascon, "Building better batteries," *Nature*, vol. 451, pp. 652–657, Feb. 6, 2008, ISSN: 1476-4687. DOI: 10.1038/451652a. [Online]. Available: https://www.nature.com/articles/451652a (visited on Nov. 12, 2018).

[7] M. Yoshio, R. J. Brodd, and A. Kozawa, Eds., *Lithium-ion batteries: science and technologies*, OCLC: ocn288986473, New York: Springer, 2009, 452 pp., ISBN: 978-0-387-34444-7 978-0-387-34445-4.

[8] N. Yabuuchi and T. Ohzuku, "Novel lithium insertion material of LiCo1/3ni1/3mn1/3o2 for advanced lithium-ion batteries," *Journal of Power Sources*, Selected papers presented at the 11th International Meeting on Lithium Batteries, vol. 119-121, pp. 171–174, Jun. 1, 2003, ISSN: 0378-7753. DOI: 10.1016/S0378-7753(03)00173-3. [Online]. Available: http://www.sciencedirect.com/science/article/pii/S0378775303001733 (visited on Nov. 12, 2018).

[9] C. Julien, A. Mauger, K. Zaghib, and H. Groult, "Comparative issues of cathode materials for li-ion batteries," *Inorganics*, vol. 2, no. 1, pp. 132–154, 2014. [Online]. Available: https://www.researchgate.net/publication/280991937_Comparative_Issues_of_Cathode_Materials_for_Li-Ion_Batteries (visited on Dec. 5, 2018).

[10] N. Nitta, F. Wu, J. T. Lee, and G. Yushin, "Li-ion battery materials: Present and future," *Materials Today*, vol. 18, no. 5, pp. 252–264, Jun. 1, 2015, ISSN: 1369-7021. DOI: 10.1016/j.mattod.2014.10.040. [Online]. Available: http://www.sciencedirect.com/science/article/pii/S1369702114004118 (visited on Nov. 13, 2018).

[11] W. Li, B. Song, and A. Manthiram, "High-voltage positive electrode materials for lithium-ion batteries," *Chemical Society Reviews*, vol. 46, no. 10, pp. 3006–3059, May 22, 2017, ISSN: 1460-4744. DOI: 10.1039/C6CS00875E. [Online]. Available: https://pubs.rsc.org/en/content/articlelanding/2017/cs/c6cs00875e (visited on Sep. 12, 2018).

[12] R. Jung, M. Metzger, F. Maglia, C. Stinner, and H. A. Gasteiger, "Oxygen release and its effect on the cycling stability of LiNixMnyCozO2 (NMC) cathode materials for li-ion batteries," *Journal of The Electrochemical Society*, vol. 164, no. 7, A1361–A1377, Jan. 1, 2017, ISSN: 0013-4651, 1945-7111. DOI: 10.1149/2.0021707jes. [Online]. Available: http://jes.ecsdl.org/content/164/7/A1361 (visited on Oct. 15, 2018).

[13] W. Liu, P. Oh, X. Liu, M.-J. Lee, W. Cho, S. Chae, Y. Kim, and J. Cho, "Nickel-rich layered lithium transition-metal oxide for high-energy lithium-ion batteries," *Angewandte Chemie International Edition*, vol. 54, no. 15, pp. 4440–4457, Mar. 20, 2015, ISSN: 1433-7851. DOI: 10.1002/anie.201409262. [Online]. Available: https://onlinelibrary.wiley.com/doi/full/10.1002/anie.201409262 (visited on Dec. 5, 2018).

[14] Z. Liu, A. Yu, and J. Y. Lee, "Synthesis and characterization of LiNi1-xyCoxMnyO2 as the cathode materials of secondary lithium batteries," *Journal of Power Sources*, vol. 81-82, pp. 416–419, Sep. 1, 1999, ISSN: 0378-7753. DOI: 10.1016/S0378-7753(99)00221-9. [Online]. Available: http://www.sciencedirect.com/science/article/pii/S0378775399002219 (visited on Nov. 13, 2018).

[15] C. D. Rahn and C.-Y. Wang, *Battery Systems Engineering*, 1st ed. John Wiley & Sons, Ltd, 2013. [Online]. Available: http://www.journals.cambridge.org/abstract_S0883769414002346 (visited on Nov. 19, 2018).

[16] Oxford Dictionaries. (2019). Definition of battery in english, [Online]. Available: https://en.oxforddictionaries.com/definition/battery (visited on May 30, 2019).

[17] N. E. Carpenter, *Chemistry of Sustainable Energy*. CRC Press, Mar. 25, 2014, 424 pp., Google-Books-ID: iGTOBQAAQBAJ, ISBN: 978-1-4665-7533-2.

[18] J. B. Goodenough and K.-S. Park, "The li-ion rechargeable battery: A perspective," *Journal of the American Chemical Society*, vol. 135, no. 4, pp. 1167–1176, Jan. 30, 2013, ISSN: 0002-7863, 1520-5126. DOI: 10.1021/ja3091438. [Online]. Available: http://pubs.acs.org/doi/10.1021/ja3091438 (visited on May 30, 2019).

[19] C. Julien, A. Mauger, A. Vijh, and K. Zaghib, *Lithium batteries: science and technology*. Cham Heidelberg New York Dordrecht London: Springer, 2016, 619 pp., OCLC: 929918766, ISBN: 978-3-319-19107-2 978-3-319-19108-9.

[20] C. Liu, Z. G. Neale, and G. Cao, "Understanding electrochemical potentials of cathode materials in rechargeable batteries," *Materials Today*, vol. 19, no. 2, pp. 109–123, Mar. 1, 2016, ISSN: 1369-7021. DOI: 10.1016/j.mattod.2015.10.009. [Online]. Available: http://www.sciencedirect.com/science/article/pii/S1369702115003181 (visited on Nov. 19, 2018).

[21] S. Han, S. Han, and K. Sezaki, "Economic assessment on v2g frequency regulation regarding the battery degradation," in *2012 IEEE PES Innovative Smart Grid Technologies (ISGT)*, Jan. 2012, pp. 1–6. DOI: 10.1109/ISGT.2012.6175717.

[22] V. Aravindan, J. Gnanaraj, Y.-S. Lee, and S. Madhavi, "LiMnPO 4 – a next generation cathode material for lithium-ion batteries," *Journal of Materials Chemistry A*, vol. 1, no. 11, pp. 3518–3539, 2013. DOI: 10.1039/C2TA01393B. [Online]. Available: https://pubs.rsc.org/en/content/articlelanding/2013/ta/c2ta01393b (visited on Dec. 10, 2018).

[23] J. Qian, W. A. Henderson, W. Xu, P. Bhattacharya, M. Engelhard, O. Borodin, and J.-G. Zhang, "High rate and stable cycling of lithium metal anode," *Nature Communications*, vol. 6, p. 6362, Feb. 20, 2015, ISSN: 2041-1723. DOI: 10.1038/ncomms7362. [Online]. Available: https://www.nature.com/articles/ncomms7362 (visited on Dec. 3, 2018).

[24] C. Mao, M. Wood, L. David, S. J. An, Y. Sheng, Z. Du, H. M. Meyer, R. E. Ruther, and D. L. Wood, "Selecting the best graphite for long-life, high-energy li-ion batteries," *Journal of The Electrochemical Society*, vol. 165, no. 9, A1837–A1845, Jan. 1, 2018, ISSN: 0013-4651, 1945-7111. DOI: 10.1149/2.1111809jes. [Online]. Available: http://jes.ecsdl.org/content/165/9/A1837 (visited on Jun. 3, 2019).

[25] E. Peled and S. Menkin, "Review—SEI: Past, present and future," *Journal of The Electrochemical Society*, vol. 164, no. 7, A1703–A1719, Jan. 1, 2017, ISSN: 0013-4651, 1945-7111. DOI: 10.1149/2.1441707jes. [Online]. Available: http://jes.ecsdl.org/content/164/7/A1703 (visited on Jun. 3, 2019).

[26] M. T. McDowell, S. Woo Lee, C. Wang, and Y. Cui, "The effect of metallic coatings and crystallinity on the volume expansion of silicon during electrochemical lithiation/delithiation," *Nano Energy*, vol. 1, no. 3, pp. 401–410, May 1, 2012, ISSN: 2211-2855. DOI: 10.1016/j.nanoen.2012.03.004. [Online]. Available: http://www.sciencedirect.com/science/article/pii/S2211285512000821 (visited on Jun. 3, 2019).

[27] B. Scrosati and J. Garche, "Lithium batteries: Status, prospects and future," *Journal of Power Sources*, vol. 195, no. 9, pp. 2419–2430, May 1, 2010, ISSN: 0378-7753. DOI: 10.1016/j.jpowsour.2009.11.048. [Online]. Available: http://www.sciencedirect.com/science/article/pii/S0378775309020564 (visited on Jun. 3, 2019).

[28] D. Aurbach, Y. Talyosef, B. Markovsky, E. Markevich, E. Zinigrad, L. Asraf, J. S. Gnanaraj, and H.-J. Kim, "Design of electrolyte solutions for li and li-ion batteries: A review," *Electrochimica Acta*, vol. 50, no. 2, pp. 247–254, Nov. 2004, ISSN: 00134686. DOI: 10.1016/j.electacta.2004.01.090. [Online]. Available: https://linkinghub.elsevier.com/retrieve/pii/S0013468604006413 (visited on Jun. 3, 2019).

[29] J. B. Goodenough and Y. Kim, "Challenges for rechargeable li batteries," *Chemistry of Materials*, vol. 22, no. 3, pp. 587–603, Feb. 9, 2010, ISSN: 0897-4756, 1520-5002. DOI: 10.1021/cm901452z. [Online]. Available: http://pubs.acs.org/doi/abs/10.1021/cm901452z (visited on Dec. 4, 2018).

[30] S. S. Zhang, "A review on the separators of liquid electrolyte li-ion batteries," *Journal of Power Sources*, vol. 164, no. 1, pp. 351–364, Jan. 10, 2007, ISSN: 0378-7753. DOI: 10.1016/j.jpowsour.2006.10.065. [Online]. Available: http://www.sciencedirect.com/science/article/pii/S0378775306022452 (visited on Jun. 3, 2019).

[31] C. E. L. Foss, "Thermal stability and electrochemical performance of graphite anodes in li-ion batteries," PhD thesis, NTNU, 2014.

[32] M. S. Whittingham, "Lithium batteries and cathode materials," *Chemical Reviews*, vol. 104, no. 10, pp. 4271–4302, Oct. 1, 2004, ISSN: 0009-2665. DOI: 10.1021/cr020731c. [Online]. Available: https://doi.org/10.1021/cr020731c (visited on Sep. 12, 2018).

[33] H.-m. Cho, M. V. Chen, A. C. Macrae, and Y. S. Meng, *Effect of Surface Modification on Nano-Structured LiNi0.5Mn1.5O4 Spinel Materials*. 2015.

[34] K. I. Ozoemena and S. Chen, *Nanomaterials in Advanced Batteries and Supercapacitors*. Springer, Jul. 18, 2016, 576 pp., ISBN: 978-3-319-26082-2.

[35] G. G. Amatucci, C. N. Schmutz, A. Blyr, C. Sigala, A. S. Gozdz, D. Larcher, and J. M. Tarascon, "Materials' effects on the elevated and room temperature performance of CLiMn2o4 li-ion batteries," *Journal of Power Sources*, vol. 69, no. 1, pp. 11–25, Nov. 1, 1997, ISSN: 0378-7753. DOI: 10.1016/S0378-7753(97)02542-1. [Online]. Available: http://www.sciencedirect.com/science/article/pii/S0378775397025421 (visited on Dec. 5, 2018).

[36] A. Manthiram, A. V. Murugan, A. Sarkar, and T. Muraliganth, "Nanostructured electrode materials for electrochemical energy storage and conversion," *Energy & Environmental Science*, vol. 1, no. 6, pp. 621–638, 2008. DOI: 10.1039/B811802G. [Online]. Available: https://pubs.rsc.org/en/content/articlelanding/2008/ee/b811802g (visited on Dec. 5, 2018).

[37] K. Momma and F. Izumi, "VESTA 3 for three-dimensional visualization of crystal, volumetric and morphology data," *Journal of Applied Crystallography*, vol. 44, pp. 1272–1276, 2011.

[38] A. Merkys, A. Vaitkus, J. Butkus, M. Okulič-Kazarinas, V. Kairys, and S. Gražulis, "COD::CIF::parser: An error-correcting CIF parser for the perl language," *Journal of Applied Crystallography*, vol. 49, no. 1, pp. 292–301, Feb. 1, 2016, ISSN: 1600-5767. DOI: 10.1107/S1600576715022396. [Online]. Available: http://scripts.iucr.org/cgi-bin/paper?po5052 (visited on Dec. 8, 2018).

[39] S. Gražulis, A. Merkys, A. Vaitkus, and M. Okulič-Kazarinas, "Computing stoichiometric molecular composition from crystal structures," *Journal of Applied Crystallography*, vol. 48, no. 1, pp. 85–91, Feb. 1, 2015, ISSN: 1600-5767. DOI: 10.1107/S1600576714025904. [Online]. Available: http://scripts.iucr.org/cgi-bin/paper?kk5188 (visited on Dec. 8, 2018).

[40] S. Gražulis, A. Daškevič, A. Merkys, D. Chateigner, L. Lutterotti, M. Quirós, N. R. Serebryanaya, P. Moeck, R. T. Downs, and A. Le Bail, "Crystallography open database (COD): An open-access collection of crystal structures and platform for world-wide collaboration," *Nucleic Acids Research*, vol. 40, pp. D420–D427, D1 Jan. 1, 2012, ISSN: 0305-1048. DOI: 10.1093/nar/gkr900. [Online]. Available: https://academic.oup.com/nar/article/40/D1/D420/2903497 (visited on Dec. 8, 2018).

[41] S. Gražulis, D. Chateigner, R. T. Downs, A. F. T. Yokochi, M. Quirós, L. Lutterotti, E. Manakova, J. Butkus, P. Moeck, and A. Le Bail, "Crystallography open database – an open-access collection of crystal structures," *Journal of Applied Crystallography*, vol. 42, no. 4, pp. 726–729, Aug. 1, 2009, ISSN: 0021-8898. DOI: 10.1107/S0021889809016690. [Online]. Available: http://scripts.iucr.org/cgi-bin/paper?kk5039 (visited on Dec. 8, 2018).

[42] R. T. Downs and M. Hall-Wallace, "The american mineralogist crystal structure database," *American Mineralogist*, vol. 88, no. 1, pp. 247–250, Jan. 1, 2003, ISSN: 0003-004X. [Online]. Available: https://pubs.geoscienceworld.org/msa/ammin/article-abstract/88/1/247/43886/the-american-mineralogist-crystal-structure (visited on Dec. 8, 2018).

[43] S.-M. Bak, E. Hu, Y. Zhou, X. Yu, S. D. Senanayake, S.-J. Cho, K.-B. Kim, K. Y. Chung, X.-Q. Yang, and K.-W. Nam, "Structural changes and thermal stability of charged LiNixMnyCozO2 cathode materials studied by combined in situ time-resolved XRD and mass spectroscopy," *ACS Applied Materials & Interfaces*, vol. 6, no. 24, pp. 22 594–22 601, Dec. 24, 2014, ISSN: 1944-8244, 1944-8252. DOI: 10.1021/am506712c. [Online]. Available: http://pubs.acs.org/doi/10.1021/am506712c (visited on Oct. 24, 2018).

[44] R. V. Chebiam, A. M. Kannan, F. Prado, and A. Manthiram, "Comparison of the chemical stability of the high energy density cathodes of lithium-ion batteries," *Electrochemistry Communications*, vol. 3, no. 11, pp. 624–627, Nov. 1, 2001, ISSN: 1388-2481. DOI: 10.1016/S1388-2481(01)00232-6. [Online]. Available: http://www.sciencedirect.com/science/article/pii/S1388248101002326 (visited on Dec. 5, 2018).

[45] A. International, "DEMOCRATIC REPUBLIC OF CONGO: "THIS IS WHAT WE DIE FOR": HUMAN RIGHTS ABUSES IN THE DEMOCRATIC REPUBLIC OF THE CONGO POWER THE GLOBAL TRADE IN COBALT," Jan. 19, 2016. [Online]. Available: https://www.amnesty.org/download/Documents/AFR6231832016ENGLISH.PDF (visited on Dec. 19, 2018).

[46] H.-J. Noh, S. Youn, C. S. Yoon, and Y.-K. Sun, "Comparison of the structural and electrochemical properties of layered li[NixCoyMnz]o2 (x = 1/3, 0.5, 0.6, 0.7, 0.8 and 0.85) cathode material for lithium-ion batteries," *Journal of Power Sources*, vol. 233, pp. 121–130, Jul. 1, 2013, ISSN: 0378-7753. DOI: 10.1016/j.jpowsour.2013.01.063. [Online]. Available: http://www.sciencedirect.com/science/article/pii/S0378775313001110 (visited on Dec. 6, 2018).

[47] X. Zhang, W. J. Jiang, A. Mauger, Qilu, F. Gendron, and C. M. Julien, "Minimization of the cation mixing in li1+x(NMC)1-xO2 as cathode material," *Journal of Power Sources*, vol. 195, no. 5, pp. 1292–1301, Mar. 1, 2010, ISSN: 0378-7753. DOI: 10.1016/j.jpowsour.2009.09.029. [Online]. Available: http://www.sciencedirect.com/science/article/pii/S0378775309016231 (visited on Dec. 6, 2018).

[48] J. R. Dahn, "Structure and electrochemistry of lil *,NiOz and a new li2ni02 phase with the ni (OH) 2 structure," p. 11, 1990.

[49] Z.-D. Huang, X.-M. Liu, S.-W. Oh, B. Zhang, P.-C. Ma, and J.-K. Kim, "Microscopically porous, interconnected single crystal LiNi1/3co1/3mn1/3o2 cathode material for lithium ion batteries," *Journal of Materials Chemistry*, vol. 21, no. 29, p. 10 777, 2011, ISSN: 0959-9428, 1364-5501. DOI: 10.1039/c1jm00059d. [Online]. Available: http://xlink.rsc.org/?DOI=c1jm00059d (visited on Dec. 1, 2018).

[50] B. K. Agarwal, *X-Ray Spectroscopy: An Introduction*. Springer, Jun. 29, 2013, 421 pp., Google-Books-ID: fav0CAAAQBAJ, ISBN: 978-3-540-38668-1.

[51] J. I. Goldstein, D. E. Newbury, J. R. Michael, N. W. M. Ritchie, J. H. J. Scott, and D. C. Joy, *Scanning Electron Microscopy and X-Ray Microanalysis*. Springer, Nov. 17, 2017, 554 pp., Google-Books-ID: D0I_DwAAQBAJ, ISBN: 978-1-4939-6676-9.

[52] S. Lowell, J. E. Shields, M. A. Thomas, and M. Thommes, *Characterization of Porous Solids and Powders: Surface Area, Pore Size and Density*. Springer Science & Business Media, Apr. 24, 2006, 370 pp., Google-Books-ID: N0r6oZ1QjMsC, ISBN: 978-1-4020-2302-6.

[53] F. Scholz, Ed., *Electroanalytical Methods: Guide to Experiments and Applications*, 2nd ed., Berlin Heidelberg: Springer-Verlag, 2010, ISBN: 978-3-642-02914-1. [Online]. Available: https://www.springer.com/gp/book/9783642029141 (visited on May 27, 2019).

[54] R. J. Brodd, *Batteries for Sustainability: Selected Entries from the Encyclopedia of Sustainability Science and Technology — Request PDF*. Springer, 2013. [Online]. Available: https://www.researchgate.net/publication/321618491_Batteries_for_Sustainability_Selected_Entries_from_the_Encyclopedia_of_Sustainability_Science_and_Technology (visited on Dec. 19, 2018).

[55] C.-y. Hu, J. Guo, Y. Du, H.-h. Xu, and Y.-h. He, "Effects of synthesis conditions on layered li[ni1/3co1/3mn1/3]o2 positive-electrode via hydroxide coprecipitation method for lithium-ion batteries," *Transactions of Nonferrous Metals Society of China*, vol. 21, no. 1, pp. 114–120, Jan. 1, 2011, ISSN: 1003-6326. DOI: 10.1016/S1003-6326(11)60686-9. [Online]. Available: http://www.sciencedirect.com/science/article/pii/S1003632611606869 (visited on Feb. 22, 2019).

[56] J. Schindelin, I. Arganda-Carreras, E. Frise, V. Kaynig, M. Longair, T. Pietzsch, S. Preibisch, C. Rueden, S. Saalfeld, B. Schmid, J.-Y. Tinevez, D. J. White, V. Hartenstein, K. Eliceiri, P. Tomancak, and A. Cardona, "Fiji: An open-source platform for biological-image analysis," *Nature Methods*, vol. 9, no. 7, pp. 676–682, Jul. 2012, ISSN: 1548-7105. DOI: 10.1038/nmeth.2019. [Online]. Available: https://www.nature.com/articles/nmeth.2019 (visited on Dec. 8, 2018).

[57] C. A. Schneider, W. S. Rasband, and K. W. Eliceiri, "NIH image to ImageJ: 25 years of image analysis," *Nature Methods*, vol. 9, no. 7, pp. 671–675, Jul. 2012, ISSN: 1548-7091, 1548-7105. DOI: 10.1038/nmeth.2089. [Online]. Available: http://www.nature.com/articles/nmeth.2089 (visited on Dec. 8, 2018).

Appendix A

Scanning Electron Microscopy

This appendix presents results from SEM which are not included in Chapter 4 of this thesis.

A.1 Scanning Electron Microscopy for Powder Characterisation

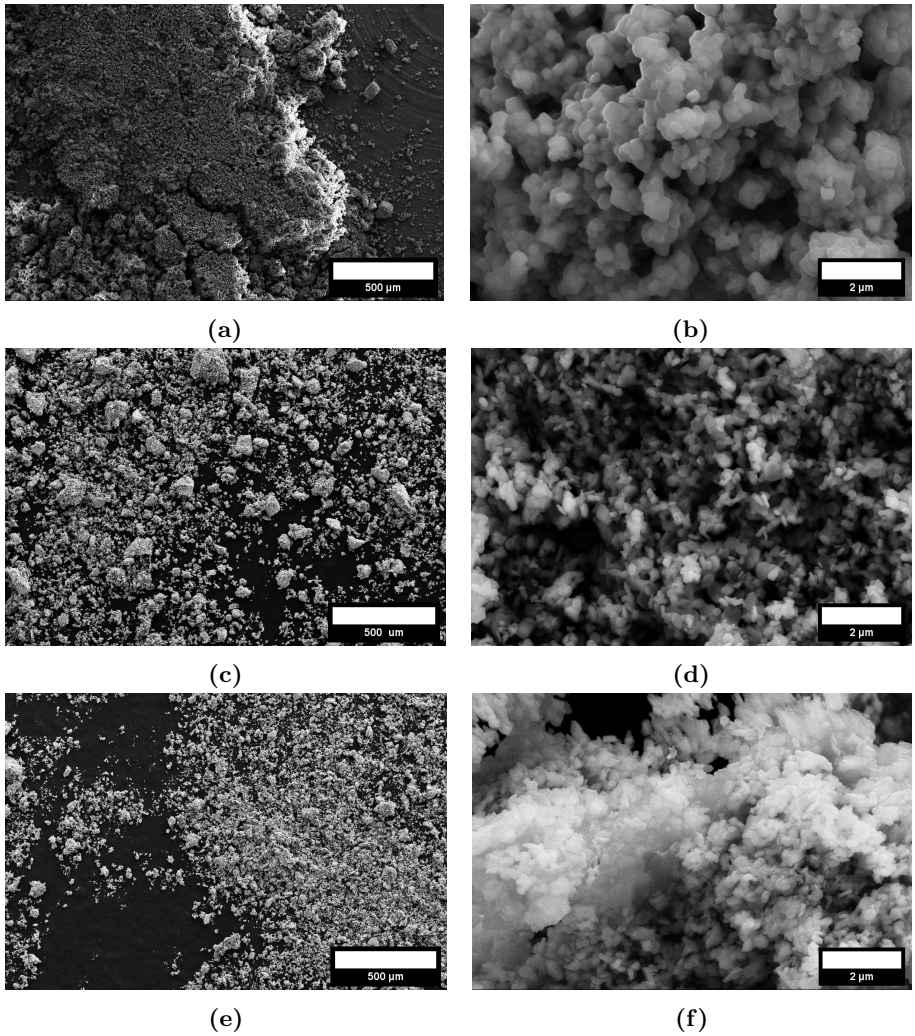

Figure A.1: SEM images of calcined CPGC (a) & (b), calcined CPSA (c) & (d), and AL-CPSA (e) & (f) powders.

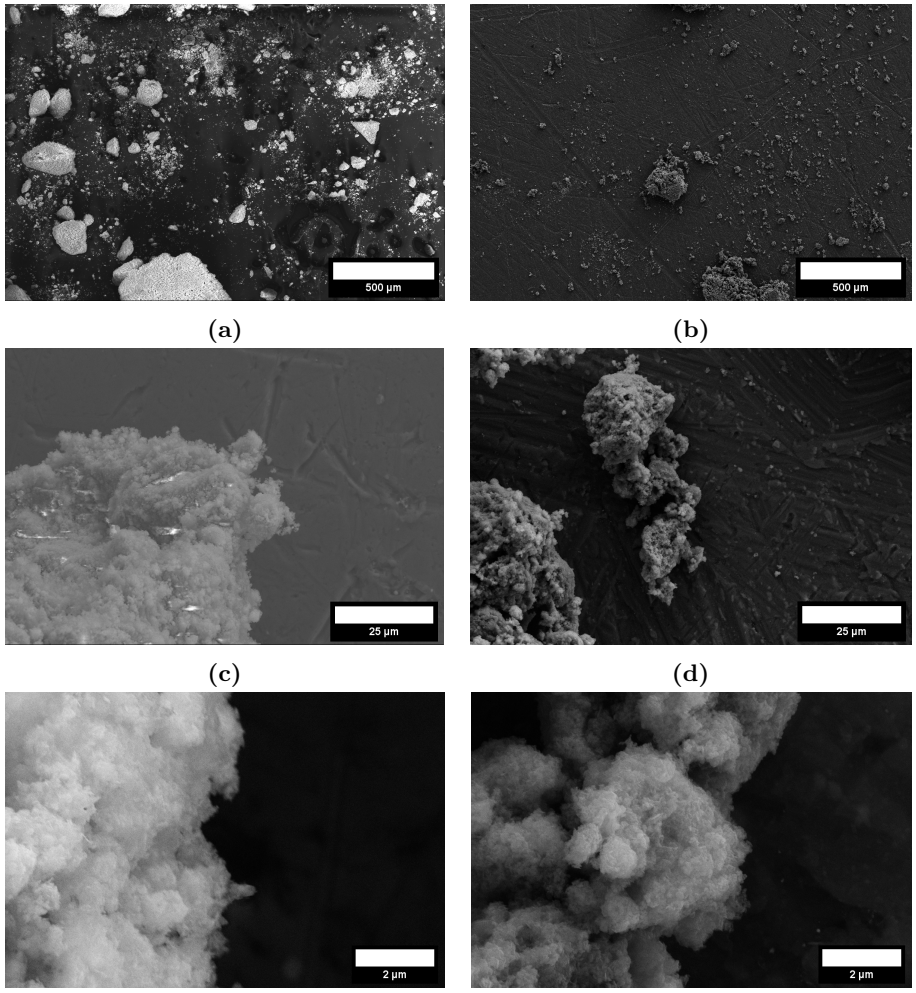

Figure A.2: SEM images of uncalcined CPGC (a), (c) & (e), and precalcined CPGC (b), (d) & (f) powders.

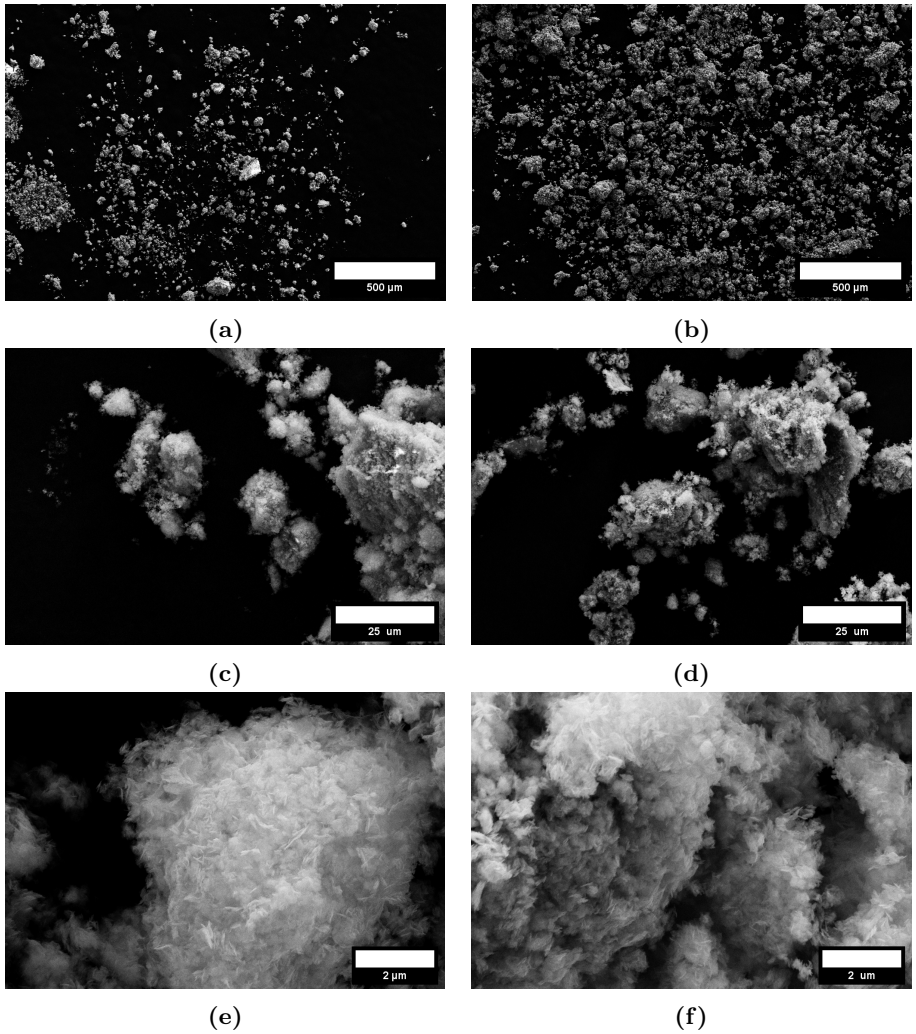

Figure A.3: SEM images of uncalcined CPSA (a), (c) & (e), and precalcined CPSA (b), (d) & (f) powders.

A.2 Scanning Electron Microscopy for Cathode Characterisation

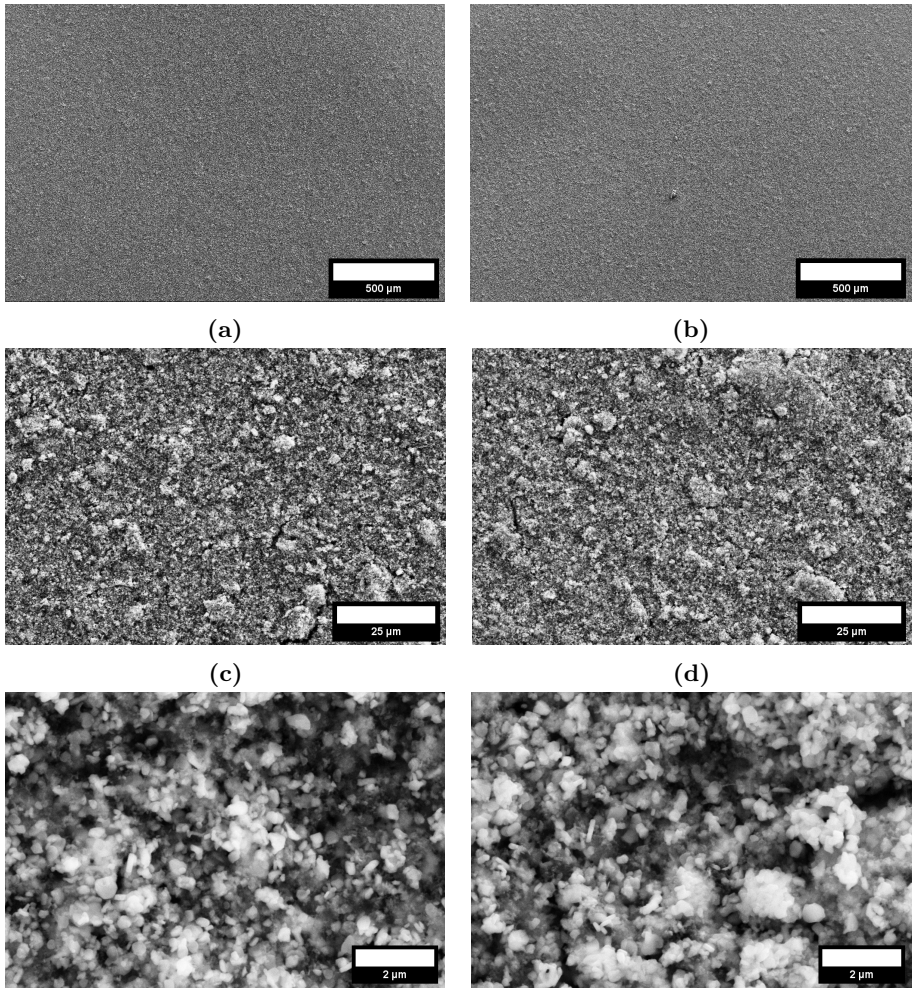

Figure A.4: SEM images of a CPSA cathode pre cycling (a), (c) & (e) and a CPSA cathode post cycling (b), (d) & (f).

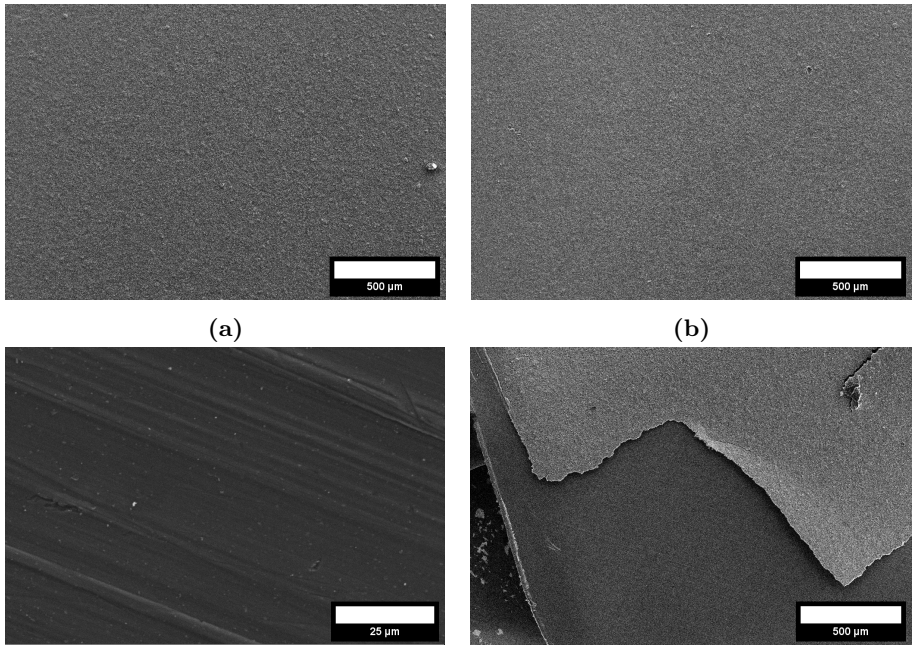

Figure A.5: SEM images of a CPGC cathode pre cycling (a) and post cycling (b). Image (c) shows shows the aluminium current collector of a CPSA cathode post cycling, and image (d) shows an overview of the cathode material exfoliated from the current collector after cell disassembly.

Appendix B

X-Ray Diffraction

This appendix presents results from XRD which are not included in Chapter 4 of this thesis.

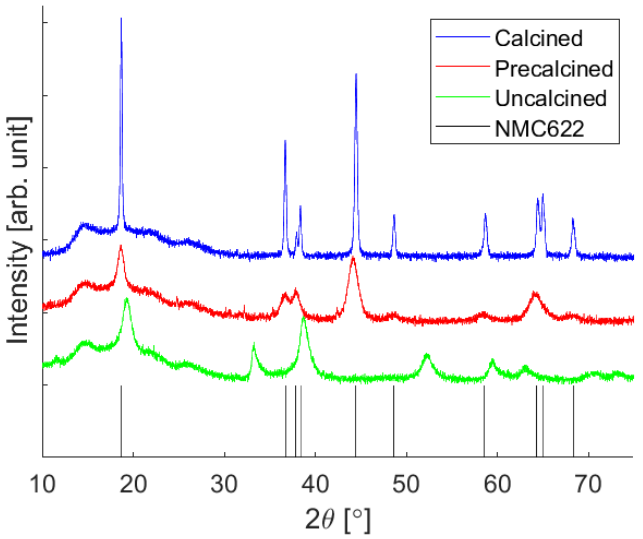

Figure B.1: X-Ray Diffractograms of 30 minute scans of CPSA at different stages. Uncalcined powder is shown in green, precalcined powder is showed in red, and calcined powder is shown in blue. The black lines indicate reference peaks for NMC622.

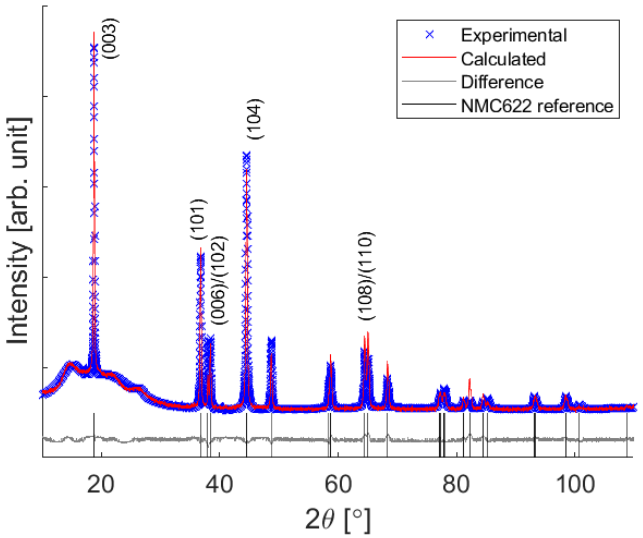

Figure B.2: Rietveld refined X-ray diffractogram of CPSA. Measured values are shown in blue, calculated values are shown in red, and the difference between measured and calculated is shown in grey. The black lines indicate reference peaks for NMC622. The relevant Bragg peaks have been indicated by including the hkl values of the crystal planes they correspond to.

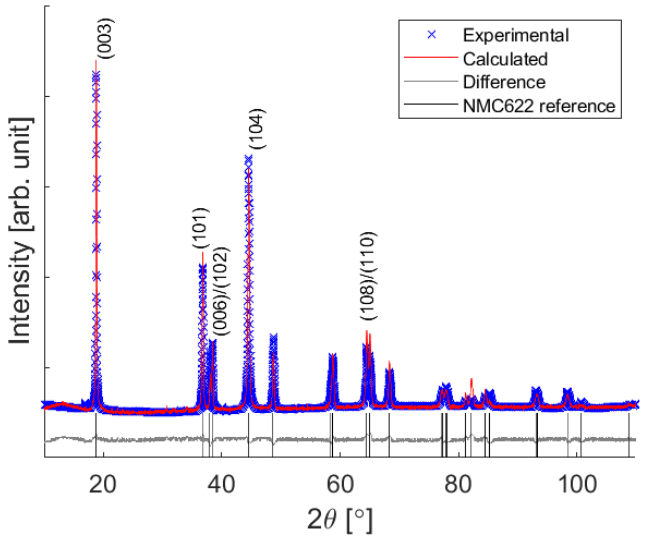

Figure B.3: Rietveld refined X-ray diffractogram of AL-CPSA. Measured values are shown in blue, calculated values are shown in red, and the difference between measured and calculated is shown in grey. The black lines indicate reference peaks for NMC622. The relevant Bragg peaks have been indicated by including the hkl values of the crystal planes they correspond to.

Appendix C

Electrochemical Impedance Spectroscopy

This appendix presents results from electrochemical impedance spectroscopy which are not included in Chapter 4 of this thesis.

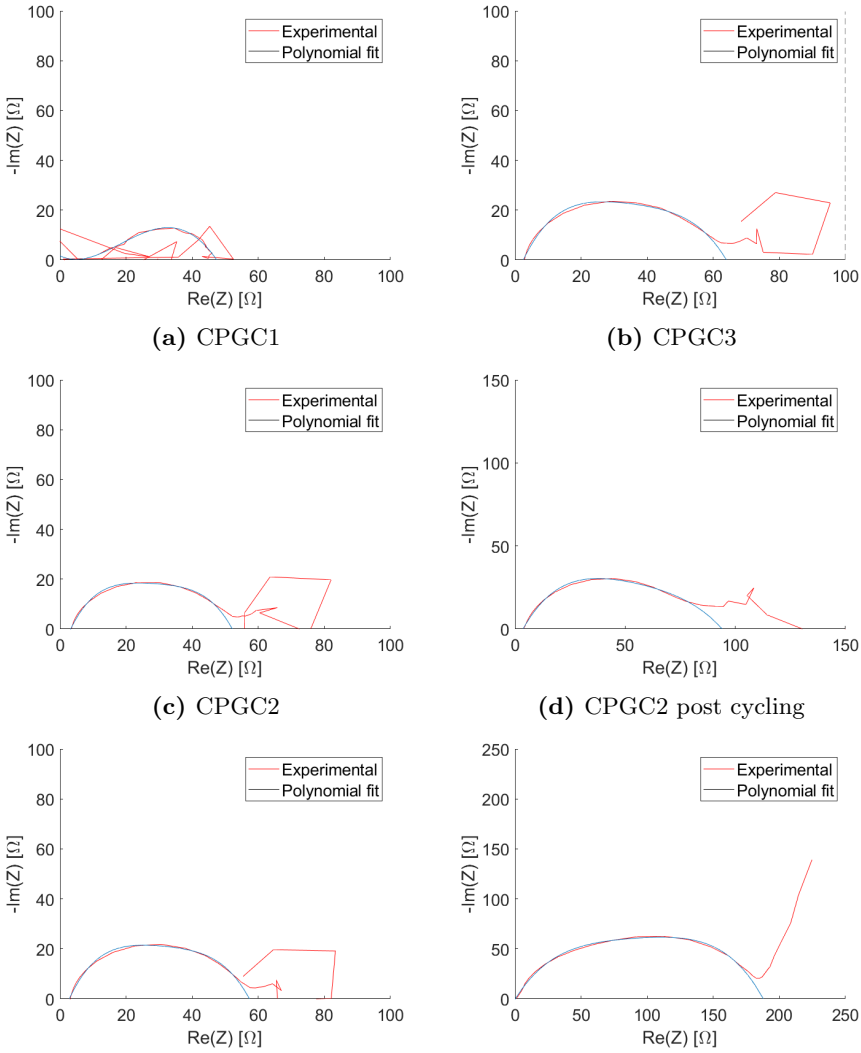

(a) CPGC1 **(b)** CPGC3

(c) CPGC2 **(d)** CPGC2 post cycling

(e) CPGC4 **(f)** AL-CPSA2

Figure C.1: Results from electrochemical impedance spectroscopy for CPGC1, CPGC3, CPGC2, CPGC2 post cycling, CPGC4 and AL-CPSA2.

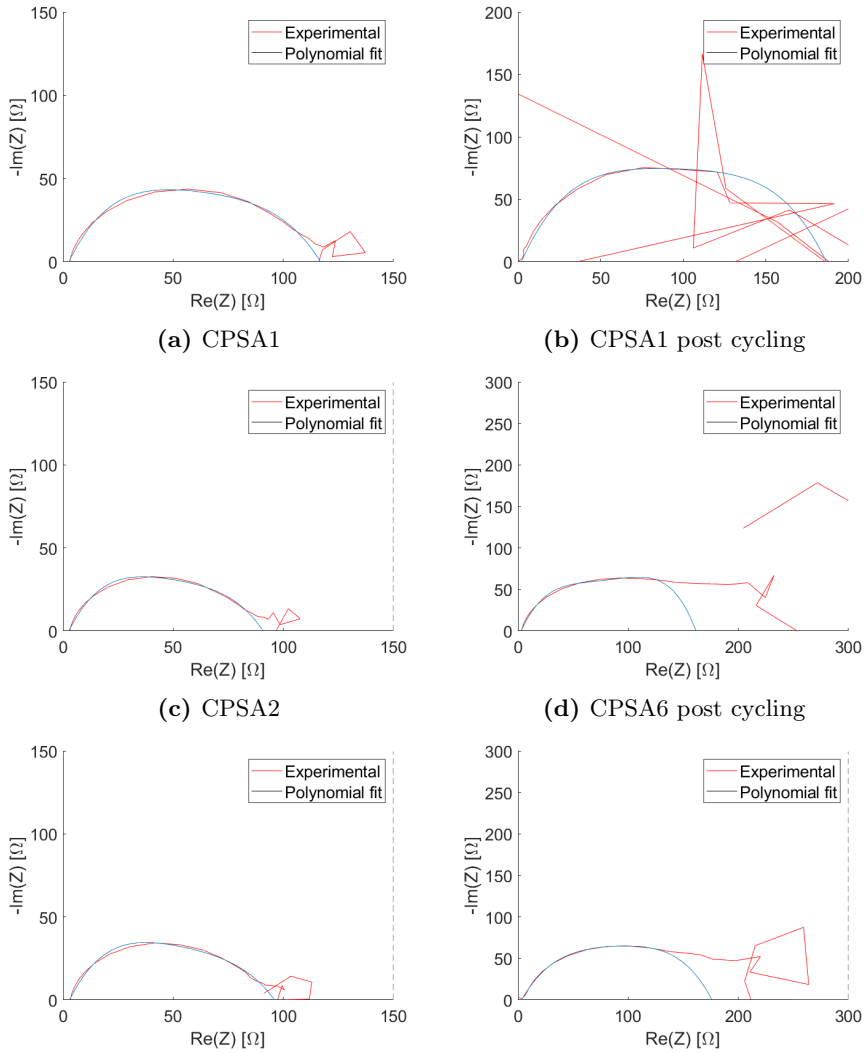

(a) CPSA1

(b) CPSA1 post cycling

(c) CPSA2

(d) CPSA6 post cycling

(e) CPSA4

(f) CPSA4 post cycling

Figure C.2: Results from electrochemical impedance spectroscopy for CPSA1, CPSA1 post cycling, CPSA2, CPSA6, CPSA4 and CPSA4 post cycling.

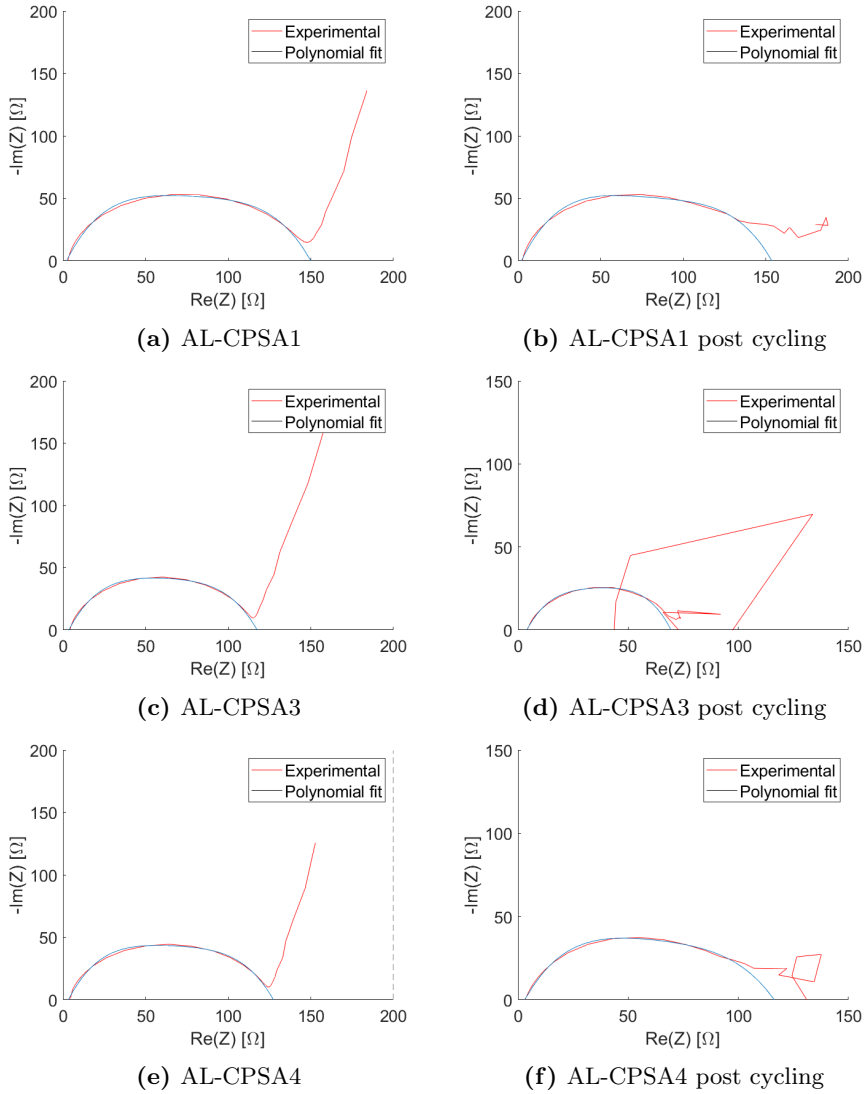

(a) AL-CPSA1

(b) AL-CPSA1 post cycling

(c) AL-CPSA3

(d) AL-CPSA3 post cycling

(e) AL-CPSA4

(f) AL-CPSA4 post cycling

Figure C.3: Results from electrochemical impedance spectroscopy for AL-CPSA1, AL-CPSA1 post cycling, AL-CPSA3, AL-CPSA3 post cycling, AL-CPSA4 and AL-CPSA4 post cycling.

Appendix D

Galvanostatic Cycling Results

This appendix presents results from galvanostatic charge-discharge cycling which are not included in Chapter 4 of this thesis.

D.1 Galvanostatic Charge-Discharge Cycling

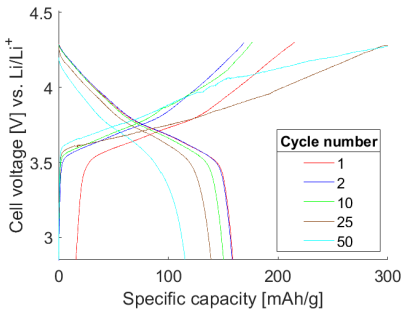

(a) CPGC3

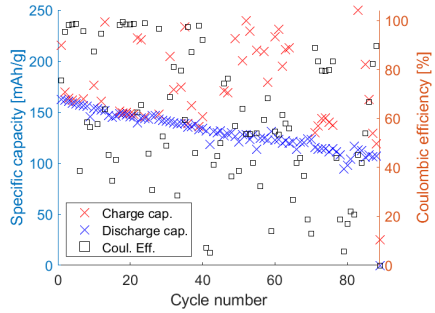

(b) CPGC3

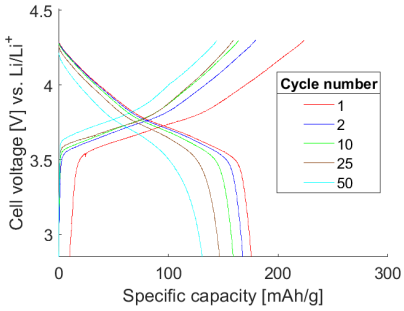

(c) CPGC4

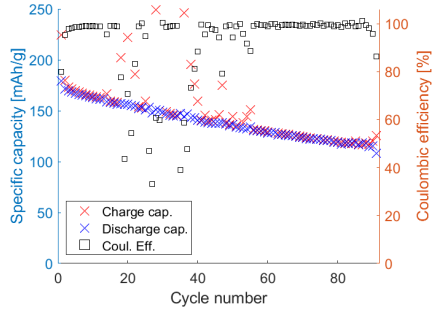

(d) CPGC4

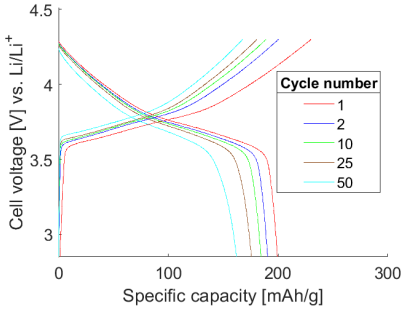

(e) CPSA1

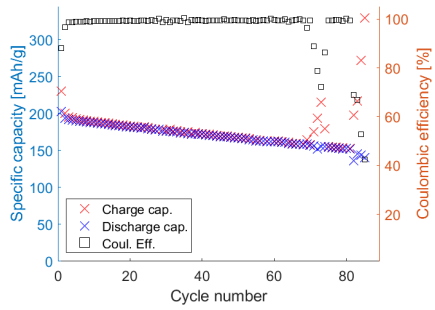

(f) CPSA1

Figure D.1: Figures on the left show cycling data as plots of voltage as a function of specific capacity for coin cells CPGC3 (a), CPGC4 (c) and CPSA1 (e). Figures on the right show specific charge and discharge capacity as well as Coulombic efficiency as a function of cycle number for CPGC3 (b), CPGC4 (d) and CPSA1 (f).

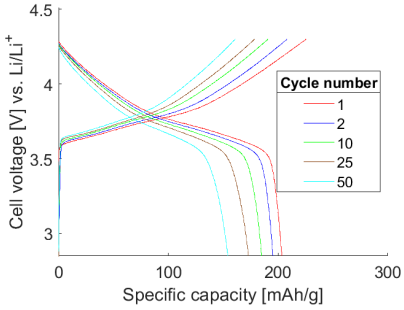

(a) CPSA4

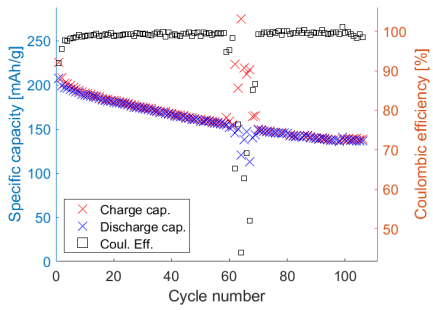

(b) CPSA4

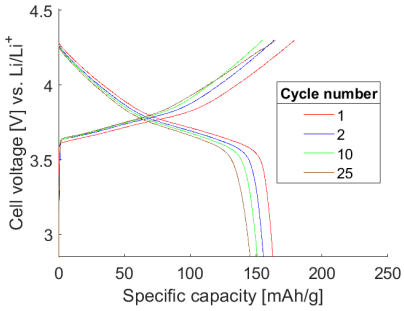

(c) AL-CPSA1

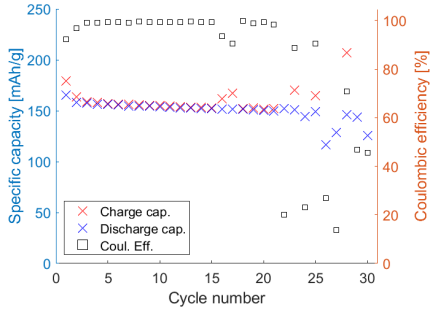

(d) AL-CPSA1

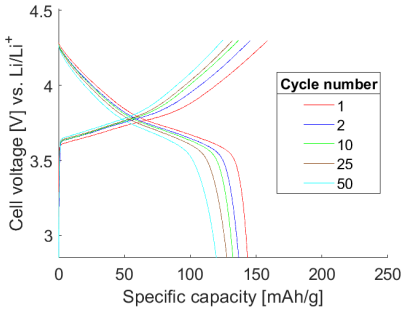

(e) AL-CPSA3

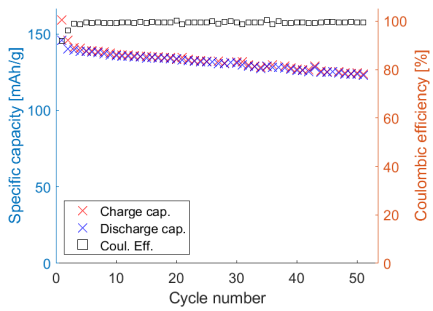

(f) AL-CPSA3

Figure D.2: Figures on the left show cycling data as plots of voltage as a function of specific capacity for coin cells CPSA4 (a), AL-CPSA1 (c) and AL-CPSA3 (e). Figures on the right show specific charge and discharge capacity as well as Coulombic efficiency as a function of cycle number for CPSA4 (b), AL-CPSA1 (d) and AL-CPSA3 (f).

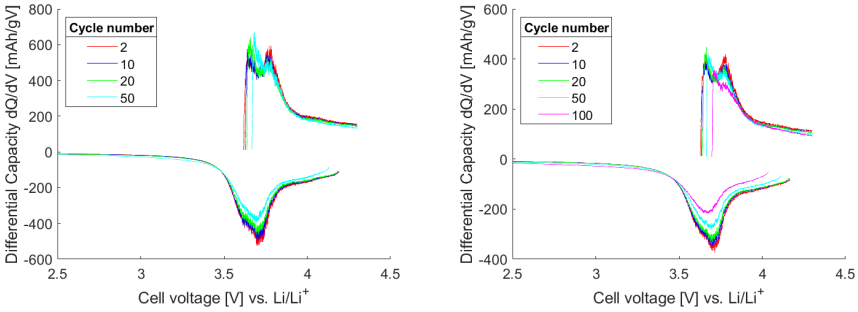

(a) CPSA1

(b) CPSA2

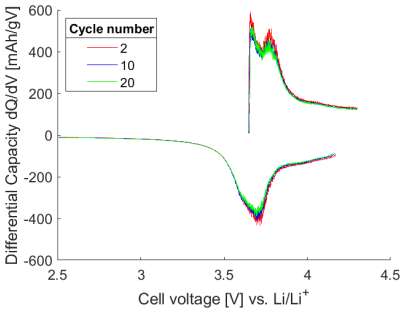

(c) AL-CPSA1

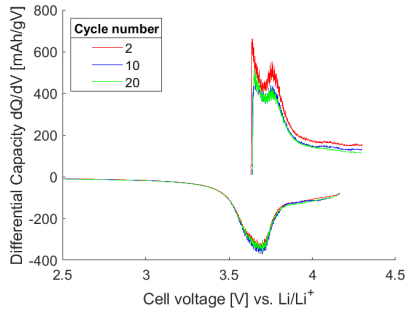

(d) AL-CPSA2

Figure D.3: Differential capacity plots as a function of cell voltage vs. Li/Li^+ for CPSA1 (a), CPSA2 (b), AL-CPSA1 (c) and AL-CPSA2 (d).

D.2 Rate Capability Cycling

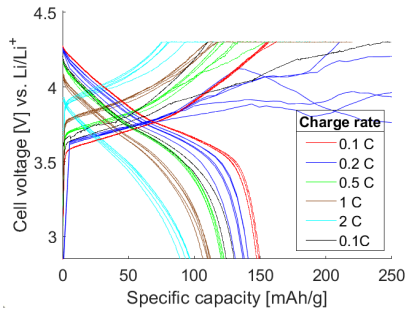

(a) CPGC5

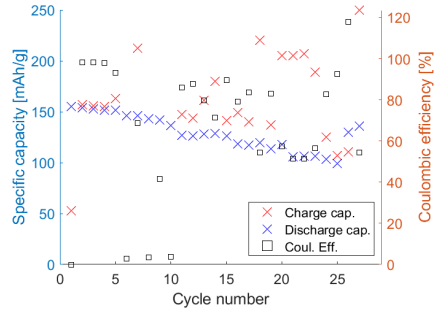

(b) CPGC5

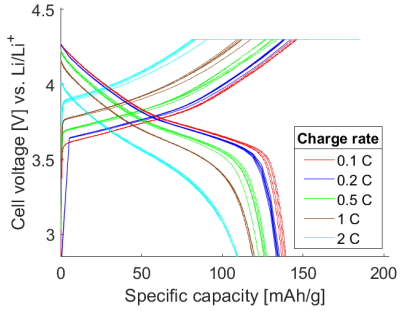

(c) CPSA5

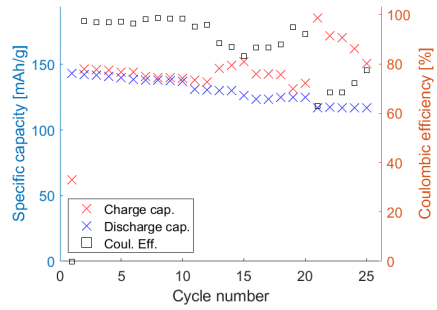

(d) CPSA5

Figure D.4: Plots (a) and (b) shows rate-capability cycling data for CPGC5. Plots (c) and (d) shows rate-capability cycling for CPSA5. Left hand side plots show cell voltages as a function of specific capacities over a range of cycles charged and discharged at different C-rates. Right hand side plots show specific charge and discharge capacity as well as Coulombic efficiency as a function of cycle number at different C-rates.

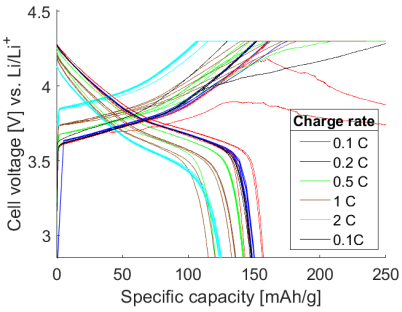

(a) AL-CPSA4

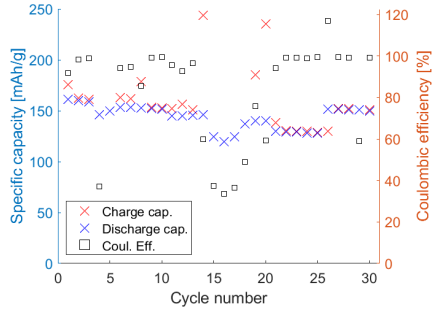

(b) AL-CPSA4

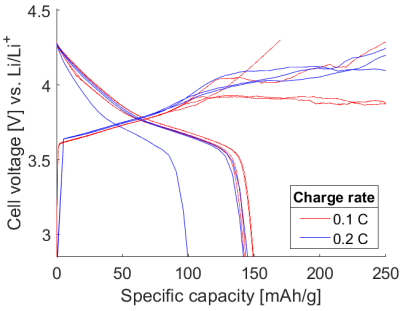

(c) AL-CPSA5

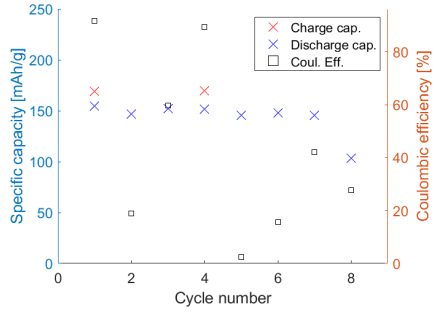

(d) AL-CPSA5

Figure D.5: Plots (a) and (b) shows rate-capability cycling data for AL-CPSA4. Plots (c) and (d) shows rate-capability cycling for AL-CPSA5. Left hand side plots show cell voltages as a function of specific capacities over a range of cycles charged and discharged at different C-rates. Right hand side plots show specific charge and discharge capacity as well as Coulombic efficiency as a function of cycle number at different C-rates.

Appendix E

Brunauer-Emmet-Teller Surface Area Analysis

In this appendix, the produced reports from BET analysis of CPGC, CPSA and AL-CPSA powders are included.

Sample: CPGC
Operator:
Submitter:
File: C:\...\STEINA~1\CPGC.SMP

Started: 10.05.2019 13:50:18
Completed: 10.05.2019 17:25:10
Report Time: 10.05.2019 18:01:17
Warm Free Space: 11.7008 cm³ Measured
Equilibration Interval: 5 s
Sample Density: 1.000 g/cm³

Analysis Adsorptive: N2
Analysis Bath Temp.: 77.300 K
Sample Mass: 1.1288 g
Cold Free Space: 34.2284 cm³ Measured
Low Pressure Dose: None
Automatic Degas: No

Isotherm Tabular Report

Relative Pressure (p/p°)	Absolute Pressure (mmHg)	Quantity Adsorbed (cm³/g STP)	Elapsed Time (h:min)	Saturation Pressure (mmHg)
			00:50	760.45886
0.009534672	7.25073	0.0625	00:55	
0.033489233	25.46718	0.0777	00:56	
0.057229960	43.52103	0.0842	00:57	
0.059971384	45.60577	0.0836	00:59	
0.091684178	69.72205	0.0901	01:00	
0.099930380	75.99294	0.0909	01:01	
0.112392890	85.47017	0.0923	01:03	
0.119876973	91.16151	0.0927	01:04	
0.139818089	106.32590	0.0955	01:05	
0.159797589	121.51949	0.0982	01:06	
0.174837038	132.95638	0.0999	01:08	
0.179930599	136.82982	0.0994	01:09	
0.199734649	151.88998	0.1018	01:10	
0.236952217	180.19241	0.1068	01:11	
0.249787569	189.95317	0.1084	01:13	
0.299226393	227.54936	0.1144	01:14	
0.349087409	265.46661	0.1210	01:15	
0.398893587	303.34216	0.1280	01:16	
0.448754623	341.25943	0.1353	01:18	
0.498615619	379.17667	0.1430	01:19	
0.548454704	417.07724	0.1512	01:20	
0.598310242	454.99033	0.1600	01:21	
0.648165780	492.90341	0.1697	01:23	
0.698004825	530.80396	0.1813	01:24	
0.738237957	561.39960	0.1929	01:25	
0.768607500	584.49438	0.2040	01:27	
0.798615145	607.31396	0.2156	01:28	
0.818912580	622.74933	0.2272	01:29	
0.839056635	638.06805	0.2388	01:30	
0.858860625	653.12817	0.2547	01:32	
0.874218078	664.80688	0.2697	01:33	
0.889219172	676.21460	0.2857	01:34	
0.904094095	687.52637	0.3069	01:35	
0.914451210	695.40253	0.3254	01:37	
0.924397148	702.96600	0.3478	01:38	
0.932544598	709.16180	0.3700	01:39	
0.939502340	714.45288	0.3949	01:40	
0.946608164	719.85657	0.4237	01:42	
0.952606386	724.41797	0.4527	01:44	
0.958346891	728.78339	0.4969	01:45	
0.963742032	732.88617	0.5446	01:46	
0.967645845	735.85486	0.5874	01:48	
0.970688779	738.16888	0.6304	01:49	
0.973753704	740.49963	0.6810	01:50	

Sample: CPGC
Operator:
Submitter:
File: C:\...\STEINA~1\CPGC.SMP

Started: 10.05.2019 13:50:18
Completed: 10.05.2019 17:25:10
Report Time: 10.05.2019 18:01:17
Warm Free Space: 11.7008 cm³ Measured
Equilibration Interval: 5 s
Sample Density: 1.000 g/cm³

Analysis Adsorptive: N2
Analysis Bath Temp.: 77.300 K
Sample Mass: 1.1288 g
Cold Free Space: 34.2284 cm³ Measured
Low Pressure Dose: None
Automatic Degas: No

Isotherm Tabular Report

Relative Pressure (p/p°)	Absolute Pressure (mmHg)	Quantity Adsorbed (cm³/g STP)	Elapsed Time (h:min)	Saturation Pressure (mmHg)
0.976555453	742.63025	0.7433	01:51	
0.979625836	744.96515	0.8305	01:53	
0.981583240	746.45367	0.9124	01:54	
0.983869554	748.19232	1.0207	01:55	
0.985536333	749.45984	1.1287	01:57	
0.987482742	750.94000	1.2851	01:58	
0.988299718	751.56128	1.4418	02:00	
0.989297603	752.32013	1.6770	02:01	
0.982202775	746.92480	1.1731	02:03	
0.972936728	739.87836	0.8025	02:05	
0.958692334	729.04608	0.5536	02:07	
0.937994558	713.30627	0.4124	02:08	
0.916309893	696.81598	0.3374	02:10	
0.897350249	682.39795	0.2966	02:11	
0.872436204	663.45184	0.2617	02:12	
0.842532737	640.71149	0.2327	02:14	
0.821719867	624.88416	0.2158	02:15	
0.801575812	609.56543	0.2022	02:16	
0.781470281	594.27600	0.1910	02:17	
0.751956080	571.83167	0.1763	02:19	
0.721893616	548.97040	0.1634	02:20	
0.682170381	518.76251	0.1508	02:21	
0.632468382	480.96619	0.1372	02:23	
0.582278397	442.79877	0.1251	02:24	
0.532132274	404.66470	0.1128	02:25	
0.482013560	366.55148	0.0995	02:26	
0.431872934	328.42160	0.0855	02:28	
0.381650042	290.22916	0.0751	02:29	
0.331525850	252.11177	0.0647	02:31	
0.281357795	213.96103	0.0552	02:32	
0.231282964	175.88118	0.0450	02:33	
0.181301316	137.87219	0.0342	02:34	
0.122678713	93.29211	0.0203	02:36	

Sample: CPGC
Operator:
Submitter:
File: C:\...\STEINA~1\CPGC.SMP

Started:	10.05.2019 13:50:18	Analysis Adsorptive:	N2
Completed:	10.05.2019 17:25:10	Analysis Bath Temp.:	77.300 K
Report Time:	10.05.2019 18:01:17	Sample Mass:	1.1288 g
Warm Free Space:	11.7008 cm³ Measured	Cold Free Space:	34.2284 cm³ Measured
Equilibration Interval:	5 s	Low Pressure Dose:	None
Sample Density:	1.000 g/cm³	Automatic Degas:	No

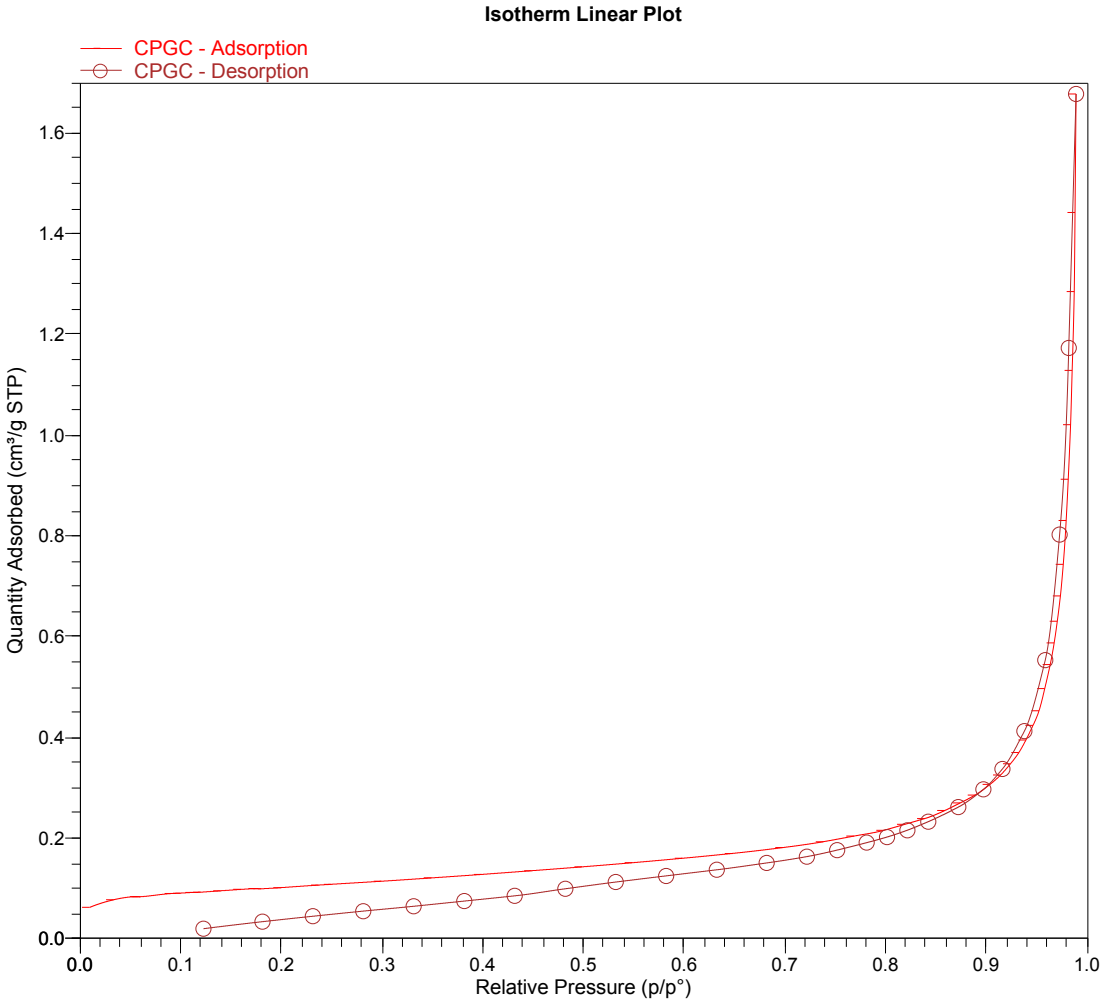

Sample: CPGC
Operator:
Submitter:
File: C:\...\STEINA~1\CPGC.SMP

Started:	10.05.2019 13:50:18	Analysis Adsorptive:	N2
Completed:	10.05.2019 17:25:10	Analysis Bath Temp.:	77.300 K
Report Time:	10.05.2019 18:01:17	Sample Mass:	1.1288 g
Warm Free Space:	11.7008 cm³ Measured	Cold Free Space:	34.2284 cm³ Measured
Equilibration Interval:	5 s	Low Pressure Dose:	None
Sample Density:	1.000 g/cm³	Automatic Degas:	No

Isotherm Log Plot

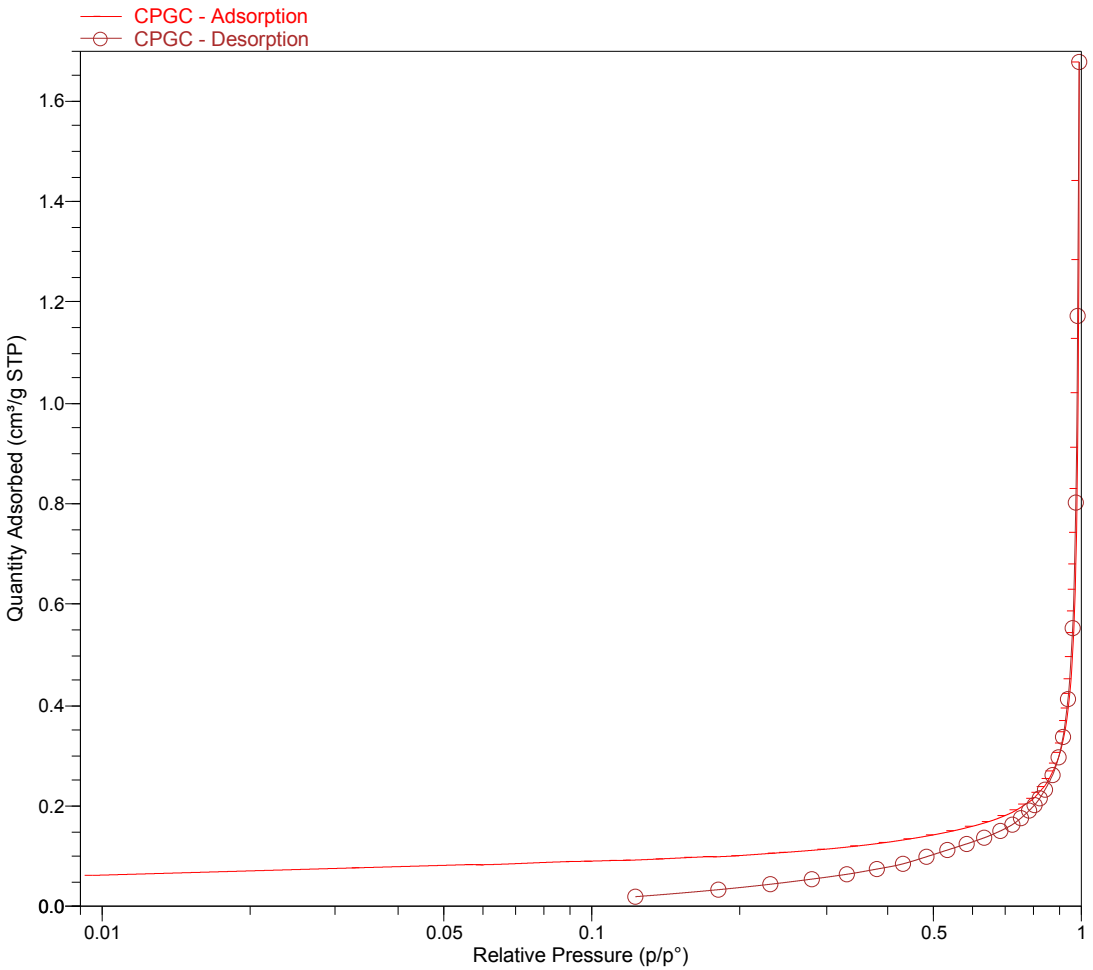

Sample: CPGC
Operator:
Submitter:
File: C:\...\STEINA~1\CPGC.SMP

Started: 10.05.2019 13:50:18
Completed: 10.05.2019 17:25:10
Report Time: 10.05.2019 18:01:17
Warm Free Space: 11.7008 cm³ Measured
Equilibration Interval: 5 s
Sample Density: 1.000 g/cm³

Analysis Adsorptive: N2
Analysis Bath Temp.: 77.300 K
Sample Mass: 1.1288 g
Cold Free Space: 34.2284 cm³ Measured
Low Pressure Dose: None
Automatic Degas: No

BET Surface Area Report

BET Surface Area: 0.3527 ± 0.0032 m²/g
Slope: 12.350462 ± 0.109885 g/cm³ STP
Y-Intercept: -0.007649 ± 0.018517 g/cm³ STP
C: -1613.568745
Qm: 0.0810 cm³/g STP
Correlation Coefficient: 0.9996835
Molecular Cross-Sectional Area: 0.1620 nm²

Relative Pressure (p/p°)	Quantity Adsorbed (cm³/g STP)	1/[Q(p°/p - 1)]
0.057229960	0.0842	0.721321
0.059971384	0.0836	0.762688
0.091684178	0.0901	1.120147
0.112392890	0.0923	1.371633
0.119876973	0.0927	1.469758
0.159797589	0.0982	1.936431
0.174837038	0.0999	2.121188
0.199734649	0.1018	2.452854
0.236952217	0.1068	2.906394
0.299226393	0.1144	3.731326

Sample: CPGC
Operator:
Submitter:
File: C:\...\STEINA~1\CPGC.SMP

Started:	10.05.2019 13:50:18	Analysis Adsorptive:	N2
Completed:	10.05.2019 17:25:10	Analysis Bath Temp.:	77.300 K
Report Time:	10.05.2019 18:01:17	Sample Mass:	1.1288 g
Warm Free Space:	11.7008 cm³ Measured	Cold Free Space:	34.2284 cm³ Measured
Equilibration Interval:	5 s	Low Pressure Dose:	None
Sample Density:	1.000 g/cm³	Automatic Degas:	No

BET Surface Area Plot

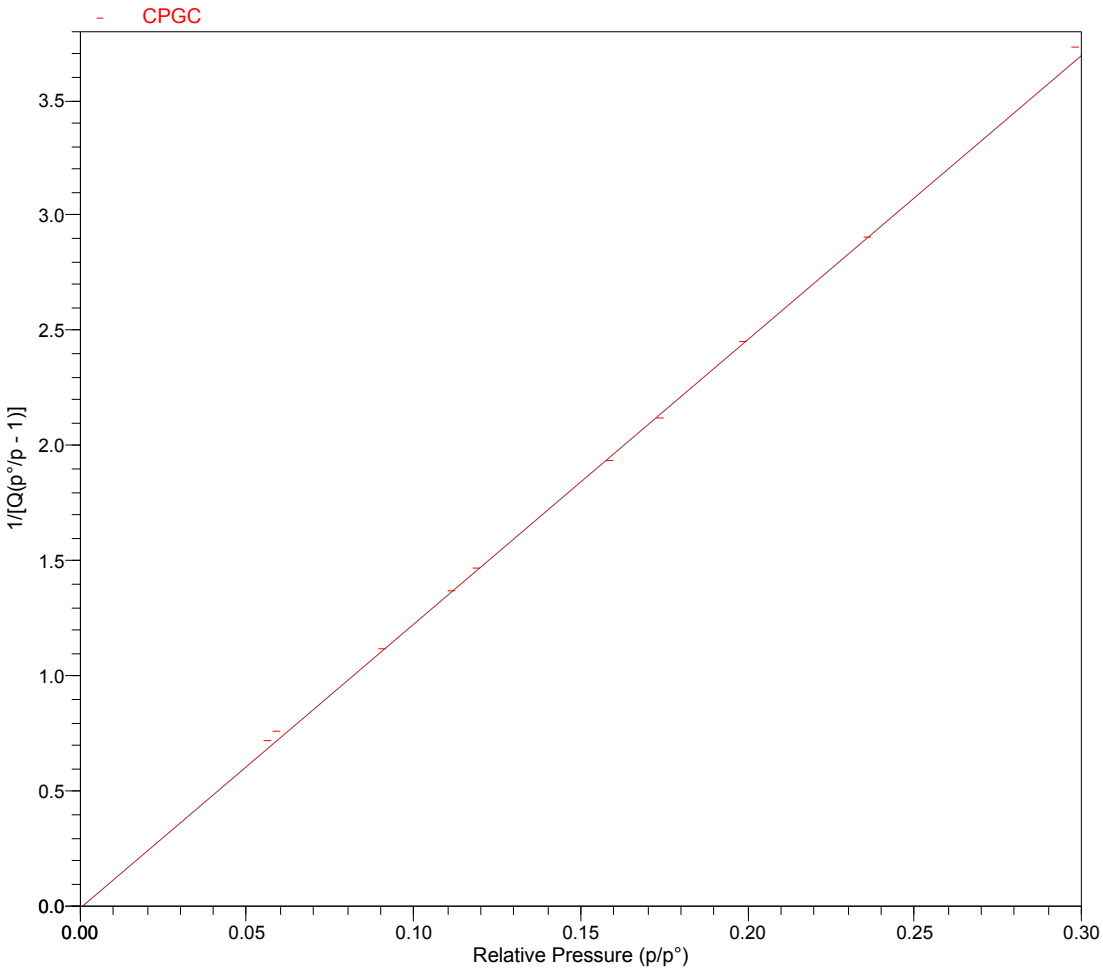

Sample: CPGC
Operator:
Submitter:
File: C:\...\STEINA~1\CPGC.SMP

Started: 10.05.2019 13:50:18
Completed: 10.05.2019 17:25:10
Report Time: 10.05.2019 18:01:17
Warm Free Space: 11.7008 cm³ Measured
Equilibration Interval: 5 s
Sample Density: 1.000 g/cm³

Analysis Adsorptive: N2
Analysis Bath Temp.: 77.300 K
Sample Mass: 1.1288 g
Cold Free Space: 34.2284 cm³ Measured
Low Pressure Dose: None
Automatic Degas: No

Langmuir Surface Area Report

Langmuir Surface Area: 0.5355 ± 0.0162 m²/g
Slope: 8.129877 ± 0.246004 g/cm³ STP
Y-Intercept: 213.559574 ± 31.524428 mmHg·g/cm³ STP
b: 0.038068 1/mmHg
Qm: 0.1230 cm³/g STP
Correlation Coefficient: 0.996358
Molecular Cross-Sectional Area: 0.1620 nm²

Pressure (mmHg)	Quantity Adsorbed (cm³/g STP)	p/Q (mmHg·g/cm³ STP)
43.52103	0.0842	517.142
45.60577	0.0836	545.210
69.72205	0.0901	773.727
85.47017	0.0923	925.837
91.16151	0.0927	983.705
121.51949	0.0982	1237.262
132.95638	0.0999	1331.051
151.88998	0.1018	1492.730
180.19241	0.1068	1686.483
227.54936	0.1144	1988.459

Sample: CPGC
Operator:
Submitter:
File: C:\...\STEINA~1\CPGC.SMP

Started:	10.05.2019 13:50:18	Analysis Adsorptive:	N2
Completed:	10.05.2019 17:25:10	Analysis Bath Temp.:	77.300 K
Report Time:	10.05.2019 18:01:17	Sample Mass:	1.1288 g
Warm Free Space:	11.7008 cm³ Measured	Cold Free Space:	34.2284 cm³ Measured
Equilibration Interval:	5 s	Low Pressure Dose:	None
Sample Density:	1.000 g/cm³	Automatic Degas:	No

Langmuir Surface Area Plot

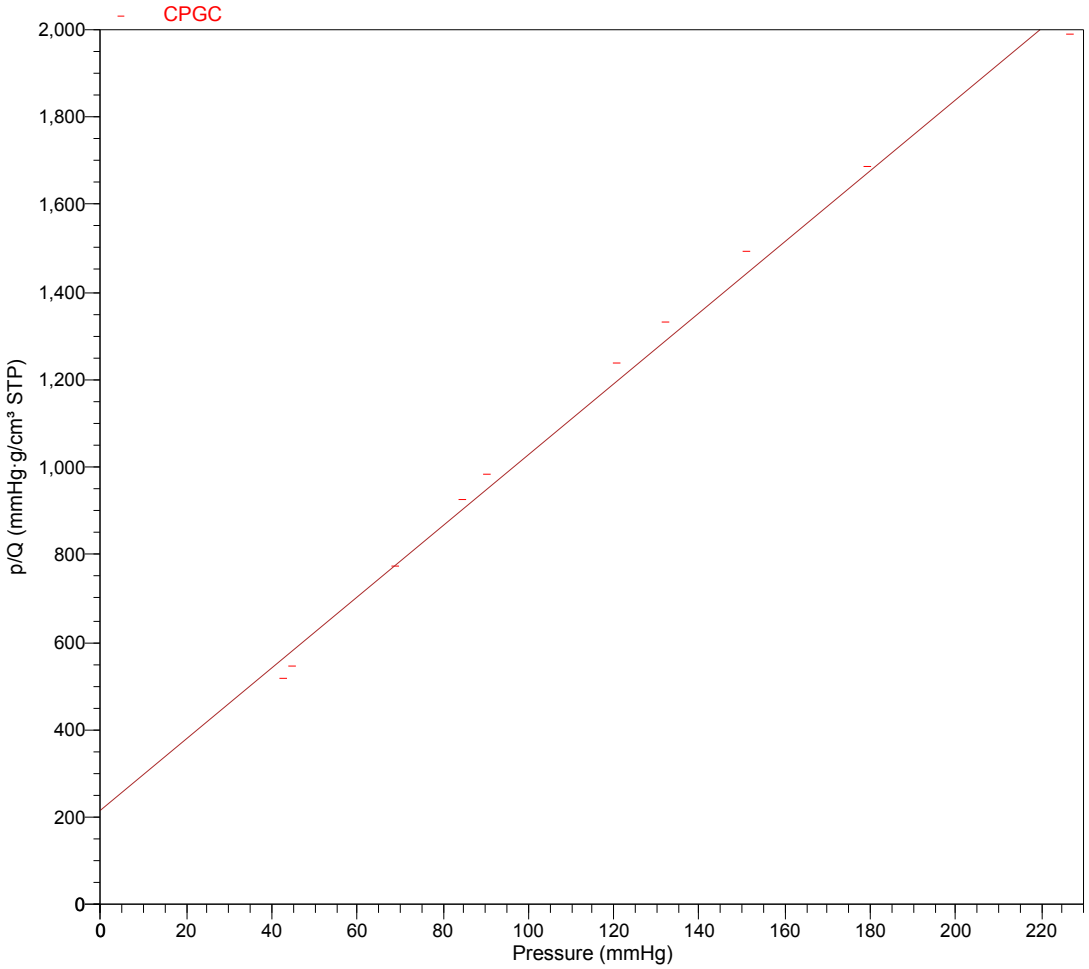

Sample: CPGC
Operator:
Submitter:
File: C:\...\STEINA~1\CPGC.SMP

Started:	10.05.2019 13:50:18	Analysis Adsorptive:	N2
Completed:	10.05.2019 17:25:10	Analysis Bath Temp.:	77.300 K
Report Time:	10.05.2019 18:01:17	Sample Mass:	1.1288 g
Warm Free Space:	11.7008 cm³ Measured	Cold Free Space:	34.2284 cm³ Measured
Equilibration Interval:	5 s	Low Pressure Dose:	None
Sample Density:	1.000 g/cm³	Automatic Degas:	No

Options Report

Sample Tube

Sample Tube: Sample Tube
Stem Diameter: 3/8 inch
Physical volume below mark: 1.0000 cm³
Use Isothermal Jacket: Yes
Use Filler Rod: No

Analysis Conditions

Preparation

Fast evacuation: No
Evacuation rate: 5.0 mmHg/s
Unrestricted evacuation from: 5.0 mmHg
Evacuation time: 0.10 h
Leak test: Yes
Leak test duration: 30 s

Free Space

Free-space type: Measured
Lower dewar for evacuation: Yes
Evacuation time: 0.10 h
Outgas test: No

p° and Temperature

p° and T type: Measure p° at intervals during analysis. Enter the Analysis Bath Temperature below.
p° and T type: Measure p° at intervals during analysis. Enter the Analysis Bath Temperature below.
Temperature: 77.300 K
Measurement interval: 120 min

Dosing

Use first pressure fixed dose: No
Use maximum volume increment: No
Target tolerance: 5.0% or 5.000 mmHg

Equilibration

Equilibration interval: 5 s
Minimum equilibration delay at p/p° >= 0.995: 600 s

Adsorptive Properties

Adsorptive: Nitrogen
Maximum manifold pressure: 1050.00 mmHg
Non-ideality factor: 0.0000620
Density conversion factor: 0.0015468
Molecular cross-sectional area: 0.162 nm²

Sample: CPGC
Operator:
Submitter:
File: C:\...\STEINA~1\CPGC.SMP

Started:	10.05.2019 13:50:18	Analysis Adsorptive:	N2
Completed:	10.05.2019 17:25:10	Analysis Bath Temp.:	77.300 K
Report Time:	10.05.2019 18:01:17	Sample Mass:	1.1288 g
Warm Free Space:	11.7008 cm³ Measured	Cold Free Space:	34.2284 cm³ Measured
Equilibration Interval:	5 s	Low Pressure Dose:	None
Sample Density:	1.000 g/cm³	Automatic Degas:	No

Summary Report

Surface Area

Single point surface area at p/p° = 0.299226393:	0.3491 m²/g
BET Surface Area:	0.3527 m²/g
Langmuir Surface Area:	0.5355 m²/g
t-Plot Micropore Area:	0.0924 m²/g
t-Plot External Surface Area:	0.2603 m²/g
BJH Adsorption cumulative surface area of pores between 17.000 Å and 3000.000 Å width:	0.3199 m²/g
BJH Desorption cumulative surface area of pores between 17.000 Å and 3000.000 Å width:	0.3557 m²/g

Pore Volume

Single point adsorption total pore volume of pores less than 1219.755 Å width at p/p° = 0.983869554:	0.001579 cm³/g
t-Plot micropore volume:	0.000045 cm³/g
BJH Adsorption cumulative volume of pores between 17.000 Å and 3000.000 Å width:	0.002588 cm³/g
BJH Desorption cumulative volume of pores between 17.000 Å and 3000.000 Å width:	0.002564 cm³/g

Pore Size

Adsorption average pore width (4V/A by BET):	179.0670 Å
BJH Adsorption average pore width (4V/A):	323.631 Å
BJH Desorption average pore width (4V/A):	288.350 Å

Sample: CPGC
Operator:
Submitter:
File: C:\...\STEINA~1\CPGC.SMP

Started:	10.05.2019 13:50:18	Analysis Adsorptive:	N2
Completed:	10.05.2019 17:25:10	Analysis Bath Temp.:	77.300 K
Report Time:	10.05.2019 18:01:17	Sample Mass:	1.1288 g
Warm Free Space:	11.7008 cm³ Measured	Cold Free Space:	34.2284 cm³ Measured
Equilibration Interval:	5 s	Low Pressure Dose:	None
Sample Density:	1.000 g/cm³	Automatic Degas:	No

Sample Log Report

Date	Time	Message
10.05.2019	14:08:12	Helium Purged: 30 seconds
10.05.2019	14:23:20	Measured free space on port 1, Warm: 11.7008 cm³, Cold: 34.2284 cm³
10.05.2019	14:36:54	Starting p° in p° tube measurement.

Sample: CPSA
Operator:
Submitter:
File: C:\...\STEINA~1\CPSA.SMP

Started: 10.05.2019 13:50:18
Completed: 10.05.2019 17:25:10
Report Time: 10.05.2019 18:03:52
Warm Free Space: 11.1238 cm³ Measured
Equilibration Interval: 5 s
Sample Density: 1.000 g/cm³

Analysis Adsorptive: N2
Analysis Bath Temp.: 77.300 K
Sample Mass: 1.1054 g
Cold Free Space: 31.9679 cm³ Measured
Low Pressure Dose: None
Automatic Degas: No

Isotherm Tabular Report

Relative Pressure (p/p°)	Absolute Pressure (mmHg)	Quantity Adsorbed (cm³/g STP)	Elapsed Time (h:min)	Saturation Pressure (mmHg)
			00:50	760.45886
0.010088919	7.67232	0.6493	00:58	
0.032444360	24.67300	0.7334	00:59	
0.056310195	42.82244	0.7810	01:01	
0.060207806	45.78656	0.7874	01:02	
0.079861617	60.73291	0.8173	01:03	
0.099829596	75.91823	0.8449	01:04	
0.112514621	85.56522	0.8612	01:06	
0.120056177	91.30060	0.8709	01:07	
0.139808930	106.32241	0.8957	01:08	
0.159776624	121.50774	0.9208	01:09	
0.174815352	132.94495	0.9398	01:11	
0.179942061	136.84399	0.9462	01:12	
0.199777222	151.92870	0.9714	01:13	
0.236751935	180.04794	1.0193	01:14	
0.249833176	189.99681	1.0370	01:16	
0.300711104	228.68962	1.1073	01:17	
0.349416755	265.73056	1.1789	01:18	
0.399853307	304.08798	1.2554	01:19	
0.449913941	342.16028	1.3327	01:21	
0.499749117	380.06070	1.4108	01:22	
0.549363609	417.79343	1.4922	01:23	
0.598773910	455.37100	1.5795	01:24	
0.647995459	492.80606	1.6759	01:26	
0.697714015	530.61841	1.7900	01:27	
0.738104825	561.33704	1.8995	01:28	
0.768473289	584.43365	1.9967	01:29	
0.798432258	607.22003	2.1061	01:31	
0.818767307	622.68628	2.1944	01:32	
0.838859673	637.96802	2.2915	01:33	
0.858514948	652.91858	2.4041	01:35	
0.873921327	664.63666	2.5085	01:36	
0.888737862	675.90619	2.6293	01:37	
0.903701496	687.28888	2.7746	01:39	
0.913958845	695.09113	2.8982	01:40	
0.924032628	702.75507	3.0396	01:42	
0.931974659	708.79651	3.1750	01:43	
0.938790373	713.98267	3.3285	01:45	
0.946311618	719.70544	3.5187	01:47	
0.952157059	724.15375	3.6847	01:49	
0.957401530	728.14502	3.8984	01:51	
0.962871952	732.30817	4.1747	01:53	
0.966708989	735.23041	4.4482	01:56	
0.970023945	737.75427	4.7711	01:58	
0.973882896	740.69324	5.1389	02:01	

Sample: CPSA
Operator:
Submitter:
File: C:\...\STEINA~1\CPSA.SMP

Started: 10.05.2019 13:50:18
Completed: 10.05.2019 17:25:10
Report Time: 10.05.2019 18:03:52
Warm Free Space: 11.1238 cm³ Measured
Equilibration Interval: 5 s
Sample Density: 1.000 g/cm³

Analysis Adsorptive: N2
Analysis Bath Temp.: 77.300 K
Sample Mass: 1.1054 g
Cold Free Space: 31.9679 cm³ Measured
Low Pressure Dose: None
Automatic Degas: No

Isotherm Tabular Report

Relative Pressure (p/p°)	Absolute Pressure (mmHg)	Quantity Adsorbed (cm³/g STP)	Elapsed Time (h:min)	Saturation Pressure (mmHg)
0.975437582	741.87970	5.4034	02:04	
0.978201301	743.98438	5.8888	02:06	
0.981117542	746.20642	6.4388	02:09	
0.982335922	747.13715	6.9306	02:12	
0.984623682	748.88123	7.6728	02:15	
0.986093827	750.00482	8.4197	02:19	
0.990191390	753.12408	9.4062	02:21	
0.984719660	748.96509	8.7920	02:23	
0.981451060	746.48309	8.1942	02:26	
0.978342426	744.12274	7.5698	02:29	
0.977308115	743.33875	7.2740	02:31	
0.973784261	740.66388	6.5560	02:35	
0.972478108	739.67444	6.2492	02:38	
0.967736219	736.07306	5.4359	02:42	
0.965482111	734.36255	5.1000	02:45	
0.958948894	729.39856	4.4564	02:49	
			02:51	760.62573
0.955120136	726.48895	4.1716	02:52	
0.948285328	721.29022	3.8227	02:54	
0.942321402	716.75391	3.5749	02:57	
0.933728302	710.21777	3.3283	02:59	
0.926617939	704.80945	3.1725	03:01	
0.916580699	697.17487	2.9927	03:03	
0.906036322	689.15454	2.8428	03:04	
0.891358048	677.98987	2.6811	03:06	
0.876541916	666.72034	2.5449	03:07	
0.861003754	654.90161	2.4327	03:09	
0.841579648	640.12714	2.3134	03:10	
0.821290198	624.69446	2.2067	03:11	
0.801144062	609.37079	2.1161	03:13	
0.771528408	586.84436	2.0046	03:14	
0.741620669	564.09576	1.9052	03:15	
0.701813387	533.81732	1.7937	03:16	
0.652090155	495.99655	1.6764	03:18	
0.602058306	457.94104	1.5740	03:19	
0.551976787	419.84775	1.4823	03:20	
0.501911838	381.76706	1.3970	03:22	
0.452342953	344.06369	1.2934	03:23	
0.402206347	305.92850	1.2150	03:24	
0.352042137	267.77231	1.1390	03:25	
0.300974026	228.92859	1.0638	03:27	
0.251796488	191.52289	0.9951	03:28	
0.201825223	153.51346	0.9298	03:29	
0.142130912	108.10843	0.8553	03:31	

Sample: CPSA
Operator:
Submitter:
File: C:\...\STEINA~1\CPSA.SMP

Started:	10.05.2019 13:50:18	Analysis Adsorptive:	N2
Completed:	10.05.2019 17:25:10	Analysis Bath Temp.:	77.300 K
Report Time:	10.05.2019 18:03:52	Sample Mass:	1.1054 g
Warm Free Space:	11.1238 cm³ Measured	Cold Free Space:	31.9679 cm³ Measured
Equilibration Interval:	5 s	Low Pressure Dose:	None
Sample Density:	1.000 g/cm³	Automatic Degas:	No

Isotherm Linear Plot

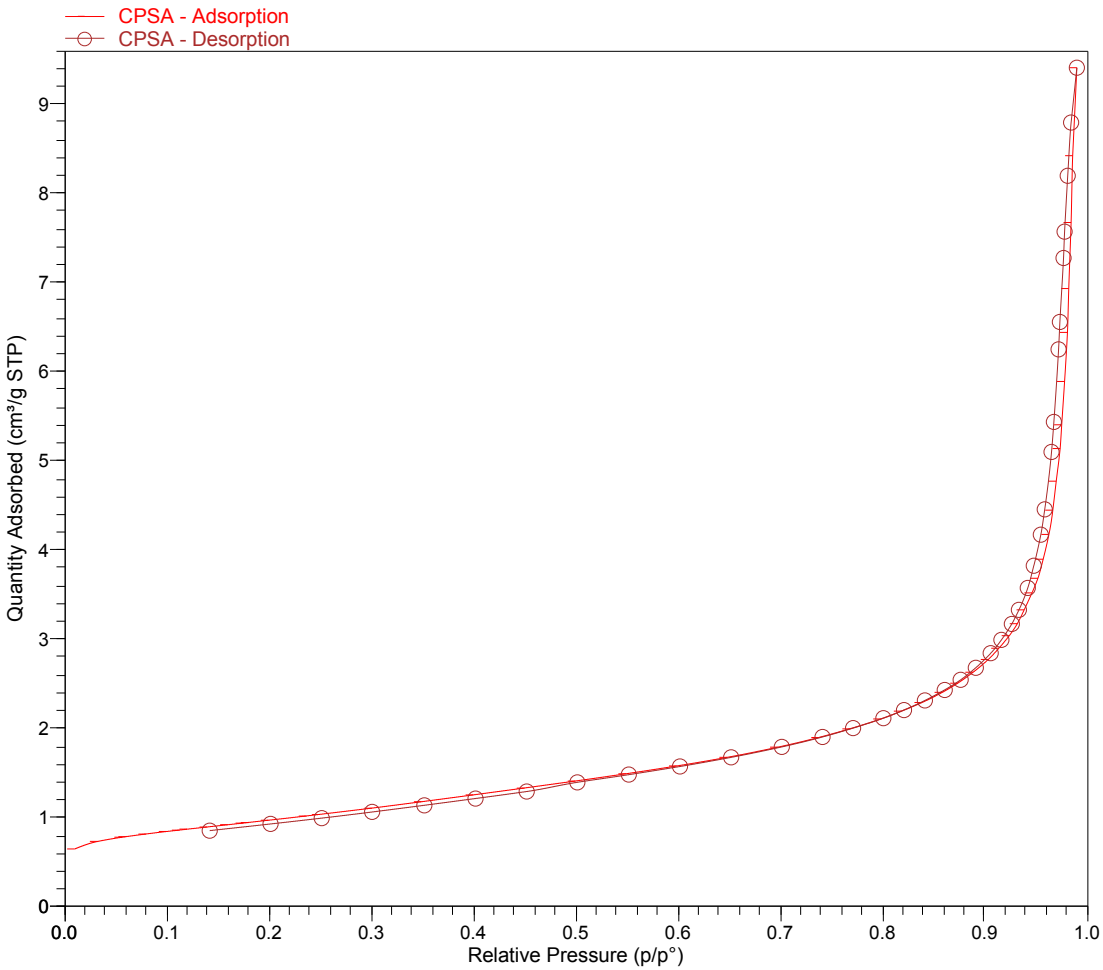

Sample: CPSA
Operator:
Submitter:
File: C:\...\STEINA~1\CPSA.SMP

Started:	10.05.2019 13:50:18	Analysis Adsorptive:	N2
Completed:	10.05.2019 17:25:10	Analysis Bath Temp.:	77.300 K
Report Time:	10.05.2019 18:03:52	Sample Mass:	1.1054 g
Warm Free Space:	11.1238 cm³ Measured	Cold Free Space:	31.9679 cm³ Measured
Equilibration Interval:	5 s	Low Pressure Dose:	None
Sample Density:	1.000 g/cm³	Automatic Degas:	No

Isotherm Log Plot

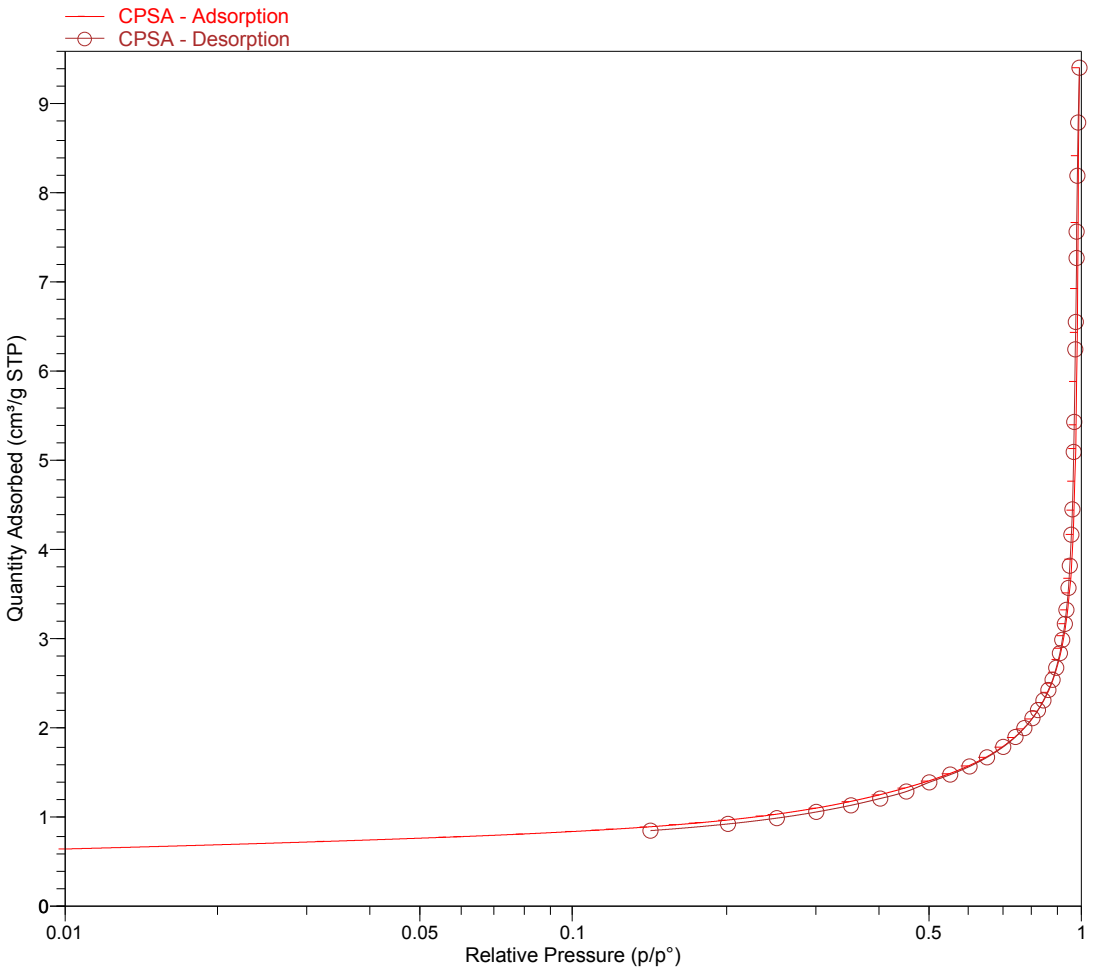

Sample: CPSA
Operator:
Submitter:
File: C:\...\STEINA~1\CPSA.SMP

Started: 10.05.2019 13:50:18
Completed: 10.05.2019 17:25:10
Report Time: 10.05.2019 18:03:52
Warm Free Space: 11.1238 cm³ Measured
Equilibration Interval: 5 s
Sample Density: 1.000 g/cm³

Analysis Adsorptive: N2
Analysis Bath Temp.: 77.300 K
Sample Mass: 1.1054 g
Cold Free Space: 31.9679 cm³ Measured
Low Pressure Dose: None
Automatic Degas: No

BET Surface Area Report

BET Surface Area: 3.4141 ± 0.0115 m²/g
Slope: 1.270830 ± 0.004217 g/cm³ STP
Y-Intercept: 0.004221 ± 0.000709 g/cm³ STP
C: 302.050107
Qm: 0.7843 cm³/g STP
Correlation Coefficient: 0.9999560
Molecular Cross-Sectional Area: 0.1620 nm²

Relative Pressure (p/p°)	Quantity Adsorbed (cm³/g STP)	1/[Q(p°/p - 1)]
0.056310195	0.7810	0.076399
0.060207806	0.7874	0.081360
0.079861617	0.8173	0.106201
0.112514621	0.8612	0.147208
0.120056177	0.8709	0.156669
0.159776624	0.9208	0.206510
0.174815352	0.9398	0.225429
0.199777222	0.9714	0.257013
0.236751935	1.0193	0.304320
0.300711104	1.1073	0.388344

Sample: CPSA
Operator:
Submitter:
File: C:\...\STEINA~1\CPSA.SMP

Started:	10.05.2019 13:50:18	Analysis Adsorptive:	N2
Completed:	10.05.2019 17:25:10	Analysis Bath Temp.:	77.300 K
Report Time:	10.05.2019 18:03:52	Sample Mass:	1.1054 g
Warm Free Space:	11.1238 cm³ Measured	Cold Free Space:	31.9679 cm³ Measured
Equilibration Interval:	5 s	Low Pressure Dose:	None
Sample Density:	1.000 g/cm³	Automatic Degas:	No

BET Surface Area Plot

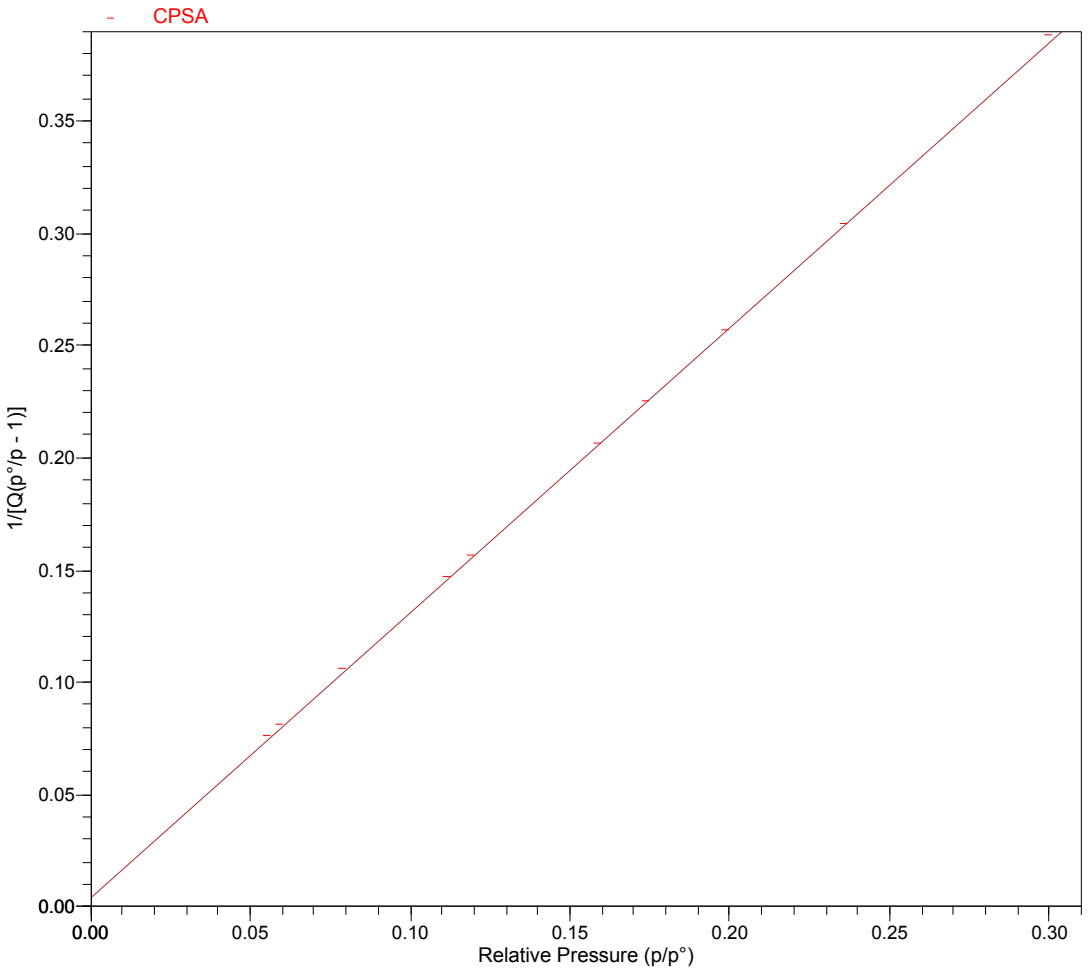

Sample: CPSA
Operator:
Submitter:
File: C:\...\STEINA~1\CPSA.SMP

Started: 10.05.2019 13:50:18
Completed: 10.05.2019 17:25:10
Report Time: 10.05.2019 18:03:52
Warm Free Space: 11.1238 cm³ Measured
Equilibration Interval: 5 s
Sample Density: 1.000 g/cm³

Analysis Adsorptive: N2
Analysis Bath Temp.: 77.300 K
Sample Mass: 1.1054 g
Cold Free Space: 31.9679 cm³ Measured
Low Pressure Dose: None
Automatic Degas: No

Langmuir Surface Area Report

Langmuir Surface Area: 5.2134 ± 0.1935 m²/g
Slope: 0.835001 ± 0.030993 g/cm³ STP
Y-Intercept: 25.146685 ± 3.963135 mmHg·g/cm³ STP
b: 0.033205 1/mmHg
Qm: 1.1976 cm³/g STP
Correlation Coefficient: 0.994534
Molecular Cross-Sectional Area: 0.1620 nm²

Pressure (mmHg)	Quantity Adsorbed (cm³/g STP)	p/Q (mmHg·g/cm³ STP)
42.82244	0.7810	54.828
45.78656	0.7874	58.147
60.73291	0.8173	74.314
85.56522	0.8612	99.353
91.30060	0.8709	104.840
121.50774	0.9208	131.955
132.94495	0.9398	141.466
151.92870	0.9714	156.409
180.04794	1.0193	176.641
228.68962	1.1073	206.524

Sample: CPSA
Operator:
Submitter:
File: C:\...\STEINA~1\CPSA.SMP

Started:	10.05.2019 13:50:18	Analysis Adsorptive:	N2
Completed:	10.05.2019 17:25:10	Analysis Bath Temp.:	77.300 K
Report Time:	10.05.2019 18:03:52	Sample Mass:	1.1054 g
Warm Free Space:	11.1238 cm³ Measured	Cold Free Space:	31.9679 cm³ Measured
Equilibration Interval:	5 s	Low Pressure Dose:	None
Sample Density:	1.000 g/cm³	Automatic Degas:	No

Langmuir Surface Area Plot

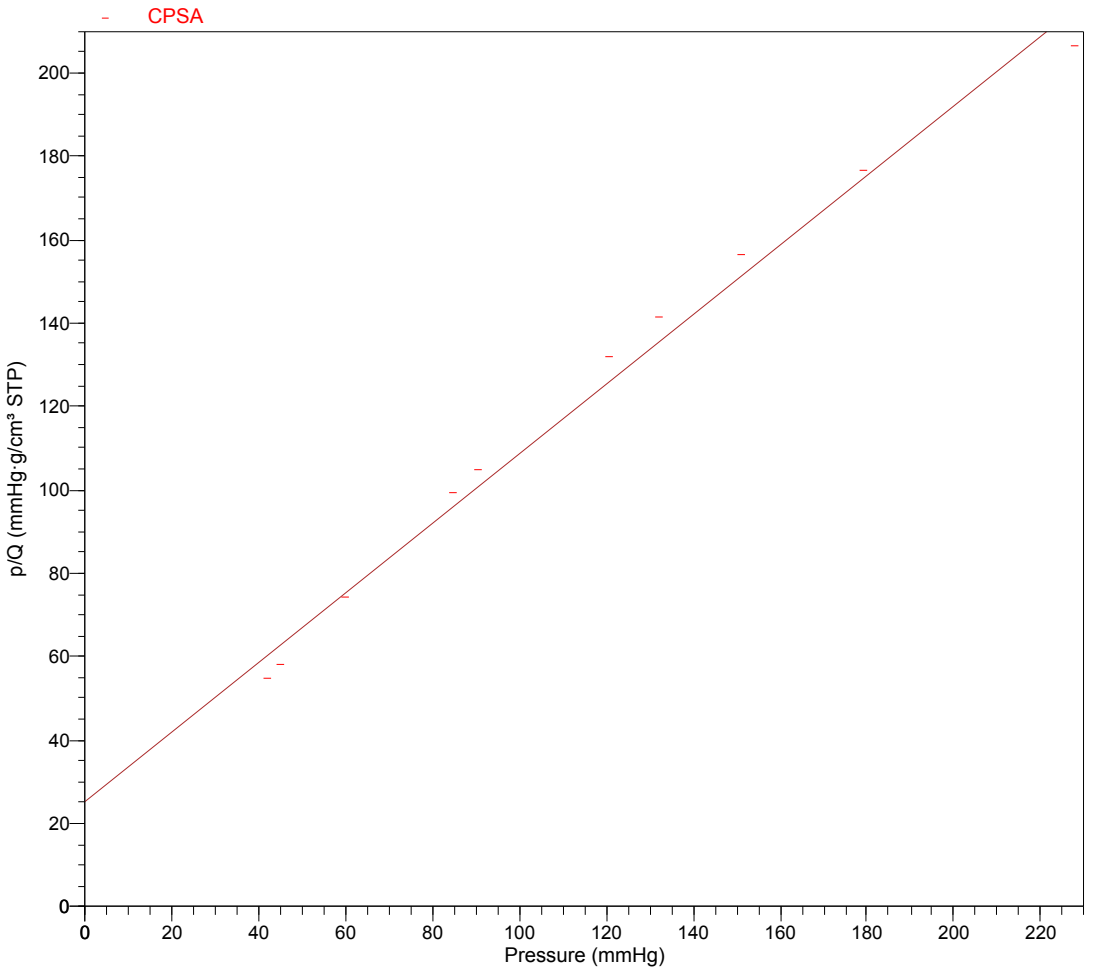

Sample: CPSA
Operator:
Submitter:
File: C:\...\STEINA~1\CPSA.SMP

Started:	10.05.2019 13:50:18	Analysis Adsorptive:	N2
Completed:	10.05.2019 17:25:10	Analysis Bath Temp.:	77.300 K
Report Time:	10.05.2019 18:03:52	Sample Mass:	1.1054 g
Warm Free Space:	11.1238 cm³ Measured	Cold Free Space:	31.9679 cm³ Measured
Equilibration Interval:	5 s	Low Pressure Dose:	None
Sample Density:	1.000 g/cm³	Automatic Degas:	No

Options Report

Sample Tube

Sample Tube: Sample Tube
Stem Diameter: 3/8 inch
Physical volume below mark: 1.0000 cm³
Use Isothermal Jacket: Yes
Use Filler Rod: No

Analysis Conditions

Preparation

Fast evacuation: No
Evacuation rate: 5.0 mmHg/s
Unrestricted evacuation from: 5.0 mmHg
Evacuation time: 0.10 h
Leak test: Yes
Leak test duration: 30 s

Free Space

Free-space type: Measured
Lower dewar for evacuation: Yes
Evacuation time: 0.10 h
Outgas test: No

p° and Temperature

p° and T type: Measure p° at intervals during analysis. Enter the Analysis Bath Temperature below.
p° and T type: Measure p° at intervals during analysis. Enter the Analysis Bath Temperature below.
Temperature: 77.300 K
Measurement interval: 120 min

Dosing

Use first pressure fixed dose: No
Use maximum volume increment: No
Target tolerance: 5.0% or 5.000 mmHg

Equilibration

Equilibration interval: 5 s
Minimum equilibration delay at p/p° >= 0.995: 600 s

Adsorptive Properties

Adsorptive: Nitrogen
Maximum manifold pressure: 1050.00 mmHg
Non-ideality factor: 0.0000620
Density conversion factor: 0.0015468
Molecular cross-sectional area: 0.162 nm²

Sample: CPSA
Operator:
Submitter:
File: C:\...\STEINA~1\CPSA.SMP

Started:	10.05.2019 13:50:18	Analysis Adsorptive:	N2
Completed:	10.05.2019 17:25:10	Analysis Bath Temp.:	77.300 K
Report Time:	10.05.2019 18:03:52	Sample Mass:	1.1054 g
Warm Free Space:	11.1238 cm³ Measured	Cold Free Space:	31.9679 cm³ Measured
Equilibration Interval:	5 s	Low Pressure Dose:	None
Sample Density:	1.000 g/cm³	Automatic Degas:	No

Summary Report

Surface Area

Single point surface area at p/p° = 0.300711104:	3.3709 m²/g
BET Surface Area:	3.4141 m²/g
Langmuir Surface Area:	5.2134 m²/g
t-Plot Micropore Area:	0.5274 m²/g
t-Plot External Surface Area:	2.8867 m²/g
BJH Adsorption cumulative surface area of pores between 17.000 Å and 3000.000 Å width:	3.3949 m²/g
BJH Desorption cumulative surface area of pores between 17.000 Å and 3000.000 Å width:	3.4040 m²/g

Pore Volume

Single point adsorption total pore volume of pores less than 1115.730 Å width at p/p° = 0.982335922:	0.010720 cm³/g
Single point desorption total pore volume of pores less than 1063.500 Å width at p/p° = 0.981451060:	0.012675 cm³/g
t-Plot micropore volume:	0.000244 cm³/g
BJH Adsorption cumulative volume of pores between 17.000 Å and 3000.000 Å width:	0.014763 cm³/g
BJH Desorption cumulative volume of pores between 17.000 Å and 3000.000 Å width:	0.013774 cm³/g

Pore Size

Adsorption average pore width (4V/A by BET):	125.5979 Å
Desorption average pore width (4V/A by BET):	148.4981 Å
BJH Adsorption average pore width (4V/A):	173.939 Å
BJH Desorption average pore width (4V/A):	161.860 Å

Sample: CPSA
Operator:
Submitter:
File: C:\...\STEINA~1\CPSA.SMP

Started:	10.05.2019 13:50:18	Analysis Adsorptive:	N2
Completed:	10.05.2019 17:25:10	Analysis Bath Temp.:	77.300 K
Report Time:	10.05.2019 18:03:52	Sample Mass:	1.1054 g
Warm Free Space:	11.1238 cm³ Measured	Cold Free Space:	31.9679 cm³ Measured
Equilibration Interval:	5 s	Low Pressure Dose:	None
Sample Density:	1.000 g/cm³	Automatic Degas:	No

Sample Log Report

Date	Time	Message
10.05.2019	14:24:20	Measured free space on port 2, Warm: 11.1238 cm³, Cold: 31.9679 cm³
10.05.2019	14:36:54	Starting p° in p° tube measurement.

Sample: AL-CPSA
Operator:
Submitter:
File: C:\...\STEINA~1\AL-CPSA.SMP

Started: 22.05.2019 14:03:19
Completed: 22.05.2019 17:57:46
Report Time: 22.05.2019 18:25:24
Warm Free Space: 11.6061 cm³ Measured
Equilibration Interval: 5 s
Sample Density: 1.000 g/cm³

Analysis Adsorptive: N2
Analysis Bath Temp.: 77.300 K
Sample Mass: 0.9878 g
Cold Free Space: 34.0042 cm³ Measured
Low Pressure Dose: None
Automatic Degas: No

Isotherm Tabular Report

Relative Pressure (p/p°)	Absolute Pressure (mmHg)	Quantity Adsorbed (cm³/g STP)	Elapsed Time (h:min)	Saturation Pressure (mmHg)
			00:47	764.90338
0.010286613	7.86715	1.0147	00:57	
0.031460374	24.06005	1.1595	00:59	
0.055660986	42.56681	1.2451	01:01	
0.059745092	45.68949	1.2581	01:02	
0.079852068	61.06524	1.3131	01:03	
0.099806961	76.32426	1.3618	01:04	
0.112311236	85.88407	1.3917	01:06	
0.119847610	91.64581	1.4097	01:07	
0.139755131	106.86730	1.4541	01:08	
0.159706839	122.12215	1.4987	01:09	
0.174749062	133.62061	1.5329	01:11	
0.179904134	137.56044	1.5446	01:12	
0.199721236	152.71106	1.5892	01:13	
0.236654660	180.94856	1.6731	01:14	
0.249829840	191.01701	1.7054	01:16	
0.299279879	228.82269	1.8242	01:17	
0.349516508	267.22870	1.9518	01:18	
0.398953220	305.01770	2.0834	01:20	
0.448866249	343.17358	2.2186	01:21	
0.498660705	381.23773	2.3552	01:22	
0.548513465	419.33942	2.4945	01:24	
0.598355090	457.43692	2.6406	01:25	
0.648076440	495.43436	2.8026	01:27	
0.697910745	533.52356	2.9909	01:28	
0.738223673	564.32507	3.1764	01:30	
0.768836231	587.71808	3.3458	01:31	
0.798626457	610.47314	3.5435	01:33	
0.819243665	626.22412	3.7085	01:34	
0.839137091	641.41229	3.8962	01:36	
0.859046674	656.62128	4.1167	01:37	
0.874087463	668.09888	4.3288	01:39	
0.889167278	679.60565	4.5920	01:41	
0.904351685	691.19171	4.8974	01:43	
0.914120028	698.63776	5.1605	01:45	
0.924712709	706.71338	5.4990	01:47	
0.932296912	712.47925	5.8181	01:50	
0.940414067	718.66211	6.1772	01:52	
0.946450047	723.24396	6.5023	01:55	
0.952636748	727.95093	6.9204	01:57	
0.958640929	732.50775	7.4337	02:00	
0.963930928	736.51849	7.9937	02:03	
0.968391861	739.89545	8.5343	02:06	
0.971224202	742.03839	8.9796	02:08	
0.974266999	744.33142	9.6128	02:11	

Sample: AL-CPSA
Operator:
Submitter:
File: C:\...\STEINA~1\AL-CPSA.SMP

Started: 22.05.2019 14:03:19
Completed: 22.05.2019 17:57:46
Report Time: 22.05.2019 18:25:24
Warm Free Space: 11.6061 cm³ Measured
Equilibration Interval: 5 s
Sample Density: 1.000 g/cm³

Analysis Adsorptive: N2
Analysis Bath Temp.: 77.300 K
Sample Mass: 0.9878 g
Cold Free Space: 34.0042 cm³ Measured
Low Pressure Dose: None
Automatic Degas: No

Isotherm Tabular Report

Relative Pressure (p/p°)	Absolute Pressure (mmHg)	Quantity Adsorbed (cm³/g STP)	Elapsed Time (h:min)	Saturation Pressure (mmHg)
0.977812105	747.00800	10.3849	02:14	
0.979813030	748.50470	11.0729	02:17	
0.982851149	750.79358	12.0693	02:20	
0.983870046	751.53986	12.7639	02:23	
0.988968601	755.41296	14.0554	02:25	
0.989872345	756.09253	14.9630	02:26	
0.990866593	756.83044	16.0745	02:28	
0.991404733	757.23071	16.7881	02:29	
0.988070442	754.66254	15.9660	02:31	
0.984446590	751.87335	15.2734	02:33	
0.982056293	750.02643	14.5225	02:35	
0.980992442	749.19263	14.1773	02:37	
0.978774153	747.46661	13.5376	02:40	
0.977046981	746.11578	12.8474	02:43	
0.974309671	743.99371	11.9692	02:46	
			02:48	763.58942
0.971137868	741.55060	11.0333	02:50	
0.966267617	737.83173	9.8703	02:54	
0.960087043	733.11230	8.7956	02:59	
0.955260435	729.42676	8.1174	03:03	
0.948069760	723.93604	7.4009	03:06	
0.942325934	719.55011	6.9492	03:09	
0.934900420	713.88007	6.4668	03:12	
0.926344748	707.34705	6.0308	03:15	
0.916888245	700.12616	5.6422	03:18	
0.906618114	692.28400	5.3010	03:20	
0.892067470	681.17328	4.9085	03:23	
0.876675942	669.42047	4.5847	03:25	
0.861819559	658.07629	4.3325	03:27	
0.841869035	642.84229	4.0604	03:29	
0.821694702	627.43738	3.8404	03:31	
0.801640426	612.12415	3.6592	03:33	
0.771933015	589.43988	3.4393	03:34	
0.741887171	566.49719	3.2541	03:36	
0.701975253	536.02087	3.0571	03:38	
0.652464752	498.21518	2.8583	03:39	
0.602249971	459.87170	2.6896	03:40	
0.552062447	421.54904	2.5413	03:42	
0.501760300	383.13885	2.4066	03:43	
0.452823111	345.77094	2.2216	03:45	
0.401942217	306.91882	2.0610	03:46	
0.351842099	268.66290	1.9222	03:48	
0.301621822	230.31523	1.7962	03:49	
0.251019372	191.67574	1.6774	03:51	
0.201432476	153.81171	1.5680	03:52	

Sample: AL-CPSA
Operator:
Submitter:
File: C:\...\STEINA~1\AL-CPSA.SMP

Started: 22.05.2019 14:03:19
Completed: 22.05.2019 17:57:46
Report Time: 22.05.2019 18:25:24
Warm Free Space: 11.6061 cm³ Measured
Equilibration Interval: 5 s
Sample Density: 1.000 g/cm³

Analysis Adsorptive: N2
Analysis Bath Temp.: 77.300 K
Sample Mass: 0.9878 g
Cold Free Space: 34.0042 cm³ Measured
Low Pressure Dose: None
Automatic Degas: No

Isotherm Tabular Report

Relative Pressure (p/p°)	Absolute Pressure (mmHg)	Quantity Adsorbed (cm³/g STP)	Elapsed Time (h:min)	Saturation Pressure (mmHg)
0.141455361	108.01382	1.4403	03:53	

Sample: AL-CPSA
Operator:
Submitter:
File: C:\...\STEINA~1\AL-CPSA.SMP

Started:	22.05.2019 14:03:19	Analysis Adsorptive:	N2
Completed:	22.05.2019 17:57:46	Analysis Bath Temp.:	77.300 K
Report Time:	22.05.2019 18:25:24	Sample Mass:	0.9878 g
Warm Free Space:	11.6061 cm³ Measured	Cold Free Space:	34.0042 cm³ Measured
Equilibration Interval:	5 s	Low Pressure Dose:	None
Sample Density:	1.000 g/cm³	Automatic Degas:	No

Isotherm Linear Plot

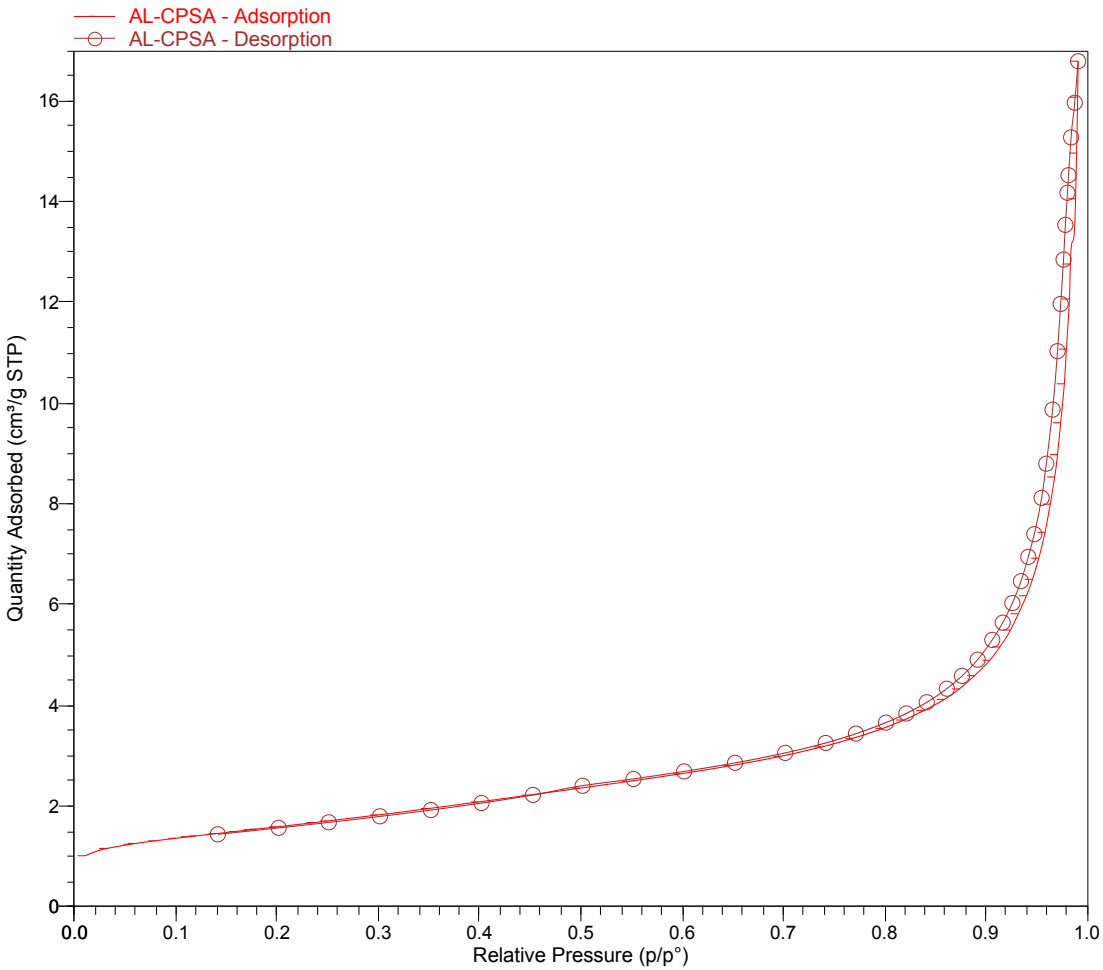

Sample: AL-CPSA
Operator:
Submitter:
File: C:\...\STEINA~1\AL-CPSA.SMP

Started:	22.05.2019 14:03:19	Analysis Adsorptive:	N2
Completed:	22.05.2019 17:57:46	Analysis Bath Temp.:	77.300 K
Report Time:	22.05.2019 18:25:24	Sample Mass:	0.9878 g
Warm Free Space:	11.6061 cm³ Measured	Cold Free Space:	34.0042 cm³ Measured
Equilibration Interval:	5 s	Low Pressure Dose:	None
Sample Density:	1.000 g/cm³	Automatic Degas:	No

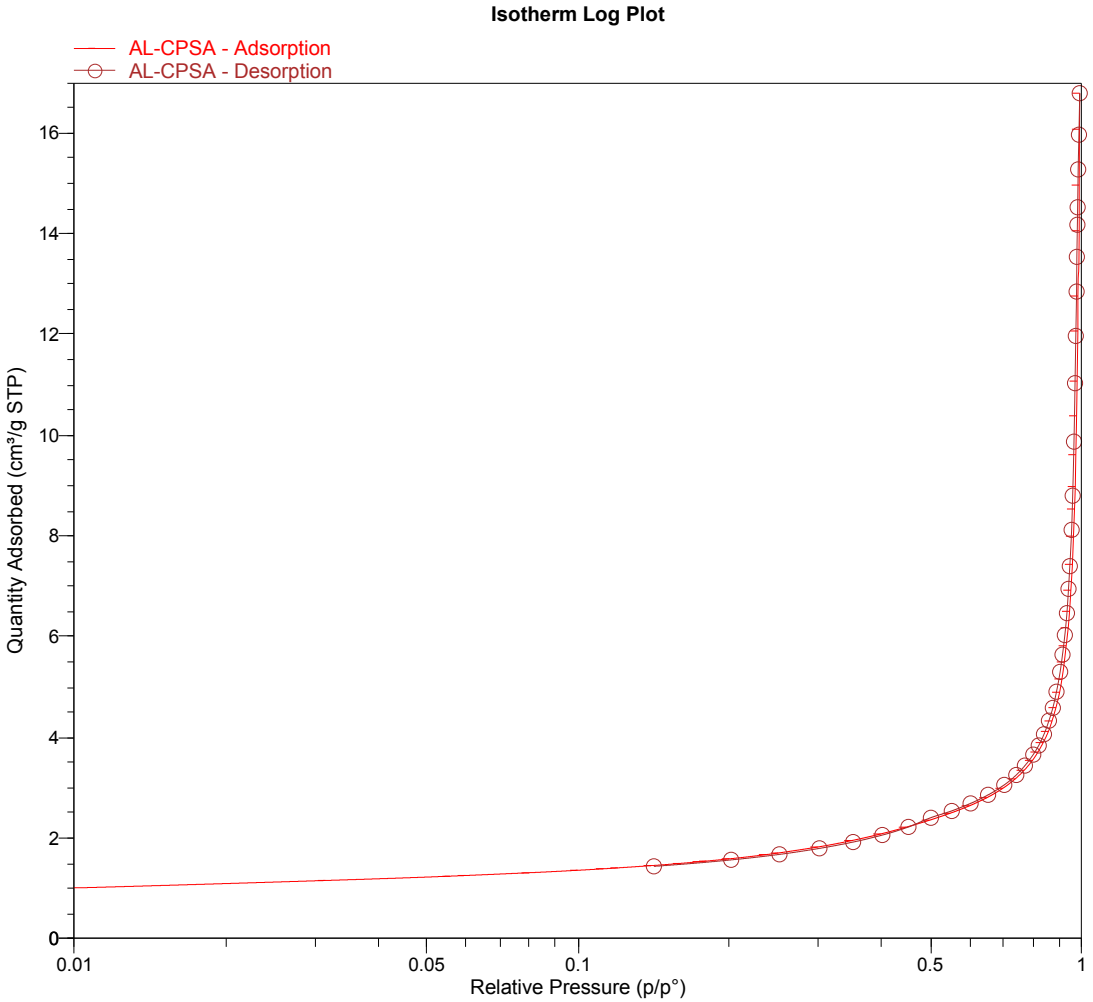

Sample: AL-CPSA
Operator:
Submitter:
File: C:\...\STEINA~1\AL-CPSA.SMP

Started: 22.05.2019 14:03:19
Completed: 22.05.2019 17:57:46
Report Time: 22.05.2019 18:25:24
Warm Free Space: 11.6061 cm³ Measured
Equilibration Interval: 5 s
Sample Density: 1.000 g/cm³

Analysis Adsorptive: N2
Analysis Bath Temp.: 77.300 K
Sample Mass: 0.9878 g
Cold Free Space: 34.0042 cm³ Measured
Low Pressure Dose: None
Automatic Degas: No

BET Surface Area Report

BET Surface Area: 5.6608 ± 0.0104 m²/g
Slope: 0.764161 ± 0.001387 g/cm³ STP
Y-Intercept: 0.004850 ± 0.000233 g/cm³ STP
C: 158.559195
Qm: 1.3004 cm³/g STP
Correlation Coefficient: 0.9999868
Molecular Cross-Sectional Area: 0.1620 nm²

Relative Pressure (p/p°)	Quantity Adsorbed (cm³/g STP)	1/[Q(p°/p - 1)]
0.055660986	1.2451	0.047339
0.059745092	1.2581	0.050504
0.079852068	1.3131	0.066091
0.112311236	1.3917	0.090911
0.119847610	1.4097	0.096590
0.159706839	1.4987	0.126813
0.174749062	1.5329	0.138134
0.199721236	1.5892	0.157035
0.236654660	1.6731	0.185304
0.299279879	1.8242	0.234131

Sample: AL-CPSA
Operator:
Submitter:
File: C:\...\STEINA~1\AL-CPSA.SMP

Started:	22.05.2019 14:03:19	Analysis Adsorptive:	N2
Completed:	22.05.2019 17:57:46	Analysis Bath Temp.:	77.300 K
Report Time:	22.05.2019 18:25:24	Sample Mass:	0.9878 g
Warm Free Space:	11.6061 cm³ Measured	Cold Free Space:	34.0042 cm³ Measured
Equilibration Interval:	5 s	Low Pressure Dose:	None
Sample Density:	1.000 g/cm³	Automatic Degas:	No

BET Surface Area Plot

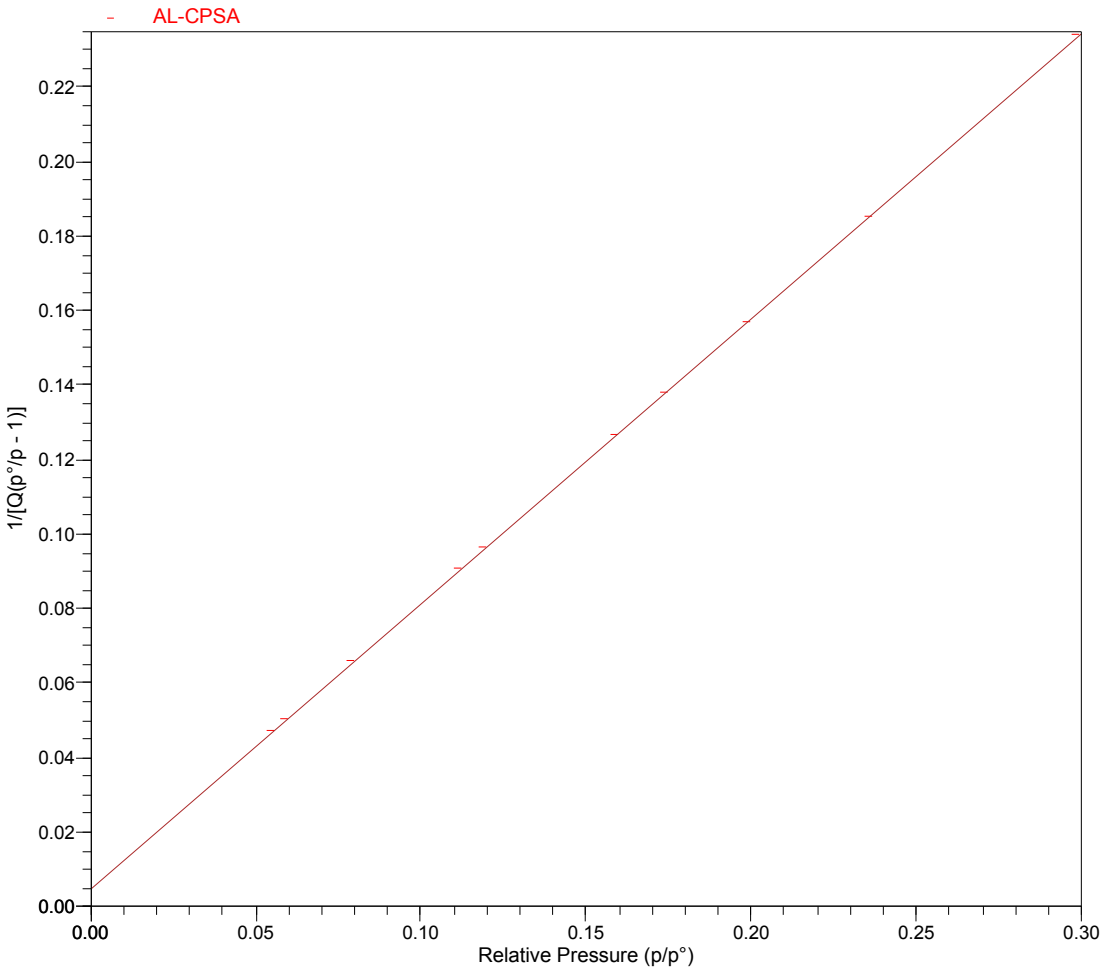

Sample: AL-CPSA
Operator:
Submitter:
File: C:\...\STEINA~1\AL-CPSA.SMP

Started: 22.05.2019 14:03:19
Completed: 22.05.2019 17:57:46
Report Time: 22.05.2019 18:25:24
Warm Free Space: 11.6061 cm³ Measured
Equilibration Interval: 5 s
Sample Density: 1.000 g/cm³

Analysis Adsorptive: N2
Analysis Bath Temp.: 77.300 K
Sample Mass: 0.9878 g
Cold Free Space: 34.0042 cm³ Measured
Low Pressure Dose: None
Automatic Degas: No

Langmuir Surface Area Report

Langmuir Surface Area: 8.6811 ± 0.3423 m²/g
Slope: 0.501458 ± 0.019774 g/cm³ STP
Y-Intercept: 16.785322 ± 2.536940 mmHg·g/cm³ STP
b: 0.029875 1/mmHg
Qm: 1.9942 cm³/g STP
Correlation Coefficient: 0.993837
Molecular Cross-Sectional Area: 0.1620 nm²

Pressure (mmHg)	Quantity Adsorbed (cm³/g STP)	p/Q (mmHg·g/cm³ STP)
42.56681	1.2451	34.187
45.68949	1.2581	36.315
61.06524	1.3131	46.506
85.88407	1.3917	61.712
91.64581	1.4097	65.009
122.12215	1.4987	81.483
133.62061	1.5329	87.166
152.71106	1.5892	96.092
180.94856	1.6731	108.155
228.82269	1.8242	125.437

Sample: AL-CPSA
Operator:
Submitter:
File: C:\...\STEINA~1\AL-CPSA.SMP

Started:	22.05.2019 14:03:19	Analysis Adsorptive:	N2
Completed:	22.05.2019 17:57:46	Analysis Bath Temp.:	77.300 K
Report Time:	22.05.2019 18:25:24	Sample Mass:	0.9878 g
Warm Free Space:	11.6061 cm³ Measured	Cold Free Space:	34.0042 cm³ Measured
Equilibration Interval:	5 s	Low Pressure Dose:	None
Sample Density:	1.000 g/cm³	Automatic Degas:	No

Langmuir Surface Area Plot

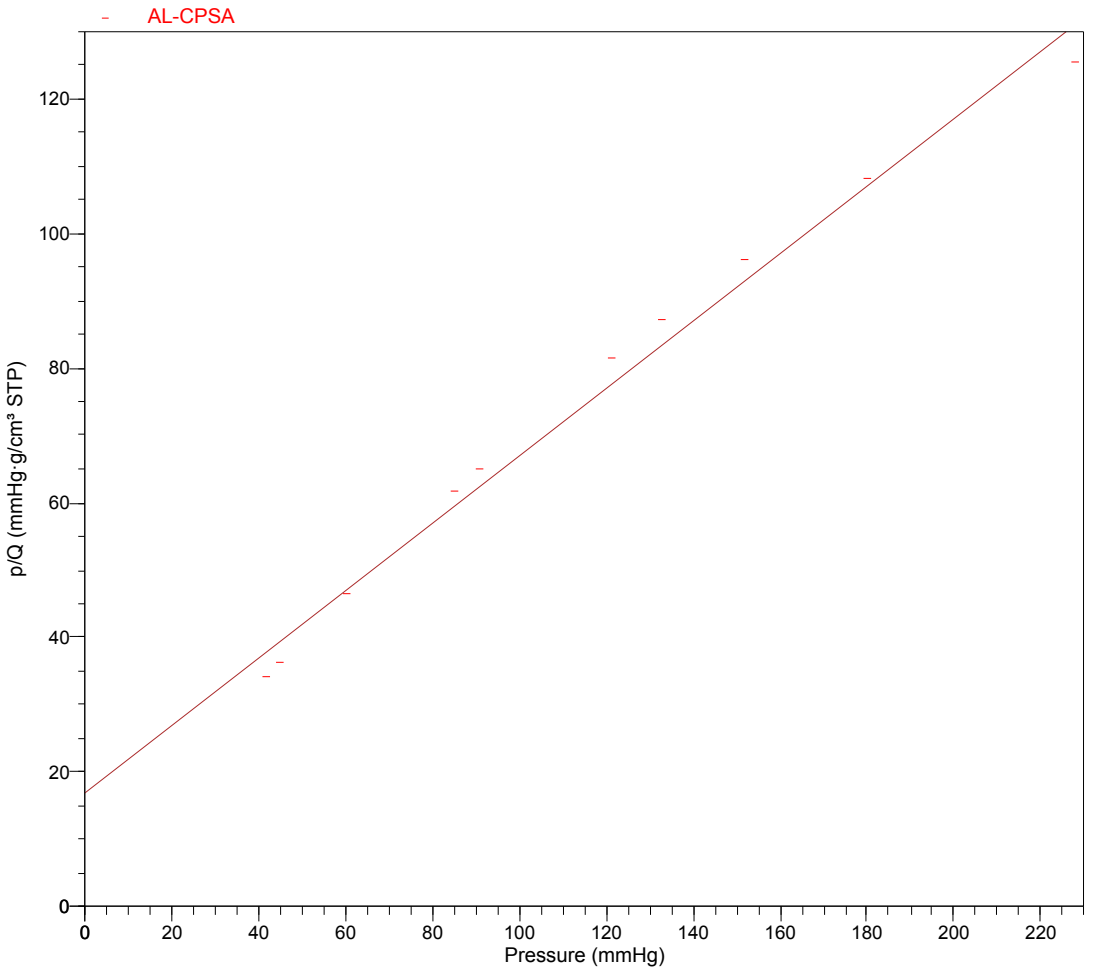

Sample: AL-CPSA
Operator:
Submitter:
File: C:\...\STEINA~1\AL-CPSA.SMP

Started:	22.05.2019 14:03:19	Analysis Adsorptive:	N2
Completed:	22.05.2019 17:57:46	Analysis Bath Temp.:	77.300 K
Report Time:	22.05.2019 18:25:24	Sample Mass:	0.9878 g
Warm Free Space:	11.6061 cm³ Measured	Cold Free Space:	34.0042 cm³ Measured
Equilibration Interval:	5 s	Low Pressure Dose:	None
Sample Density:	1.000 g/cm³	Automatic Degas:	No

Options Report

Sample Tube

Sample Tube:	Sample Tube
Stem Diameter:	3/8 inch
Physical volume below mark:	1.0000 cm³
Use Isothermal Jacket:	Yes
Use Filler Rod:	No

Analysis Conditions

Preparation

Fast evacuation:	No
Evacuation rate:	5.0 mmHg/s
Unrestricted evacuation from:	5.0 mmHg
Evacuation time:	0.10 h
Leak test:	Yes
Leak test duration:	30 s

Free Space

Free-space type:	Measured
Lower dewar for evacuation:	Yes
Evacuation time:	0.10 h
Outgas test:	No

p° and Temperature

p° and T type:	Measure p° at intervals during analysis. Enter the Analysis Bath Temperature below.
p° and T type:	Measure p° at intervals during analysis. Enter the Analysis Bath Temperature below.
Temperature:	77.300 K
Measurement interval:	120 min

Dosing

Use first pressure fixed dose:	No
Use maximum volume increment:	No
Target tolerance:	5.0% or 5.000 mmHg

Equilibration

Equilibration interval:	5 s
Minimum equilibration delay at p/p° >= 0.995:	600 s

Adsorptive Properties

Adsorptive:	Nitrogen
Maximum manifold pressure:	1050.00 mmHg
Non-ideality factor:	0.0000620
Density conversion factor:	0.0015468
Molecular cross-sectional area:	0.162 nm²

Sample: AL-CPSA
Operator:
Submitter:
File: C:\...\STEINA~1\AL-CPSA.SMP

Started:	22.05.2019 14:03:19	Analysis Adsorptive:	N2
Completed:	22.05.2019 17:57:46	Analysis Bath Temp.:	77.300 K
Report Time:	22.05.2019 18:25:24	Sample Mass:	0.9878 g
Warm Free Space:	11.6061 cm³ Measured	Cold Free Space:	34.0042 cm³ Measured
Equilibration Interval:	5 s	Low Pressure Dose:	None
Sample Density:	1.000 g/cm³	Automatic Degas:	No

Summary Report

Surface Area

Single point surface area at p/p° = 0.299279879:	5.5645 m²/g
BET Surface Area:	5.6608 m²/g
Langmuir Surface Area:	8.6811 m²/g
t-Plot Micropore Area:	0.5006 m²/g
t-Plot External Surface Area:	5.1602 m²/g
BJH Adsorption cumulative surface area of pores between 17.000 Å and 3000.000 Å width:	5.8614 m²/g
BJH Desorption cumulative surface area of pores between 17.000 Å and 3000.000 Å width:	5.8983 m²/g

Pore Volume

Single point adsorption total pore volume of pores less than 1219.792 Å width at p/p° = 0.983870046:	0.019743 cm³/g
t-Plot micropore volume:	0.000207 cm³/g
BJH Adsorption cumulative volume of pores between 17.000 Å and 3000.000 Å width:	0.026282 cm³/g
BJH Desorption cumulative volume of pores between 17.000 Å and 3000.000 Å width:	0.026225 cm³/g

Pore Size

Adsorption average pore width (4V/A by BET):	139.5092 Å
BJH Adsorption average pore width (4V/A):	179.356 Å
BJH Desorption average pore width (4V/A):	177.850 Å

Sample: AL-CPSA
Operator:
Submitter:
File: C:\...\STEINA~1\AL-CPSA.SMP

Started:	22.05.2019 14:03:19	Analysis Adsorptive:	N2
Completed:	22.05.2019 17:57:46	Analysis Bath Temp.:	77.300 K
Report Time:	22.05.2019 18:25:24	Sample Mass:	0.9878 g
Warm Free Space:	11.6061 cm³ Measured	Cold Free Space:	34.0042 cm³ Measured
Equilibration Interval:	5 s	Low Pressure Dose:	None
Sample Density:	1.000 g/cm³	Automatic Degas:	No

Sample Log Report

Date	Time	Message
22.05.2019	14:21:04	Helium Purged: 30 seconds
22.05.2019	14:34:40	Measured free space on port 1, Warm: 11.6061 cm³, Cold: 34.0042 cm³
22.05.2019	14:46:55	Starting p° in p° tube measurement.